INTERNATIONAL DOCTORATE IN ATOMIC
AND MOLECULAR PHOTONICS
CICLO XXIX

Settore Scientifico Disciplinare FIS/03

HIGH PRECISION FREQUENCY MEASUREMENT ON A CO MOLECULAR BEAM USING A 6 μm COHERENT SOURCE REFERENCED TO A FIBER DELIVERED ABSOLUTE STANDARD

Candidato

Giacomo Insero

Tutore

Dr. Paolo De Natale

Coordinatore

Prof. Roberto Righini

2013/2016

Abstract

The vibrational transition $|v = 1, J = 1, -\rangle \leftarrow |v = 0, J = 1, +\rangle$ in the $a^3\Pi_1$ state of CO is measured at the kHz level as (51399115447 ± 3) kHz. The measurement is done on a pulsed, supersonic molecular beam. The achieved relative accuracy is $6 \cdot 10^{-11}$, more than four orders of magnitude better than previous measurements.

The thesis consists of two parts. The first part treats the generation of coherent radiation in the mid-infrared by difference frequency generation of two near-infrared lasers in a custom-made orientation-patterned gallium phosphide (OP-GaP) crystal. This novel nonlinear material is extensively characterized. This crystal is particularly interesting for its wide transparency range, its high nonlinear coefficient, and for the possibility of quasi phase-matching with the widely used 1064-nm lasers. Then, it is explained how the accuracy and the stability of the frequency standard at the national metrological institute (INRIM) is transferred to the 6-micron radiation using a 642-km long fiber link and an optical frequency comb. The mid-IR source is characterized in terms of phase noise power spectral density.

The second part of the thesis deals with the experimental setup and the spectroscopic measurement. After a brief discussion of the carbon monoxide energy levels and experimental apparatus, the high precision measurements are presented. The effects of stray fields, mainly magnetic, and of the Doppler shift are extensively discussed.

Contents

Introduction

Thanks to the significant progress of the last years in the field of atomic, molecular and optical (AMO) physics, high resolution spectroscopy measurements have reached astonishing fractional accuracies. In the case of atoms and atomic ions relative accuracies of parts in 10^{-18} have been demonstrated [1], whereas for molecules they are, at present, worse by more than three orders of magnitudes. This difference comes from the more complex internal structure of molecules that makes cooling and detection much more complicated than in the case of atoms. However, the interest for molecules is deep. Their internal structure, their symmetry and the strong intramolecular fields make molecules convenient systems for new studies to disclose new physics [2]. In some cases, these characteristics make molecules more sensitive systems to some fundamental physical aspects than atoms, despite the lower absolute precision of spectroscopic measurements [3–8]. Furthermore, some precision measurements on molecules can already compete with the large particle accelerators in the search for new exotic particles and to test our physical models [4]. The main motivations for high resolution molecular spectroscopic studies are questions about the possible variation of fundamental constants, parity violation, the possible non-zero electrical dipole moment of fundamental particles, and the precise measurements of the Boltzmann constant.

The fine-structure constant α that determines the electromagnetic interaction strength has the measured value $\alpha = 1/137.035999139(31)$ [9], and the proton-to-electron mass ratio is measured as $\mu = m_p/m_e = 1836.15267389(17)$ [9]. The Standard Model does not require these values to be constant, but they are often assumed to be so. However, their possible variation in space and time is a challenging question, especially in light of the observation during the last 20 years, that indicates that the universe is expanding at an accelerating rate [10–12] leading to the postulation of unknown forms of mass and energy. This new form of energy is usually described on the base of the cosmological constant and the dynamical action of a scalar field [13]. It has been shown that an effect of this field would be a variation of the fundamental constants. The natural way to measure the effect of a possible temporal variation of α or μ is to measure atomic or molecular transitions with sufficiently high precision to detect changes of the energy levels over time. For

instance, the most accurate experiment on μ to date was done on SF_6 with the result $\dot{\mu}/\mu = (-3.8 \pm 5.6) \cdot 10^{-14}$ yr^{-1} [5]. Another strategy involves the comparison of astronomical data among each other or with laboratory measurements. The best results for μ, in this latter case, was achieved for methanol using a radio telescope to look back 7 billion years, yielding to $\Delta\mu/\mu = (-0.0 \pm 1.0) \cdot 10^{-7}$ [14].

Another fascinating issue is the search of the parity violating weak force, that is expected to induce a difference in the energy levels of the two enantiomers of a chiral molecule [15]. Some articles [16, 17] suggests that this energy difference should be measurable and an attempt was done with CHFClBr [18] in which the relative energy splitting was constrained to be lower than 10^{-14}. Theoretical studies [19,20] predict a relative splitting of about two orders of magnitude smaller and new experiments are planned [2]. An high resolution spectroscopy experiments have also the possibility to determine whether the electrons have a non-zero electric-dipole moment (EDM), which would violate time and parity reversal symmetries [21] and would indicate for physics beyond the Standard Model [22, 23]. The most accurate experiment so far, performed in a cold beam of ThO molecules produced with a cryogenic buffer gas source [4], constrains the magnitude of the electron-dipole moment to be less than $8.7 \cdot 10^{-29}$ e·cm.

Also the Boltzmann constant k_B is under investigation in several experiments. It plays an important role for a possible redefinition of the kelvin, one of the seven International System (SI) base units [24], since it is based on a fixed definition of the k_B value. The most precise determination of such a constant is provided measuring the speed of sound in a noble gas inside an acoustic resonator [25] with a relative uncertainty of the order of 10^{-6}. Alternative methods have been demonstrated to approach the same precision with the possibility to improve it. One of these methods, called Doppler broadening thermometry, consists in the measurement of k_B from the shape of an atomic or molecular spectral line. To date, the best determination of the Boltzmann constant using this approach was performed in $H_2^{18}O$ reaching a relative uncertainty of $24 \cdot 10^{-6}$ [26].

A fundamental requirement for high resolution spectroscopy is a narrow, stable and powerful laser source that can precisely address the transition to be measured in a reproducible and highly efficient way. One of the most straightforward spectral regions for high-resolution spectroscopy is the microwave where the sources are powerful, reliable and easy to use. The Doppler broadening, that is proportional to the radiation frequency, is much smaller than in the IR or visible region, but the limited interaction time of a molecules with the radiation limits the relative precision of the measurement. Moving at higher frequency allows to reduce the relative influence of the transit time broadening. The mid-IR region is particularly interesting for molecular spectroscopy because it corresponds to the nuclear vibrations. This region is characterized by intense rovibrational transitions with Hz-level natural line widths. In order to reduce the larger Doppler broadening, intrinsic Doppler-free techniques can be employed such as saturated or two-photon absorption spectroscopy. There-

fore, moving from the GHz to the THz frequency range can produce a dramatic increase in the precision but it requires the development of intense and narrow line width laser sources to be referenced to the primary frequency standard.

Quantum cascade lasers (QCLs) are particularly promising for spectroscopy in the mid infrared. They cover the range between 4 to 20 μm [27] allowing for continuous tunability with power ranging from mW to the W level [28]. They have a very narrow intrinsic line width [29–31], but temperature controllers and current drivers introduce external noise so that their typical free-running line width is of the order of few MHz. To reduce these broadenings, several techniques have been demonstrated, such as locking to a sub Doppler transition [32], to a Fabry-Perot cavity [33–35], or to a crystalline whispering gallery mode micro-resonator [36]. With such techniques a relative stability of the order of 10^{-14} over 1 second has already been demonstrated [37]. One serious technological problem involves referring a mid infrared laser to the primary frequency standard of cesium in the microwaves. One approach to bridge the gap from the microwave region to the near infrared involves the use of an optical frequency comb, which is now a mature technology, to reach the near infrared and then using difference frequency generation to reach the mid infrared. The first comb-assisted DFG sources in the mid infrared have been used to measure CO_2 transitions at around 4.3 μm with a relative precision of 10^{-11} [38,39]. However, the spectral region above 5 μm is difficult to access because commercial periodically-poled lithium niobate (PPLN) crystals are not transparent. Other commercial crystals, such as AgGaSe, $AgGaS_2$, GaSe or $ZnSeP_2$, are characterized by low conversion efficiencies and cannot be pumped with the most convenient laser sources such as Nd:YAGs. Some non commercial orientation patterned crystals such as OP-GaP and OP-GaAs can represent a valid alternative since they show higher conversion efficiency with respect to other crystals and present all the advantages of the quasi-phase matching condition.

For precision spectroscopy experiments like that discussed in this thesis, the dissemination of the primary frequency standard is an important part of the frequency chain. The commonly used 10 MHz quartz-oscillator disciplined by a rubidium clock and a GPS (Global Positioning System) can reach absolute accuracy of the order of 10^{-13} [40]. In order to improve this accuracy level, some metrological institutes distribute the frequency standard via optical fiber networks to different laboratories placed all over the national territory. Such a network can provide the primary reference with frequency instabilities of parts in 10^{-15} over 1000 s.

At the beginning of my work as a PhD student, there was the idea of establishing the first laboratory in Italy for high resolution spectroscopy experiments on cold molecules. Thus, I first moved to the Fritz Haber Institute of the Max Planck Society in Berlin. There, in the group of Gabriele Santambrogio in the department of molecular physics headed by Gerard Meijer, I learned to manipulate neutral polar molecules with electric fields using both conventional and miniaturized Stark decelerators. Then, I moved part of the equipment from Berlin to Florence to set up the first Italian laboratory for manipulation of cold molecules using Stark

decelerators. In the meanwhile, I started to work on the stabilization of QCLs using a high-Q ($> 10^7$) whispering galley mode micro-resonator (WGMR) [36, 41]. The emission frequency of the QCL laser was stabilized to ∼10 kHz line width (full width at half maximum) over 1 second timescale. The micro-resonator has the advantage over ordinary Fabry-Perot cavities of working over the whole transparency range of the material used to realize the device, calcium fluoride, which is transparent from the UV to over 6 μm.

In the last year and a half of my PhD work, I have been working at the setup of a stable, narrow and absolutely-referenced mid-IR laser source, which we then used for spectroscopy measurements on metastable CO in a molecular beam. This is the topic of this thesis. An optical frequency comb is referenced to the frequency standard via a 640-km-long optical fiber link with the national metrological institute. Two near-IR lasers are locked to the comb and produce some μW of radiation at 1714 cm^{-1} by difference frequency generation in a non-commercial OP-GaP crystal. To boost the mid-IR power, a QCL is phase locked to the DFG radiation. This radiation is then used to measure a vibrational transition in the first excited state of CO at 1714 cm^{-1} with an accuracy of parts in 10^{-11} by means of transverse laser excitation in a supersonic beam of CO molecules. The achieved accuracy is four orders of magnitude better than previous results. The main limitation is due to the residual Doppler effect.

In the first chapter a brief description of the nonlinear optics theory is provided with particular focus on difference frequency generation. The characterization of the OP-GaP crystal is then exhaustively described. The crystal is pumped with two continuous wave (cw) laser sources at 1064 nm and 1300 nm and mid-IR idler radiation at about 5.8 μm is generated. We have derived an effective nonlinear coefficient of $d = (17 \pm 3)$ pm/V. In the second chapter, the locking scheme to reference the mid infrared radiation to the frequency standard delivered over the optical fiber link is shown. It is also shown how the QCL is locked to the DFG radiation and a characterization in terms of phase noise power spectral density of the final mid-IR radiation is also provided. The third chapter describes the Hamiltonian of the carbon monoxide molecule providing the theory needed to calculate the frequencies of its rovibrational transitions in the $a^3\Pi$ metastable state. The experimental setup is described in Chapter 4. Finally, the spectroscopic measurements are shown in Chapter 5.

Chapter 1

Orientation Patterned Gallium Phosphide Crystal

One fundamental ingredient for sensitive and precise molecular spectroscopy is a coherent, tunable, single-frequency and powerful laser source. The mid-IR region is particularly interesting because it corresponds to the frequencies of vibrational transitions, which are intense and have Hz-level natural line widths. Generation of mid-infrared radiation is still challenging but the introduction of quantum cascade lasers (QCLs) opened up new possibilities for mid-IR molecular spectroscopy. Unfortunately, their free running line width ranges from a few to tens of MHz and they have to be stabilized by means of phase locking or injection locking schemes to make them suitable for high resolution spectroscopy experiments. To phase-lock a QCL and reduce its line width, a reference radiation with narrower line width has to be obtained first. One possible approach exploits difference frequency generation in a nonlinear medium to obtain mid-IR radiation, starting from commercially available narrow laser sources in the near-IR. This method allows for an easy tracing of the generated light to a frequency standard.

This chapter introduces a basic description of nonlinear optical frequency conversion techniques, focusing on difference frequency generation and on the quasi-phase matching technique. After the theoretical introduction, the properties and the whole characterization of the novel orientation-patterned gallium phosphide crystal (OP-GaP) are provided.

1.1 Nonlinear Optics

The polarization induced in a material by an electromagnetic wave is the starting point for understanding its linear and nonlinear optical properties [42]. We start from Maxwell's equations and we derive the nonlinear optical wave equations. Defining a Cartesian coordinate system xyz and considering an electric $\boldsymbol{E}(\boldsymbol{x}, t)$ and a magnetic $\boldsymbol{H}(\boldsymbol{x}, t)$ field in a non-magnetic material ($\boldsymbol{B} = \mu \boldsymbol{H}$) containing no free

charges, we can write the Maxwell's equations as

$$\begin{aligned} \nabla \times \boldsymbol{E} &= -\mu \frac{\partial \boldsymbol{H}}{\partial t} \\ \nabla \times \boldsymbol{H} &= \boldsymbol{J} + \frac{\partial \boldsymbol{D}}{\partial t} \\ \nabla \cdot \boldsymbol{D} &= 0 \\ \nabla \cdot \boldsymbol{B} &= 0 \end{aligned} \tag{1.1}$$

The electric displacement field $\boldsymbol{D}$ and the electric current density $\boldsymbol{J}$ are related to $\boldsymbol{E}$ by

$$\begin{aligned} \boldsymbol{D} &= \epsilon_0 \boldsymbol{E} + \boldsymbol{P} \\ \boldsymbol{J} &= \sigma \boldsymbol{E} \end{aligned} \tag{1.2}$$

where σ is the conductivity and $\boldsymbol{P}$ the dielectric polarization vector, indicating the dipole moment per unit volume of the matter. In the previous equations we have indicated with ϵ_0 and μ the vacuum permittivity and the magnetic permeability respectively[1]. The dielectric polarization vector $\boldsymbol{P} = (P_x, P_y, P_z)$ can be expanded in power series[2] of the electric field $\boldsymbol{E}$. So, for the generic component P_k, we have

$$\begin{aligned} P_k(\boldsymbol{x}, t) =& P_k^0 + \sum_l \left(\frac{\partial P_k}{\partial E_l} \right) E_l + \frac{1}{2} \sum_{l,m} \left(\frac{\partial^2 P_k}{\partial E_l \partial E_m} \right) E_l E_m + \\ &+ \frac{1}{6} \sum_{l,m,n} \left(\frac{\partial^3 P_k}{\partial E_l \partial E_m \partial E_n} \right) E_l E_m E_n + ... \end{aligned} \tag{1.3}$$

where the indexes l, m and n, range upon the x, y, z spatial coordinates and denote the different components of the electric field. Furthermore, each component E_i has to be intended as a function of space and time $E_i(\boldsymbol{x}, t)$, while all the partial derivatives of P_k are calculated at null electric field value. The zero-th order term P_k^0 represents the material polarization density, when no external electric field is applied. Since we are interested in non ferroelectric materials, we can set $P_k^0 = 0$. Then, we introduce the dielectric susceptibility tensor χ and rewrite the previous equation as

$$\begin{aligned} P_k(\boldsymbol{x}, t) =& \sum_l \epsilon_0 \chi_{kl}^{(1)} E_l + \sum_{l,m} \epsilon_0 \chi_{klm}^{(2)} E_l E_m + \\ &+ \sum_{l,m,n} \epsilon_0 \chi_{klmn}^{(3)} E_l E_m E_n + ... \end{aligned} \tag{1.4}$$

where $\chi_{kl}^{(1)}$ is the first order dielectric susceptibility that gives rise to the linear term, while $\chi_{klm}^{(2)}$, $\chi_{klmn}^{(3)}$ and so on are the higher order nonlinear dielectric susceptibilities.

[1] We discuss only non magnetic materials for which $\mu = \mu_0$.

[2] The expansion in power series is not always valid, as in case of saturable absorption, where a more sophisticated approach has to be used.

The second order term is null in all crystals with a center of simmetry, while the third order is non vanishing in all crystalline and isotropic materials. Usually, the previous equation is reported in a more compact form as

$$\begin{aligned}\boldsymbol{P} &= \epsilon_0[\chi^{(1)}\boldsymbol{E} + \chi^{(2)}\boldsymbol{E}^2 + \chi^{(3)}\boldsymbol{E}^3 + ...] \\ &= \epsilon_0\chi^{(1)}\boldsymbol{E} + \boldsymbol{P}^{(2)} + \boldsymbol{P}^{(3)} + ... \\ &= \epsilon_0\chi^{(1)}\boldsymbol{E} + \boldsymbol{P}_{\mathrm{NL}}\end{aligned} \tag{1.5}$$

in which the nonlinear part is separated from the linear term.

Combining the first two Maxwell's equation reported in Eq. 1.1 with Eq. 1.5 and using the vector identity $\nabla \times (\nabla \times \boldsymbol{E}) = \nabla(\nabla \cdot \boldsymbol{E}) - \nabla^2\boldsymbol{E}$, we obtain the wave equation[3]

$$\nabla^2\boldsymbol{E} \simeq \mu\sigma\frac{\partial \boldsymbol{E}}{\partial t} + \mu\epsilon\frac{\partial^2\boldsymbol{E}}{\partial^2 t} + \mu\frac{\partial^2\boldsymbol{P}^{NL}}{\partial^2 t} \tag{1.6}$$

where the relation $\epsilon = \epsilon_0(1 + \chi^{(1)})$ has been used, and the term $\nabla \cdot \boldsymbol{E}$ has been approximated to zero[4].

In the following we will use the complex notation: the symbol $*$ indicates the conjugate while the abbreviation 'c.c.' indicates the complex conjugate of the whole preceding expression.

Let us consider an electric field propagating in the $\hat{z}$ direction, which consists of a superposition of three waves oscillating at frequencies ω_1, ω_2 and ω_3, of the form

$$\boldsymbol{E}(z,t) = [\boldsymbol{E}^{(\omega_1)}(z,t) + \boldsymbol{E}^{(\omega_2)}(z,t) + \boldsymbol{E}^{(\omega_3)}(z,t)] \tag{1.7}$$

with

$$\boldsymbol{E}^{(\omega_j)}(z,t) = \frac{1}{2}[\boldsymbol{E}_j(z)e^{i(\omega_j t - k_j z)} + \text{c.c.}] \tag{1.8}$$

for $j = 1, 2, 3$. The wave-vector $k_j = 2\pi n_j/\lambda_j$ is a function of the refractive index n_j of the material, which depends on the frequency ω_j. The term $\boldsymbol{E}_j(z)$ is used to denote the amplitude of the electric field oscillating at frequency ω_j. The electric field $\boldsymbol{E}(z,t)$, reported in Eq. 1.7, lies in the xy plane. In order to simplify the following analysis, we can consider the case where the polarization vector $\boldsymbol{P}$ and the

[3]
$$\begin{aligned}\nabla^2\boldsymbol{E} \simeq &- \nabla \times (\nabla \times \boldsymbol{E}) = -\nabla \times \left(-\mu\frac{\partial \boldsymbol{H}}{\partial t}\right) = \\ =&\mu\frac{\partial}{\partial t}(\nabla \times \boldsymbol{H}) = \mu\frac{\partial}{\partial t}\left(\boldsymbol{J} + \frac{\partial \boldsymbol{D}}{\partial t}\right) = \\ =&\mu\sigma\frac{\partial \boldsymbol{E}}{\partial t} + \mu\epsilon\frac{\partial^2\boldsymbol{E}}{\partial^2 t} + \mu\frac{\partial^2\boldsymbol{P}^{NL}}{\partial^2 t}\end{aligned}$$

[4]The Maxwell equation predicts $\nabla \cdot \boldsymbol{D} = 0$ when no free charges are present. This equation can be written, using Eq.1.5, as $\epsilon\nabla \cdot \boldsymbol{E} = -\nabla \cdot \boldsymbol{P}^{(NL)}$. Since the nonlinear terms of the polarization are usually very small and slowly varying over the spatial coordinates, we can consider $\nabla \cdot \boldsymbol{E} \simeq 0$.

electric field vector $\boldsymbol{E}$ are parallel and aligned with the $\hat{x}$ axis. In this case we can write the Eq. 1.5 as

$$P = \epsilon_0 \chi^{(1)} E + P^{(NL)} \tag{1.9}$$

Since in the following we are interested in phenomena originating from second order polarization, we can ignore the higher order terms and write

$$\begin{aligned} P &\simeq \epsilon_0 \chi^{(1)} E + P^{(2)} \\ &\simeq \epsilon_0 \chi^{(1)} E + \epsilon_0 \chi^{(2)} E^2 \end{aligned} \tag{1.10}$$

The second order term can be expressed as

$$\epsilon_0 \chi^{(2)} E^2 = \epsilon_0 \chi^{(2)} \frac{1}{4} [E_1 e^{i(\omega_1 t - k_1 z)} + E_2 e^{i(\omega_2 t - k_2 z)} + E_3 e^{i(\omega_3 t - k_3 z)} + \text{c.c.}]^2 \tag{1.11}$$

In nonlinear process descriptions, the dielectric susceptibility tensor is usually written in term of the d-coefficient defined as

$$d^{(\omega)} = \frac{1}{2} \chi^{(2)} \tag{1.12}$$

where the superscript (ω) on the coefficient indicates the oscillation frequency of the electric field at which the nonlinear coefficient refers to. Introducing the d-coefficient, we can make explicit the squared term in the Eq.1.11. Since it is a square of a complex number, terms like E_i^2, $|E_i|^2$ and $E_i E_j^*$ and relative c.c. with $i \neq j$ and $i, j = 1, 2, 3$ are expected to arise. Grouping all the terms that oscillate at the same frequency we get the following result

$$\begin{aligned} \epsilon_0 \chi^{(2)} E^2 = &\left(\epsilon_0 \frac{d^{(2\omega_1)}}{2} E_1^2 e^{i(2\omega_1 t - 2k_1 z)} + \text{c.c.} \right) + \epsilon_0 d^{(0)} |E_1|^2 + \\ &+ \left(\epsilon_0 \frac{d^{(2\omega_2)}}{2} E_2^2 e^{i(2\omega_2 t - 2k_2 z)} + \text{c.c.} \right) + \epsilon_0 d^{(0)} |E_2|^2 + \\ &+ \left(\epsilon_0 \frac{d^{(2\omega_3)}}{2} E_3^2 e^{i(2\omega_3 t - 2k_3 z)} + \text{c.c.} \right) + \epsilon_0 d^{(0)} |E_3|^2 + \\ &+ \left(\epsilon_0 d^{(\omega_1 + \omega_2)} E_1 E_2 e^{i[(\omega_1 + \omega_2)t - (k_1 + k_2)z]} + \text{c.c.} \right) + \\ &+ \left(\epsilon_0 d^{(\omega_1 - \omega_2)} E_1 E_2^* e^{i[(\omega_1 - \omega_2)t - (k_1 - k_2)z]} + \text{c.c.} \right) + \\ &+ \left(\epsilon_0 d^{(\omega_1 + \omega_3)} E_1 E_3 e^{i[(\omega_1 + \omega_3)t - (k_1 + k_3)z]} + \text{c.c.} \right) + \\ &+ \left(\epsilon_0 d^{(\omega_1 - \omega_3)} E_1 E_3^* e^{i[(\omega_1 - \omega_3)t - (k_1 - k_3)z]} + \text{c.c.} \right) + \\ &+ \left(\epsilon_0 d^{(\omega_2 + \omega_3)} E_2 E_3 e^{i[(\omega_2 + \omega_3)t - (k_2 + k_3)z]} + \text{c.c.} \right) + \\ &+ \left(\epsilon_0 d^{(\omega_2 - \omega_3)} E_2 E_3^* e^{i[(\omega_2 - \omega_3)t - (k_2 - k_3)z]} + \text{c.c.} \right) \end{aligned} \tag{1.13}$$

From the previous equations, we can see that the propagation of monochromatic waves in nonlinear media, with squared nonlinearity, gives rise to new light waves oscillating at new frequencies as well as to constant, i.e. non oscillating, terms. The

frequencies of the oscillating terms are $\omega_j \pm \omega_k$, with $j, k = 1, 2, 3$, but, generally, they are non-synchronous and not able to drive oscillations at frequencies ω_1, ω_2 or ω_3, unless, for example, the relation

$$\omega_3 = \omega_1 + \omega_2 \tag{1.14}$$

is verified. In this case, the term at frequency $\omega_1 + \omega_2$ can act as a source for the field oscillating at ω_3, so that power can be exchanged from fields oscillating at ω_1 and ω_2 towards the field characterized by frequency ω_3. In a similar way, we can consider the term $\omega_3 - \omega_2$ driving field at ω_1 and so on. It is common to address the three waves as pump, signal and idler beam for the shorter, middle and longer wavelength, respectively.

Various nonlinear optical phenomena arise from the oscillation of the generated polarization at different frequencies including:

Second Harmonic Generation (SHG) The generation of light oscillating at twice the frequency of the incident beam is know as second harmonic generation. This process is described by the terms with amplitude E_i^2 and $(E_i^*)^2$ with $i = 1, 2, 3$. This process can take place even when only one field, oscillating at one single frequency, is initially present in the nonlinear material.

Optical Rectification (OR) This process takes place when the generation of a zero-frequency component of the electric field arises from an oscillating field. This process is described by the terms with amplitude $|E_i|^2$ with $i = 1, 2, 3$. As for SHG, this phenomenon can take place even when only one frequency of light is initially present in the medium.

Sum/Difference Frequency Generation (SFG or DFG) These two phenomena are obtained when light at frequency $\omega_1 + \omega_2$ or $\omega_1 - \omega_2$ is respectively generated. These processes are described by the terms with amplitude $E_i E_j$ or $E_i^* E_j^*$ and $E_i E_j^*$ or $E_i^* E_j$ with $i \neq j$. The DFG process is employed to convert shorter wavelength radiations to longer wavelengths, whereas the SFG is applied to generate shorter wavelengths starting from longer ones. When the two initial frequencies are the same, SFG and DFG reduce, respectively, to SHG and OR.

Linear Electro-Optic Effect (EO) With this term we refer to the modulation of a light beam due to an applied static, or low frequency, electric field. This process, also known as Pockel's effect, is described by the terms $E_i E_j$, $E_i E_j^*$ and their complex conjugates with $i \neq j$ and $\omega_j \simeq 0$.

Now we derive the fundamental equations that describe the nonlinear optical processes at the second-order in the electric field. We focus on the electric field $E^{(\omega_1)}$, oscillating at frequency ω_1. If $\omega_3 = \omega_1 + \omega_2$, from Eq. 1.13 we select the second-order polarization term oscillating at the same frequency $\omega_1 = \omega_3 - \omega_2$.

Then, by using Eq. 1.6, we can write a wave equation for the oscillating field at frequency ω_1 as

$$\begin{aligned}\nabla^2 E^{(\omega_1)} =& \mu\sigma_1 \frac{\partial E^{(\omega_1)}}{\partial t} + \mu\epsilon_1 \frac{\partial^2 E^{(\omega_1)}}{\partial^2 t} + \\ &+ \mu\epsilon_0 \left[d^{(\omega_3-\omega_2)} \frac{\partial^2}{\partial^2 t} \left(E_3(z) E_2^*(z) e^{i[(\omega_3-\omega_2)t-(k_3-k_2)z]} \right) + \text{c.c.} \right]\end{aligned} \tag{1.15}$$

where σ_1 and ϵ_1 are the dielectric conductivity and permeability at frequency ω_1. The Laplace operator of the electric field can be directly derived as

$$\begin{aligned}\nabla^2 E^{(\omega_1)} &= \frac{1}{2} \frac{\partial^2}{\partial z^2} \left[E_1(z) e^{i(\omega_1 t - k_1 z)} + \text{c.c.} \right] \\ &\simeq -\frac{1}{2} \left[k_1^2 E_1(z) + 2ik_1 \frac{dE_1(z)}{dz} \right] e^{i(\omega_1 t - k_1 z)} + \text{c.c.}\end{aligned} \tag{1.16}$$

where the second derivative of the electric field amplitude over z has been neglected assuming a slow variation of the electric field amplitude over the space position z. This approximation is known as SVEA (slowly varying envelope approximation), that can be mathematically formulated as

$$\left| k_1 \frac{dE_1(z)}{dz} \right| \gg \left| \frac{d^2 E_1(z)}{dz^2} \right| \tag{1.17}$$

Combining Eq. 1.15 with Eq. 1.16 and recognizing that $k_j^2 = \omega_j^2 \mu\epsilon_j$, we obtain the basic equations describing nonlinear parametric interactions:

$$\begin{aligned}\frac{dE_1}{dz} &= -\frac{\sigma_1}{2}\sqrt{\frac{\mu}{\epsilon_1}} E_1 - i\frac{\omega_1}{cn_1} d^{(\omega_3-\omega_2)} E_3 E_2^* e^{-i(k_3-k_2-k_1)z} \\ \frac{dE_2}{dz} &= -\frac{\sigma_2}{2}\sqrt{\frac{\mu}{\epsilon_2}} E_2^* - i\frac{\omega_2}{cn_2} d^{(\omega_1-\omega_3)} E_1^* E_3 e^{-i(k_3-k_2-k_1)z} \\ \frac{dE_3}{dz} &= -\frac{\sigma_3}{2}\sqrt{\frac{\mu}{\epsilon_3}} E_3 - i\frac{\omega_3}{cn_3} d^{(\omega_1+\omega_2)} E_1 E_2 e^{i(k_3-k_2-k_1)z}\end{aligned} \tag{1.18}$$

where the last two equations are calculated in a similar way for fields oscillating at frequencies ω_2 and ω_3 respectively. Notice, that the three equations are coupled together via the nonlinear tensor d.

It is interesting to derive the photon conservation conditions, which can be easily obtained from Eq. 1.18. In the International System, the electric field intensity I is related to its amplitude by

$$I = \frac{c\epsilon_0 n}{2} |E|^2 \tag{1.19}$$

The rate of change in intensity over the spatial coordinate z can be obtained by

$$\frac{dI}{dz} = \frac{c\epsilon_0 n}{2} \left(E^* \frac{dE}{dz} + \text{c.c.} \right) \tag{1.20}$$

Multiplying the first expression in Eq. 1.18 by the factor $cn_1\epsilon_0 E_1^*/(2\omega_1)$, and using Eq. 1.20, we obtain

$$\frac{1}{\omega_1}\frac{dI_1}{dz} = -\frac{i}{2}\epsilon_0 d^{(\omega_3-\omega_2)} E_3 E_2^* E_1^* e^{-i(k_3-k_2-k_1)z} + \text{c.c.} \tag{1.21}$$

where we have considered, for simplicity, a lossless material where σ is zero. With similar calculations over the other two equations we obtain

$$\frac{1}{\omega_3}\frac{dI_3}{dz} = -\frac{1}{\omega_1}\frac{dI_1}{dz} = -\frac{1}{\omega_2}\frac{dI_2}{dz} \tag{1.22}$$

These are the so-called *Manley-Rowe relations* and can be interpreted as photon conservation conditions. Since the single photon energy is $\hbar\omega$, the quantity I/ω is proportional to the number of photons. For this reason Eq. 1.22 says that when one photon of the field oscillating at frequency ω_3 is created, at the same time one photon at ω_1 and one at ω_2 are destroyed (SFG) or vice versa (DFG). In a SHG process two photons from the pump beam are destroyed and a single photon at the new frequency is simultaneously created.

1.1.1 DFG Theory

In this section, we focus on the analysis related to difference frequency generation phenomena. We will derive its efficiency and discuss the main properties of this three-wave mixing process.

Let us assume two plane waves, oscillating at frequency ω_3 and ω_2, that interact in a nonlinear medium of length L, for example a crystal, and that produce a new wave, oscillating at frequency $\omega_1 = \omega_3 - \omega_2$. We can assign the labels pump, signal and idler to the beams oscillating at frequencies

$$\begin{aligned}\omega_1 &\rightarrow \text{idler}\\ \omega_2 &\rightarrow \text{signal}\\ \omega_3 &\rightarrow \text{pump}\end{aligned}$$

that will be useful later in the text.

If we introduce the quantity Δk, called *phase mismatch*, defined as

$$\Delta k = k_3 - (k_1 + k_2) = k_3 - k_1 - k_2 \tag{1.23}$$

the first line of Eq. 1.18 can be written as

$$\frac{dE_1}{dz} = -i\frac{\omega_1}{n_1 c} dE_3 E_2^* e^{i\Delta k z} \tag{1.24}$$

where the compact notation $d^{(\omega_3-\omega_2)} = d$ is used because we are considering only the DFG process. Considering the fields $E_3(z)$ and $E_2(z)$ constant over the whole

crystal length, we can integrate the previous equation over the length of the crystal, namely z over the interval $[0, L]$, obtaining

$$E_1(L) = -i\frac{\omega_1 d}{n_1 c} E_3 E_2^* \frac{e^{i\Delta k L} - 1}{i\Delta k} \tag{1.25}$$

where the boundary condition $E_1(z = 0) = 0$ is imposed and $n_1 = \sqrt{\epsilon_1/\epsilon_0}$ represents the refractive index of the crystal at frequency ω_1. Using Eq. 1.19 and remembering that the intensity is defined as the power P per unit area, if we suppose that the nonlinear interaction takes place in a cross section A of the crystal, we can calculate the conversion efficiency of the difference frequency generation process η_{DFG} as

$$\eta_{DFG}(A, L) = \frac{P_1}{P_2 P_3} = \frac{8\pi^2 d^2 L^2}{\epsilon_0 c \lambda_1^2 n_1 n_2 n_3 A} \mathrm{sinc}^2\left(\frac{\Delta k L}{2}\right) \tag{1.26}$$

where $\mathrm{sinc}(x) = \sin x/x$. This equation is derived for a DFG process in which $\omega_1 = \omega_3 - \omega_2$, but a similar function can be derived for a SFG process in which $\omega_3 = \omega_1 + \omega_2$ and for other processes.

In all of these cases, the spectral dependence of the conversion efficiency is mainly determined by the term $\mathrm{sinc}^2(\Delta k L/2)$ since that term is the most frequency-dependent compared to the other factors. For this reason, by slightly detuning the wavelength away from the condition $\Delta k = 0$, called *phase matching condition*, it results in a decrease of the nonlinear efficiency. The oscillatory behavior of efficiency versus $\Delta k L$ can be explained in terms of dephasing of the generated light with respect to the polarization that generates the wave itself: the ω_1 wave, generated at a general position z_1 and propagating up to position z_2 inside the crystal, can be out of phase with the radiation generated at z_2. This results in an interference that is described by the oscillatory factor. Note that the generated power P_1 is directly proportional to the product $P_3 P_2$: this allows the use of a relatively weak pump or signal laser to obtain detectable nonlinear generation, if the other beam is sufficiently powerful.

The generation efficiency, reported in Eq. 1.26, can be seen as an oscillating function of L with semi-period l_c

$$l_c = \frac{\pi}{\Delta k} = \frac{\pi}{k_3 - k_2 - k_1} \tag{1.27}$$

called *coherence length*. This parameter corresponds to the maximum crystal length that is useful to generate difference frequency power, as a function of phase mismatch in case of plane waves. Considering the dependence over L, the oscillating term in the Eq. 1.26 can be written as $\sin^2(\frac{\pi}{2}\frac{L}{l_c})$: every l_c the efficiency goes from zero to its maximum and vice-versa, up to the end of the crystal, as shown in the lower curve in Fig. 1.2 at page 18, where the generated idler intensity is reported as a function of position z inside the crystal. If $\Delta k \neq 0$ we can think at the crystal as an array of sub-crystals with length l_c: if the ω_1 power increases in one segment, in the next

one it will decrease down to zero, in favor of pump fields ω_3 and ω_2 and then it will increase again in the next l_c array. In the limit of $\Delta k \to 0$, the coherence length becomes infinite and all the crystal length participates to increase the idler power. In this case, the efficiency has a quadratic dependence over the crystal length L, as shown in the upper curve in Fig. 1.2.

Generally, the phase matching condition cannot be satisfied by the most common materials where the refractive index normally increases with ω. Using the identity $k_j = \omega_j n_j / c$, where $n_j = n(\omega_j)$ denotes the index of refraction at frequency ω_j, we can in fact rewrite the Eq. 1.23 as

$$\omega_1 n_1 + \omega_2 n_2 = \omega_3 n_3 \tag{1.28}$$

that can be written as

$$n_3 - n_2 = (n_1 - n_2)\frac{\omega_1}{\omega_3} \tag{1.29}$$

In anisotropic materials, transparent at the involved wavelengths, the refractive index is an increasing function of the frequency. Since $\omega_3 > \omega_1$, the previous equation can be solved if $n_1 - n_2 > n_3 - n_2$. This is equal to $n_1 > n_3$, that is in contrast with the initial assumption about the refractive index.

However, the phase matching condition can be satisfied in anisotropic materials, for which the index of refraction depends upon the polarization of the traveling beam: this phenomenon is called *birefringence*. One example is given by uniaxial crystals, i.e. crystals with one symmetry axis (optical axis). A wave propagating in such a material can experience two different refractive indexes called ordinary, n_o, and extraordinary, n_e, refractive index depending on the electromagnetic wave propagation direction and polarization. If the wave at higher frequency is polarized along the direction with the lower refractive index, the phase matching condition can be satisfied.

1.1.2 DFG with Gaussian Beams

The analysis, carried out in the previous section, is based on the plane wave approximation, but in real experiments focused Gaussian beams are usually employed. In a Gaussian beam propagating in the $\hat{z}$ direction, the electric field amplitude, i.e. $E_j(z)$ in Eq. 1.8, is a function of all the spatial coordinates x, y and z. This amplitude can be written as

$$E_j(x, y, z) = E_{\mathrm{G}j}(z) \exp\left(- \frac{x^2 + y^2}{w_j(z)^2} \right) \tag{1.30}$$

where we have supposed that the beams have TEM_{00} modes and we have indicated with $w_j(z)$ the radius $\rho = \sqrt{x^2 + y^2}$ at which the field amplitude falls to $1/e$ of its axial value at a generic point z along the beam. The index j, as before, can assume value 2 or 3 if referenced to signal or pump beams, respectively. As for the plane wave approximation, we assume that the Gaussian electric field amplitude $E_{\mathrm{G}j}(z)$ does not decrease with the z coordinate, that corresponds to the case with

no absorption and negligible depletion by the DFG process. In this case, the beam size can be described as a function of position z as

$$w_j(z) = w_{0j}\sqrt{1 + \left(\frac{z}{z_{\mathrm{R}j}}\right)^2} \tag{1.31}$$

where w_{0j} is the waist, i.e. $w_j(z = 0)$, and $z_{\mathrm{R}j}$ is the Rayleigh distance defined as the distance between the waist and a point where the radius $w(z_{\mathrm{R}j}) = \sqrt{2}w_{0j}$. Another useful quantity is the confocal parameter b_j, defined as twice the Rayleigh distance.

In order to derive the difference frequency generation efficiency, let us calculate the integrated optical power of the two impinging beams. To simplify this calculation, we consider the situation in which the beam size remains constant over the nonlinear material interaction length L. From Eq. 1.31 we can see that this assumption corresponds to the case $z_{\mathrm{R}j} \gg L$ for which we can derive the optical power as

$$P_j = \frac{\epsilon_0 n_j c}{2}\int_S |E_j(x,y)|^2 dxdy = \frac{\epsilon_0 n_j c}{2}\frac{\pi w_{0j}^2}{2}|E_{\mathrm{G}j}^2| \tag{1.32}$$

where the integral is calculated over the plane S orthogonal to $\hat{z}$ axis. Making use of the following relation which holds among the three waists

$$\frac{1}{w_{01}^2} = \frac{1}{w_{02}^2} + \frac{1}{w_{03}^2} \tag{1.33}$$

we can rewrite the difference frequency generation efficiency, Eq. 1.26, as

$$\eta_{DFG}(w_{03}, w_{02}, L) = \frac{16\pi}{\epsilon_0 c\lambda_1^2}\frac{d^2}{n_1 n_2 n_3}\frac{L^2}{w_{02}^2 + w_{03}^2}\mathrm{sinc}^2\left(\frac{\Delta kL}{2}\right) \tag{1.34}$$

According to the previous relation, the DFG efficiency can be increased reducing the input beam waists, at least until $z_{\mathrm{R}j} \gg L$, for which the Eq. 1.34 is derived. This equation has been derived under several assumptions (no absorption, constant beam size inside the crystal, equal confocal parameters) and a more general equation is needed for a complete description of the nonlinear processes in a more realistic case. An all-inclusive theory allows to calculate the maximum achievable generation efficiency as well as to determine the second-order nonlinear optical susceptibilities for different materials. Discrepancies between experimental data and predictions were often ascribed, in the past, to non perfect crystal quality, but nowadays, since the growing techniques have reached very high quality, these discrepancies have to be explained with different arguments. Frequently, the literature provides non consistent values of nonlinear optical susceptibility, which originate from experimental methods and from the weaknesses of the theoretical models used to describe the phenomena. For this reason, in literature, there are many attempts to include effects such as absorption, focusing, beam waist position inside the nonlinear material, diffraction, pump depletion and so on.

Some more detailed theoretical descriptions can be found in [43–46] and [47], but they suffer from limitations due to some approximations such as the neglected absorption, the assumption of equal confocal parameters etc. The most complete model for DFG is provided in [48], in which the general case for difference-frequency generation is analyzed. The only assumption here is that the two input beams have TEM_{00} modes. From [48], we obtain the conversion efficiency of the nonlinear process $\eta_{DFG} = P_1/(P_3P_2)$ as

$$\begin{aligned}\eta_{DFG} =& \frac{8\omega_1^2 d^2}{\pi\epsilon_0 c^3 n_1 n_2 n_3} \exp(-\alpha_1 L) L (k_2^{-1} - k_3^{-1})^{-1} h(\mathfrak{a}, \mathfrak{l}, \mathfrak{f}, \mathfrak{s}) \\ =& \frac{16\omega_1^2 d^2}{\pi\epsilon_0 c^3 n_1 n_2 n_3} \exp(-\alpha_1 L) \left(\frac{L}{w_{02}^2 + w_{03}^2}\right) \left(\frac{k_2 z_{\mathrm{R}3} + k_3 z_{\mathrm{R}2}}{k_3 - k_2}\right) h(\mathfrak{a}, \mathfrak{l}, \mathfrak{f}, \mathfrak{s})\end{aligned} \tag{1.35}$$

where the following identities are used

$$\begin{aligned} w_{0\mathrm{d}} &= \frac{w_{03} w_{02}}{\sqrt{w_{03}^2 + w_{02}^2}} \\ z_{\mathrm{Rd}} &= \frac{1}{2} k_1 w_{0\mathrm{d}}^2 = \frac{k_3 - k_2}{k_2 z_{\mathrm{R}3} + k_3 z_{\mathrm{R}2}} z_{\mathrm{R}2} z_{\mathrm{R}3} \\ \mathfrak{a} &= \frac{\alpha_3 + \alpha_2 - \alpha_1}{2} z_{\mathrm{Rd}} \\ \mathfrak{l} &= L/z_{\mathrm{Rd}} \\ \mathfrak{f} &= f_c/z_{\mathrm{Rd}} \\ \mathfrak{s} &= \Delta k \, z_{\mathrm{Rd}} \end{aligned} \tag{1.36}$$

The function $h(\mathfrak{a}, \mathfrak{l}, \mathfrak{f}, \mathfrak{s})$, called *aperture function*, includes all the beam parameter dependencies: this function is a complex variable integral, which has no analytical solution and therefore has to be solved numerically. The integration cancels out the complex variables and yields to a real function. The exponential term takes into account the absorption of generated light inside the crystal. The parameter z_{Rd} is the Rayleigh range for the generated beam and can be expressed as a function of $w_{0\mathrm{d}}$, which represents the beam waist of the idler beam. z_{Rd} can be thought as a new distance reference unit: in fact, the parameters $\mathfrak{l}$ and $\mathfrak{f}$ define the crystal length and the position of the input beams foci in unit of z_{Rd}. The two input beams have to overlap their waists to a common position in order to reach maximum efficiency and f_c represents the distance[5] from the input crystal facet of their foci. Also the parameters $\mathfrak{s}$ and $\mathfrak{a}$, called respectively *mismatch* and *normalized absorption*, represent the phase matching condition and the absorption normalized to the new unit z_{Rd}. Notice that $\mathfrak{a}$, argument of the aperture function, includes the absorption at all three waves involved in the nonlinear process.

[5]Notice that f_c is the waist location with respect to the crystal facet inside the medium of refractive index n_j. If f_{cj}^{air} denotes the position of the input beam waists in air, $j = 3$ or $j = 2$, a translation of the crystal in a way to intercept the beam yields a position inside the medium $f_c = n_j f_{cj}^{air}$.

The first important result of this generation efficiency formula is that the dependence over the crystal length in phase matching condition is linear and not quadratic, as in the case of plane wave approximation. However, consistent with Eq. 1.34, when the aperture function is calculated for a plane wave, it contains a factor proportional to L, so that the efficiency will again depend quadratically on L. A second interesting result regards the optimal position of the foci f_c inside the crystal. When absorption is neglected, typically $\alpha_j L < 0.05$ with $j = 1, 2, 3$, the optimum waist location is always in the middle of the crystal: $f_c = L/2$. Instead, when absorption is taken into account, the optimal position of the foci shifts towards one of the two crystal facet.

In relation to our measurements on OP-GaP, for which the measured absorption is of the order of 0.15 cm^{-1}, for both pump and signal beams, the absorption cannot be neglected because $\alpha_j L \sim 0.4$. We find out that the optimal foci position inside the crystal is achieved when input beams are focalized really close to the input facet.

The last result is that the optimum conversion efficiency for non critical phase matching[6] corresponds always to the condition of equal confocal parameters.

1.1.3 Quasi-Phase Matching Conditions

As we have shown in the previous sections, the nonlinear frequency conversion efficiency is strongly dependent on the phase matching condition. For collimated beams, we have seen in Eq. 1.26 that the efficiency dependence is of the type $[\sin(\Delta kL/2)/(\Delta kL/2)]^2$, having a maximum for $\Delta k = 0$. For a Gaussian focused beam, instead, it can be shown that the maximum is obtained for Δk close to, but not exactly zero. In both cases, the phase matching condition has to be satisfied in order to maximize the generation efficiency. As mentioned before, the birefringent phase matching techniques can only be used in anisotropic crystals. However, several isotropic materials exhibit large values of the d-coefficient, little absorption and other desirable properties, if compared to the anisotropic ones. In addition, even some anisotropic materials with a specific crystal structure can have very high nonlinear coefficients which cannot be addressed in the birefringent phase matching techniques[7]. We have seen (Eq. 1.26) that the generated power is an oscillating function of the crystal position z and that only the first layer of thickness l_c is useful for the generation. Since common values of l_c are of the order of tens or hundreds of microns, the generation efficiency is low and cannot be enhanced. This problem can be overcome using the quasi-phase matching (QPM) technique. Here the crystal is configured as a layered structure, in which each layer thickness is l_c and the d-value of two consecutive layers is equal in magnitude but opposite in sign, i.e. a phase

[6] Noncritical phase matching, sometimes called temperature phase matching, is a technique for phase matching by tuning the crystal temperature.

[7] For example $LiNbO_3$ have d_{333} term about one order of magnitude higher than the other terms but it does not play any role in nonlinear generation because, due to the crystal structure, the $\Delta k = 0$ condition cannot be fulfilled [49]

factor $e^{i\pi}$ is introduced between two adjacent layers. In this way the energy flows from pump to signal and idler waves in the first layer and, instead of reversing back from idler and signal to pump wave, it continues its flow in the same direction in the following layer. Continuously changing the sign of d every l_c up to the end facet of the crystal, a continuous flux of energy from incident to generated beam is obtained through all the nonlinear material. In this way the longer is the crystal the higher is the generated power.

We can use a more quantitative approach to understand the QPM technique. The nonlinear polarization is sign reversed in the positions

$$z = l_c, 2l_c, 3l_c, \ .... \qquad \text{with} \ \ l_c = \frac{\pi}{\Delta k} \tag{1.37}$$

These positions correspond to the point where the power flux would reverse direction in the non phase matched case. If we consider the crystal made by an array of very short layers, stacked over the z axis, each of which of thickness $\Delta \ll l_c$, we can use the Eq. 1.18 to calculate the complex electric field increment over each segment, centered at general coordinate z, as

$$\Delta E_1(z) = -i\frac{\omega_1}{n_1 c} d(z) E_3 E_2^* e^{i\Delta k z}\Delta \tag{1.38}$$

To characterize the overall process, we can think each increment $\Delta E_1(z)$ as a phasor and sum them over the crystal length. What we get is summarized in Fig. 1.1, together with the other type of phase matching conditions. In the non phase matched case the difference frequency generated field grows up from $z = 0$ up to $z = \pi/\Delta k$ and then decreases up to $z = 2\pi/\Delta k$ when the field is null again. In the case of quasi-phase matching, the situation is exactly the same from $z = 0$ to $z = \pi/\Delta k$, where the sign of nonlinear coefficient is reversed and the resulting electric field $E_1(z)$ starts to grow up again. These process is repeated up to the crystal end facet at $z = L$. In the phase matched case the electric field increase quadratically with the position z. The power generated as a function of the position z inside the crystal is reported in Fig. 1.2 for the three different phase matching conditions. Since the coherence length depends on the wavelength of the various beams, the inversion period has to be designed accordingly. For small variations of the beam frequencies, the quasi-phase matching condition can be restored by changing the crystal temperature, which slightly affects both the crystal length and the index of refraction.

Let us now calculate the nonlinear efficiency in such a material, using the plane wave and non-depleted input pumps approximation to simplify the results and focus on the physical meaning. The results can be easily applied in focused Gaussian beams theory. Since the new nonlinear coefficient is periodic, we can expand it in a Fourier series

$$d(z) = d_{\text{bulk}}\left[\sum_{m=-\infty}^{+\infty} a_m \exp\left(i\, m \frac{2\pi}{\Lambda} z\right)\right] \tag{1.39}$$

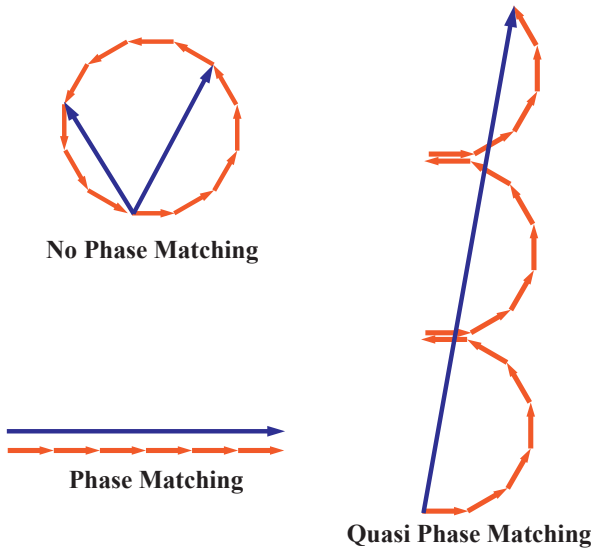

Figure 1.1: Comparison of different types of phase matching in the complex plane. Each arrow indicates the increment in the generated electric field $\Delta E_1(z)$ in every layer of thickness Δ inside the crystal. The dark lines denote the resulting field amplitude after the propagation inside the nonlinear material, i.e. $E_1(L)$. In the non phase matching scenario the resulting field can only assume values between zero and its maximum $E(z = l_c)$.

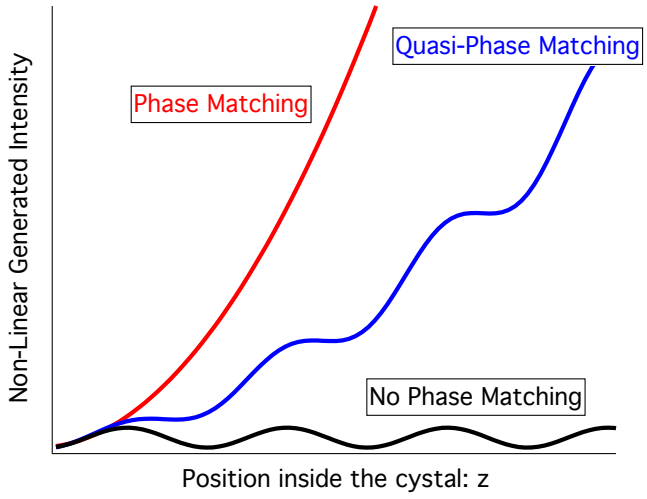

Figure 1.2: Nonlinear generated intensity as function of the position z inside the crystal for the phase matching, quasi-phase matching and no phase matching.

where the coefficients a_m are expressed by the relation

$$a_m = \frac{1}{\Lambda}\int_0^{\Lambda} \frac{d(z)}{d_{\text{bulk}}} \exp\left(- i\, m \frac{2\pi}{\Lambda} z \right) dz \tag{1.40}$$

Here we have identified the period of the inversion with Λ, assuming that $d(z)$ switches from d_{bulk} to $-d_{\text{bulk}}$. If we now insert the Fourier expanded coefficient $d(z)$ into the first Eq. 1.18, for the difference frequency generation, we get

$$\frac{dE_1}{dz} = -i\frac{\omega_1}{n_1 c} d_{\text{bulk}} E_3 E_2^* \sum_{m=-\infty}^{+\infty} a_m \exp[-i(k_3 - k_2 - k_1 - m\frac{2\pi}{\Lambda})z] \tag{1.41}$$

where a lossless material is considered. The new quasi-phase matching condition can be obtained if for some integer number $m = m'$ the equation

$$\Delta k' = k_3 - k_2 - k_1 - m'\frac{2\pi}{\Lambda} = \Delta k - m'\frac{2\pi}{\Lambda} = 0 \tag{1.42}$$

is satisfied. All other $m \neq m'$ terms in the Eq. 1.41 averages to zero over distances that are large compared to the coherence length l_c, as the crystal length, and can be ignored. Thus the Eq. 1.41 can be written more simply as

$$\frac{dE_1}{dz} = -i\frac{\omega_1}{n_1 c} d_{\text{bulk}} E_3 E_2^* a_{m'} \exp[-i(k_3 - k_2 - k_1 - m'\frac{2\pi}{\Lambda})z] \tag{1.43}$$

If we assume the simplest case in which the $d(z)$ switches from d_{bulk} to $-d_{\text{bulk}}$ and vice versa every $\Lambda/2$, for $m' \neq 0$ the Fourier coefficient $a_{m'}$ assumes the form

$$a_{m'} = \frac{1 - \cos(m'\pi)}{m'\pi} \tag{1.44}$$

If we choose $m' = 1$ to satisfy the quasi-phase matching condition, the effective value d_{eff} is

$$d_{\text{eff}} = a_1 d_{\text{bulk}} = \frac{2}{\pi} d_{\text{bulk}} \tag{1.45}$$

From the last equation we can see that the value of the new coefficient is only slightly lower than in the phase-matched case, but the advantage, as already mentioned, is the possibility of using an higher nonlinear coefficient (otherwise not usable), or crystals that cannot satisfy the phase matching condition as GaP. For example, if we consider $LiNbO_3$, the term d_{333} is around 5 times greater than the other terms that are generally used in birefringent phase matching, but it can be used only if quasi-phase matching is used. Since the efficiency of a second-order nonlinear process is quadratic with d, this means that in quasi-phase matching the generated power is around 25 times bigger than in the other case. Another advantage is that the periodicity can be realized in such a way to satisfy the QPM equation for all the wavelengths inside the transparency range of the medium, while this is not

necessarily possible for birefringent media. Finally, QPM is a powerful technique also because it allows to work with a normal incidence geometry of the pump and signal beams. In birefringent crystals, the non-normal incidence induces different propagation angles of the beams inside the material due to the different refractive indexes experienced by the beams (called *walk-off*). This reduces the overlapping region between the beams and strongly limits the generated idler power. QPM allows to overcome this problem, thus making possible the use of longer crystals and allowing for higher generated idler powers.

1.2 The OP-GaP Crystal

We need DFG radiation at around 5.83 μm to phase lock a quantum cascade laser, that we use to drive vibrational transition in metastable CO. Two basic requirements have to be satisfied in the choice of the nonlinear medium: minimum absorption at the three wavelengths involved in the process and highest nonlinear coefficient as possible. Oxide birefringent crystals, like $LiNbO_3$, $LiTaO_3$ or $KTiOPO_4$, have been extensively used for cw multi-mW DFG or OPO [50, 51], but they are transparent only at wavelengths lower than about 5 μm. Idler radiations with wavelengths longer than 5 μm can be generated with birefringent crystals like $CdSiP_2$, $AgGaSe_2$, $AgGaS_2$ or $LiInSe_2$, which in some cases are commercially available. They can be used over a wide spectral range but, due to their non-negligible absorption if compared to the oxide materials, cw generation is sometimes difficult to achieve. Moreover, their low nonlinear coefficients strongly limit the generated power. As an example, $AgGaS_2$ has been used to produce cw radiation over the 5–12.5 μm range [46, 52], but the idler power was limited to the 10–1000 nW-range.

Recently, the development of orientation patterning (OP) techniques [53] has opened up the possibility to use different materials with higher nonlinear coefficients like OP-GaAs and OP-GaP with also the advantages of QPM. OP-GaAs has been used for quasi-cw parametric oscillation around 4.7 μm with a Ho:YAG pump laser source at 2.1 μm [54], for SFG of a cw QCL at 5.4 μm [55], and only few papers report on cw DFG with OP-GaAs above 6 μm [56–58]. One of the limiting factors of GaAs is its strong absorption at 1.064 μm, which makes difficult its use with the highly-stable and powerful laser sources available in this region. To date only few papers have been published on OP-GaP [59, 60]. The main difference between OP-GaAs and OP-GaP is the much broader transparency region of OP-GaP: gallium phosphide has a relatively small two-photon absorption coefficient in the near-IR. In addition, compared with GaAs, it has a lower refractive index, larger nonlinear coefficient and thermal conductivity, and a lower thermal expansion coefficient. The properties of OP-GaP are listed in Tab.1.1.

For these reasons the interest in GaP has increased over the last few years and the search for a good growing technique has been initiated. First attempts of growing were based on molecular beam epitaxy (MBE) [63] and metal-organic chemical vapor

Table 1.1: Properties of OP-GaP [54], [61] and our work [62].

Property	Value
Transparency Range	0.57–12 μm
Thermal Conductivity	110 W/(m K)
Thermal Linear Expansion	$4.65{\cdot}10^{-6}$ K^{-1}
Possible Pattern Period	14.5–95.9 μm
Effective nonlinear coefficient @ 6 μm	17 pm/V

deposition (MOCVD) [64], trying to repeat the success obtained in the fabrication of OP-GaAs, which was the first realization of a practical and efficient quasi-phase matching semiconductor. To date, the only method producing orientation-patterned layers in GaP with a thickness of hundreds of μm is hydride vapor phase epitaxy (HVPE).

In Fig. 1.3 the growing process for OP-GaP is shown. A silicon layer of about 5 nm is grown over a GaP (100) substrate. A thin smoothing layer of AlGaP is then deposited, followed by a thicker layer of inverted GaP. The inverted GaP layer is then photolithographically patterned with a grating period and then etched down to the surface of the original GaP substrate. After removing the photoresist, the crystal is grown for around 200 nm in a MBE chamber. After this passage, the crystal is HVPE grown to reach thickness of the order of few hundreds of microns.

We use the fundamental of a Nd:YAG at 1064 nm laser and a diode laser around 1300 nm to obtain DFG radiation around 5.8 μm. Thus, the grating period of the OP-GaP crystal, using the Eq. 1.42 for $m' = 1$, turns out to be 24 μm. We received two such crystals from BAE Systems, Inc.[8] thanks to a collaboration with Peter Schunemann. In the following text the two crystal samples are referred to as CS1 and CS2. All the details of the two samples are listed on Tab. 1.2. Both crystals were anti-reflection coated at the three wavelengths used for DFG, with nominal reflections lower than 0.5 %. Using a power meter we have checked that the nominal reflectivity agrees with the measured value. In Fig. 1.4 a zoom of the patterned region is shown: notice the periodic inverted region and how it degrades as the distance from the silicon layer, the dark line on the bottom of the figure, increases. This effect is a direct evidence of the difficulties to produce such crystals.

1.2.1 OP-GaP Characterization

The basic experimental setup used to produce the 5.8 μm radiation by means of difference frequency generation is shown in Fig. 1.5. A single frequency Nd:YAG

[8] http://www.baesystems.com

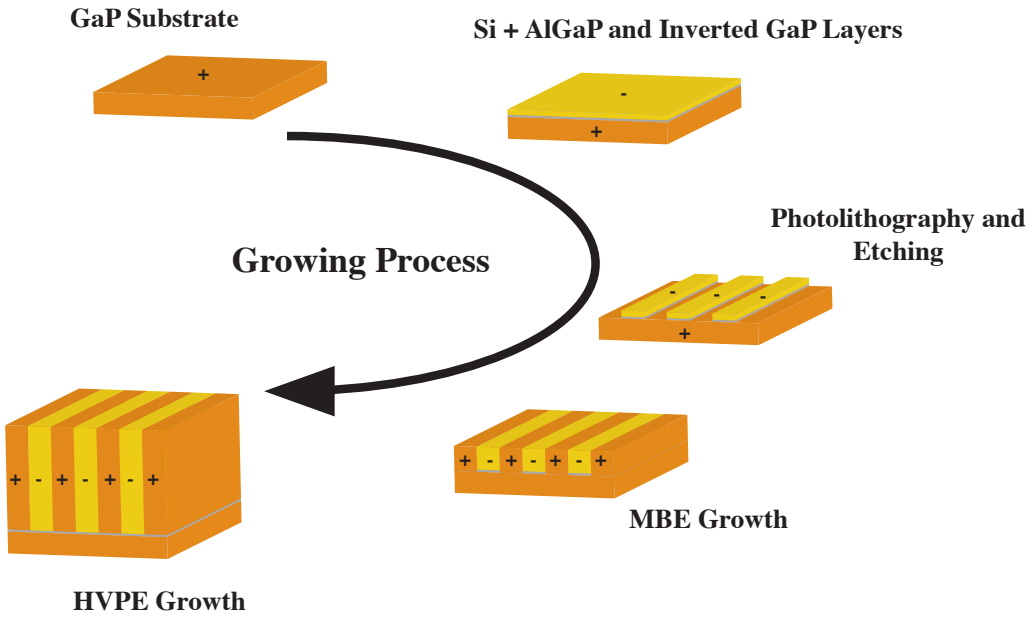

Figure 1.3: Growth and fabrication of orientation patterned gallium phosphide crystals.

Table 1.2: Geometrical and optical characteristics of the two crystal samples.

Crystal length CS1 (CS2)	24.6 (11.5) mm
Crystal section	6.0x1.8 mm^2
Substrate thickness	400 μm
Patterned region thickness	400 μm
Pattern period	24 μm
Duty cycle	50 %
AR coating	Both facets
Coating reflectivity	$< 0.5\%$ 1064 nm
	$< 0.5\%$ 1300 nm
	$< 0.3\%$ 5850 nm

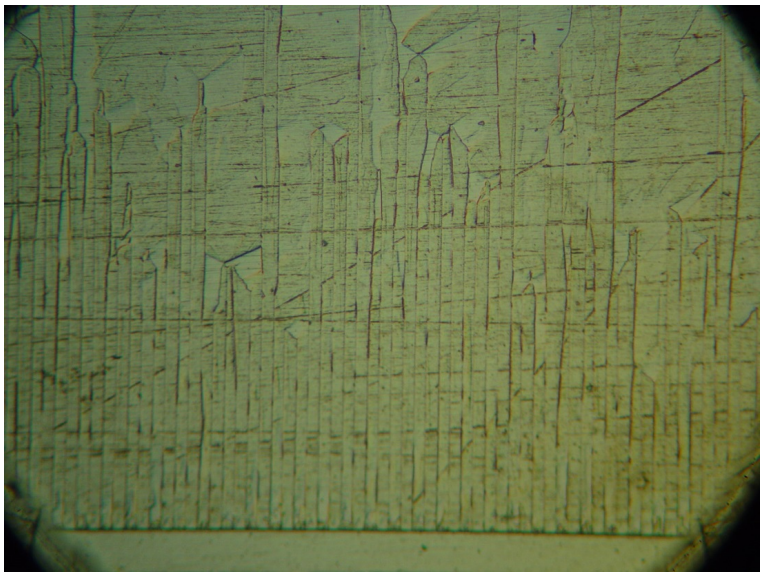

Figure 1.4: Orientation patterned region. The grating period is 24 μm. The dark line on the bottom is the silicon layer deposited during the growing process. Both the substrate and the patterned region are about 400 μm thick.

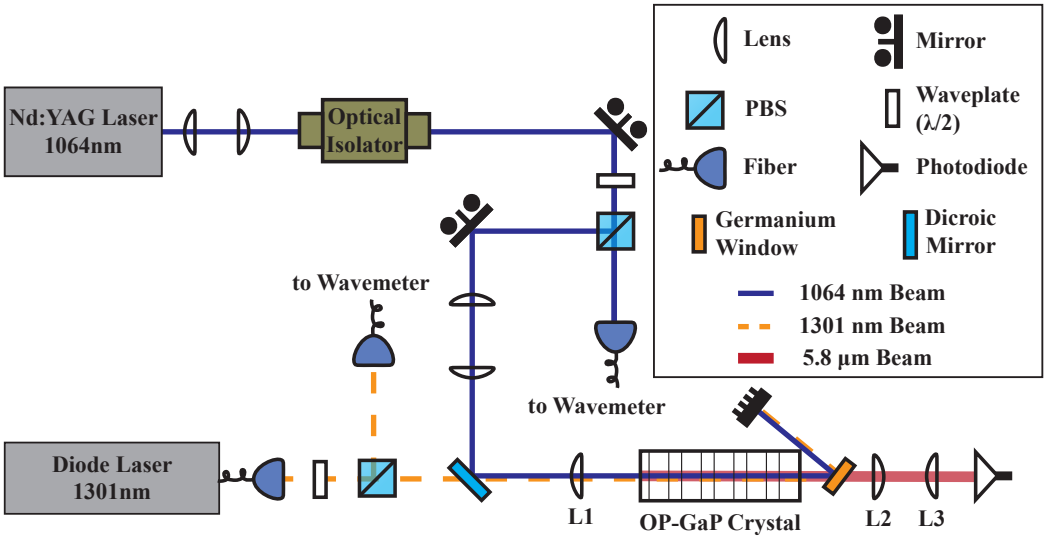

Figure 1.5: Experimental scheme to obtain difference frequency generation in the OP-GaP crystal. Two lasers emitting at 1064 nm and 1301 nm are combined in a dichroic mirror and focused on the crystal by means of lens L1. A Germanium window is used to separate the pump and signal beams from the idler, which is collected by lens L2 and focalized into a 200 μm active area HgCdTe detector by lens L3.

laser (InnoLight GmbH, Mephisto MOPA 55W, $\Delta\nu \sim 1$ kHz over 100 ms), hereafter called pump laser, is used to provide up to 10 W of continuous wave, linearly polarized radiation at $\lambda_p \simeq 1064$ nm. An extended cavity tunable fiber coupled diode laser (Toptica Photonics AG, DL PRO, $\Delta\nu \sim 100$ kHz), hereafter called signal laser, is used to provide up to 50 mW of linearly polarized, cw radiation at $\lambda_s \simeq 1301$ nm. The pump laser, collimated using a Keplerian telescope, passes first through an optical isolator. The beam is then split into two arms by means of a polarizing beam splitter: a small part of the light is sent to a wave meter (Bristol Instruments, Inc., Wavelength Meters 671 Series NIR) while the remaining light is sent to the crystal. Similarly the diode laser is split into two collimated arms: one is sent to the wave meter and the other one is sent to the crystal. The pump and signal beams, nearly TEM_{00}, are superimposed by a dichroic mirror and coaxially focalized with a plano-convex lens (L1) on the crystal. In the test and optimization procedure of the DFG process, four different values for the L1 focal length have been used: $f = 50$, 75, 100 and 150 mm. After the crystal, a germanium window is used to separate the idler from the two near-IR beams. As the mid-IR radiation exiting the crystal is strongly divergent, a calcium fluoride lens (L2) is used to collect and collimate the idler beam. The radiation is then focused on a thermoelectrically cooled HgCdTe detector with 200 μm active area (Vigo System S. A., PVI-4TE-5/MIP-DC-10M) by means of lens L3. All the beams are linearly polarized: the pump and signal wave are polarized vertically (along the [001] crystallographic axis) and horizontally (along [110]), respectively, yielding an horizontally polarized idler radiation. This configuration ensures a full coupling of the nonlinear coefficient d_{123}, indicated also as d_{14} in the contract notation often used in literature. The absolute responsivity of the HgCdTe detector is calibrated at 5.8 μm using a calibrated radiometer. A quantum cascade laser, emitting at the same frequency as the idler beam, is carefully aligned on the Vigo detector and on the radiometer by means of a flip mirror. The QCL output is scanned from 2 μW to 60 μW, as measured with the radiometer. The absorption and reflection of the different optics used in the two beam paths are taken into account and the power is corrected accordingly. Figure 1.6 shows the voltage reading on the HgCdTe detector as a function of the power measured with the radiometer. From a linear fit of the experimental data we extract a responsivity of $(56.5 \pm 1.1) \cdot 10^{-3}$ μW/mV at ~ 6 μm of the Vigo detector.

The OP-GaP crystal is housed inside a massive copper block whose temperature is stabilized by a digital PI servo controller from room temperature to 200° Celsius. The crystal-oven system is then mounted on a XYZ-$\theta\phi$ manipulator to optimize the alignment with the optical beams. Since the nonlinear efficiency is strongly dependent on the superposition of the pump and signal beams, the telescope on the pump path allows for matching the beam waists. The telescope is finely adjusted to maximize the idler power.

As shown in Eq. 1.35, the aperture function has a crucial role in the determination of the nonlinear process efficiency and has to be correctly estimated. The two key parameters for the correct evaluation of the aperture function are the shape and the

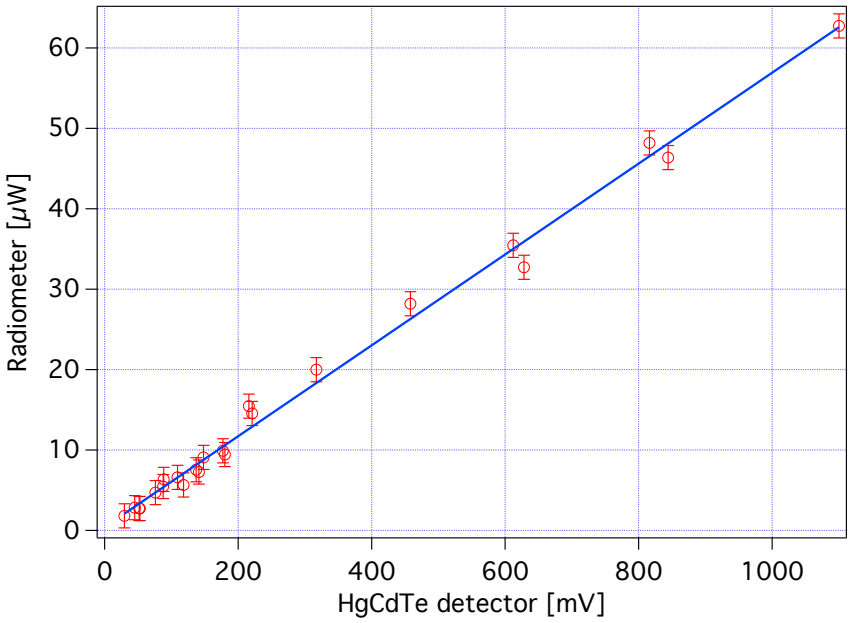

Figure 1.6: HgCdTe detector absolute responsivity calibration. A QCL power at $\sim$ 6 μm is measured simultaneously with a calibrated radiometer and with the HgCdTe detector. The line is a linear fit on the experimental data. The measured responsivity at ~ 6 μm is $(56.5 \pm 1.1) \cdot 10^{-3}$ μW/mV.

waist of the beams. While the beam shapes are close to TEM_{00} thanks to the type of laser that were used, the beam waists had to be accurately measured using the calibrated pinhole technique [65], in which the power transmitted through a set of diameter-calibrated pinholes is measured. An XYZ translator is used to adjust the pinhole positions. We can calculate the transmission factor T of a circular aperture of diameter ϕ coaxial to a Gaussian beam of waist w_0 as

$$T(\phi, w_0) = \frac{2}{\pi w_0^2} \int_0^{\phi/2} 2\pi r \exp\left(-\frac{2r^2}{w_0^2}\right) dr \tag{1.46}$$

If the transmission factor T is experimentally measured for a value of ϕ and the pinhole is not too small compared to the beam area, we can derive the waist from the relation

$$w_0 = \left[-\frac{\phi^2}{2\ln(1-T)}\right]^{1/2} \tag{1.47}$$

For each beam, the waist was measured by using several pinholes with different diameters. The measurements are consistent with each other within a 10 % uncertainty. The averaged values are reported in Tab. 1.3, together with the calculated idler waist and Rayleigh range following Eq. 1.36. The measurements satisfy the relation $w = (4/\pi)\lambda f/D$, where D is the beam diameter and f the focal length

Table 1.3: Experimental values of waist for pump (w_p) and signal (w_s) laser at different focusing conditions for maximal idler power. The waists are measured using the calibrated pinhole techniques from which we get an uncertainty of 10 %. $w_\mathrm{i} = w_\mathrm{p} w_\mathrm{s}/(w_\mathrm{p}^2 + w_\mathrm{s}^2)^{1/2}$ is the calculated idler waist and $z_\mathrm{i} = k_\mathrm{i} w_\mathrm{i}^2/2$ is the calculated Rayleigh range, where $k_\mathrm{i} = 2\pi n_\mathrm{i}/\lambda_\mathrm{i}$ is the wave vector. For the GaP crystal we assumed a refractive index at 5.83 μm of $n_\mathrm{i} = 3.18$ [66].

f [mm]	w_p [μm]	w_s [μm]	w_i [μm]	z_i [mm]
150	67	82	52	4.7
100	45	55	35	2.1
75	27	33	21	0.75
50	19	23	15	0.37

of the lens L1, with a ratio $w_\mathrm{s}/w_\mathrm{p} \approx \lambda_\mathrm{s}/\lambda_\mathrm{p}$. Although such a waist ratio does not correspond to the equal confocal parameter focusing condition, which theoretically yields optimal efficiency, it is sufficiently close to it. In Eq. 1.35, the exponential term and the aperture function take into account the absorption of the pump and signal waves, as well as the idler one, in the so called normalized absorption coefficient $\mathfrak{a}$. For this reason we measure the absorption for the pump and signal waves[9], obtaining an average absorption coefficients of $\alpha_\mathrm{p} \approx 0.17$ cm^{-1} and $\alpha_\mathrm{s} \approx 0.12$ cm^{-1} inside the 400 μm thick orientation patterned region. In the substrate much higher coefficients are found: $\alpha_\mathrm{p} \approx 0.58$ cm^{-1} and $\alpha_\mathrm{s} \approx 0.53$ cm^{-1}. The reason of this difference is that the substrate is grown by means of a Czochralski process[10] in which there is a contamination due to unintentional impurities which are not present in the high-purity vapor-grow (HVPE) material. The idler absorption coefficient is assumed to be $\alpha_\mathrm{i} \approx 0.007$ cm^{-1}, value measured using a Perkin Elmer Spectrum GX FTIR as reported in [59].

In order to derive the efficiency of the nonlinear process, the absolute idler power is measured as a function of the pump power for a fixed signal power of 40 mW (45 mW) with the CS1 (CS2) crystal. The results of these measurements are shown in Fig. 1.7 for both crystals. Each curve on the two plots corresponds to one of the focusing conditions summarized in Tab. 1.3. The error bars represent a relative uncertainty of 5 %, which is mainly due to the uncertainty in the pump power reading and to the uncertainty associated to the responsivity of the Vigo detector. For the idler power estimation, spurious losses due to the germanium filter and the

[9]The absorbing coefficients are written with subscript s and p indicating the signal and pump radiation respectively, not to be confused with the s and p polarization.

[10]The Czochralski process is a method of crystal growth used to obtain single crystals of semiconductors or metals. High-purity, semiconductor-grade silicon is melted in a crucible in which a seed crystal is dipped into. The seed is slowly pulled upwards and rotated simultaneously and a large crystal is then obtained.

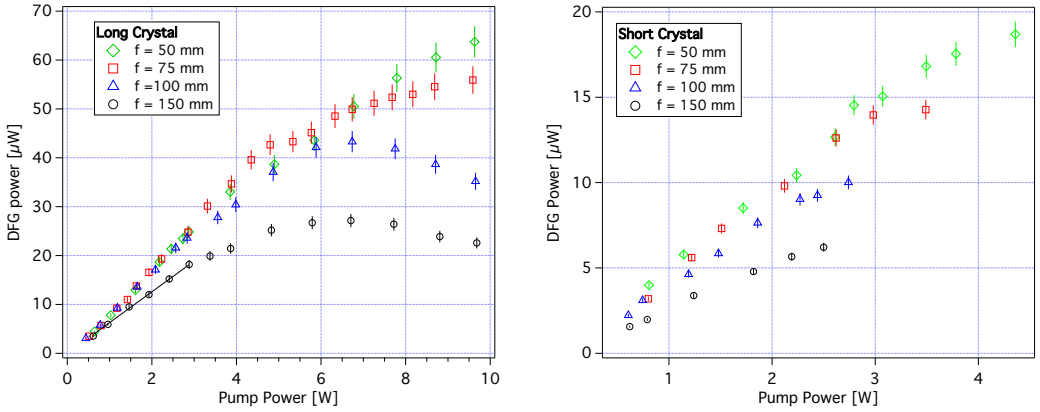

Figure 1.7: Idler power generated as function of the pump power with the long crystal, CS1, (left) and with the the short crystal, CS2, (right). The signal power is kept constant over the measurements at around 40 mW and 45 mW with the long and short crystal, respectively. For each point the crystal temperature is optimized to achieve the best phase matching. The data show a linear slope at low pump powers, where they can be fitted with a line. An example of such a fit is shown for the loosest focusing data set of the long crystal, CS1. The slope of this line is used to calculate the conversion efficiency $\eta_{\mathrm{DFG}} = P_{\mathrm{i}}/(P_{\mathrm{p}}P_{\mathrm{s}})$ plotted in Fig. 1.8.

two CaF_2 lenses have been considered. The short crystal was used only for initial tests and it was characterized up to about 4 W of pump power. The 24.6 mm long sample, instead, has been completely characterized up to 10 W of pump power, this limit being set by the damage threshold of the antireflection coating on the crystal facets. If we take into account the different lengths of the samples, both of them show a very similar behavior. In the following, only the measurements with the long crystals are discussed.

The maximum generated idler power is around 65 μW with slightly less than 10 W of 1064 nm and 40 mW of signal power. The highest efficiency is achieved for the strongest focusing case, corresponding to a $f = 50$ mm L1 lens. Nevertheless, the curve obtained for $f = 75$ mm is almost overlapped to the previous case, meaning that both these two focusing conditions must be close to the optimum value for the difference frequency generation process. The non negligible absorption of the GaP at the two input waves results in an heating of the material and consequently in a modification of local index of refraction, affecting the quasi-phase matching condition. Heating is mainly due to absorption of the pump beam, because of its high power and higher absorption coefficient. Absorptions at 1064 nm and at 1301 nm are around 35% and 25%, respectively. In all measurements this effect is partially corrected by adjusting the crystal temperature to maximize the generated power. As expected, the optimal generation efficiency is found at a lower crystal temperature as the pump power increases. A second effect arise from the finite thermal conductivity

of the material that yields a transverse temperature gradient $\Delta T(r)$, with r the radial coordinate transverse to the propagation axis of the incident beams. Such gradient spatially changes the quasi-phase matching condition. When the pump power is low, the QPM condition is satisfied throughout the whole beam volume, i.e. for any radial coordinate r. At higher pump powers, though, the QPM condition cannot be satisfied for all r. The temperature of any ring with radius r is different from the temperature of a ring with radius r' and, since the phase-match is temperature dependent, this effect leads to a position-dependent dephasing. Unfortunately, there is no way to recover the phase matching condition and the resulting effect is that the DFG power saturates or even decreases. In Fig. 1.7 the saturation effect due to thermal effect is clearly visible for increasing pump power, whereas a linear behavior would be expected for not absorbing crystals over the entire graph.

In order to derive the nonlinear coefficient d_{14}, only the linear portion of the plots shown in Fig. 1.7 are taken into account. In this way the thermal effects do not affect the analysis. The nonlinear coefficient d_{14} can be derived from the efficiency of nonlinear generation using the Eq. 1.35, which we repeat here

$$\eta_{DFG} = \frac{8\omega_{\mathrm{i}}^2 d_{14}^2 L}{\pi\epsilon_0^3 c^3 n_{\mathrm{p}} n_{\mathrm{s}} n_{\mathrm{i}}} \exp(-\alpha_{\mathrm{i}} L)(k_{\mathrm{s}}^{-1} - k_{\mathrm{p}}^{-1})^{-1} h(\mathfrak{a}, \mathfrak{l}, \mathfrak{f}, \mathfrak{s})$$

To compare this relation with the experimental data, the focusing function $h(\mathfrak{a}, \mathfrak{l}, \mathfrak{f}, \mathfrak{s})$ has to be optimized (maximized) over the phase mismatch $\mathfrak{s}$ and waist location $\mathfrak{f}$ to obtain the optimal function $< h >_{\mathfrak{s},\mathfrak{f}}$. This reproduces the experimental optimization procedure performed over the waists position, overlapping and size. This optimization procedure is carried out numerically using an adaptive step size algorithm[11] tracking the maximum of h. The results of the numerical simulations are shown in Fig. 1.8 together with the experimental data. Each point reported in the graph represents the slope of a curve from Fig. 1.7, expressed as conversion efficiency $\eta_{\mathrm{DFG}} = P_{\mathrm{i}}/(P_{\mathrm{p}} P_{\mathrm{s}})$, in function of the focusing parameter $\mathfrak{l} = L/z_{\mathrm{Rd}}$. The focusing parameter depends, via z_{Rd}, on the focal length of the lens L1.

For the comparison we have considered only the $f = 100$ and $f = 150$ mm loose focusing data for which the modes of all three waves are confined within the active QPM layer volume, for reasons which will be stated further. Deriving the nonlinear coefficient d_{14} from the term η_{DFG} that appears in the Eq. 1.35 and using the Eq. 1.45, we obtain

$$d_{\mathrm{eff}} = \frac{2}{\pi} d_{14} = (17 \pm 3) \text{ pm/V} \tag{1.48}$$

using the experimental data from both crystals.

The efficiency saturation observed for the two tight focusing data can be related to the limited thickness (400 μm) of the patterned layer. If we consider a Gaussian

[11] We thank Prof. Jean-Jacques Zondy from Nazarbaev University in Astana (Kazakhstan) for running the simulations.

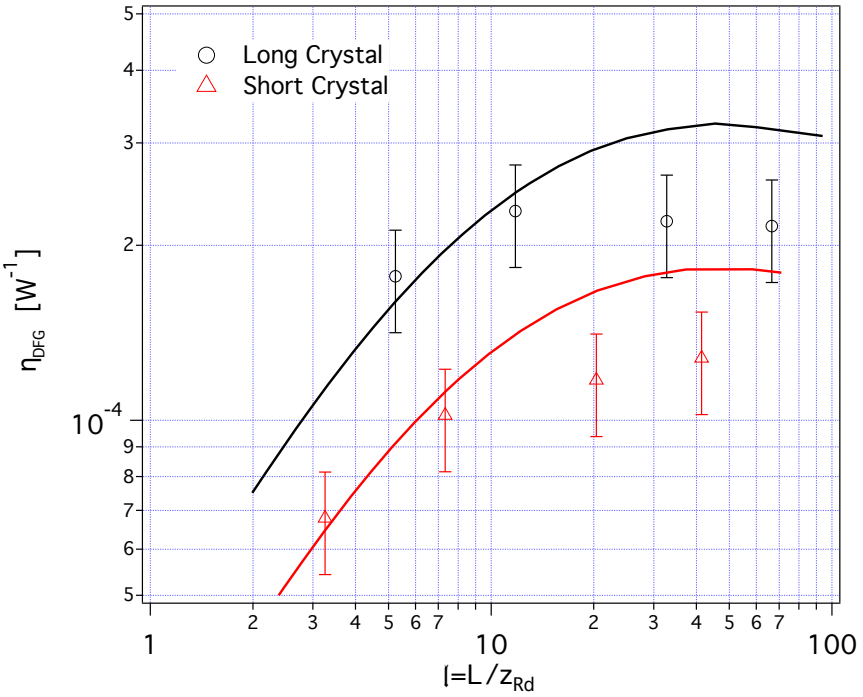

Figure 1.8: Conversion efficiency $\eta_{\mathrm{DFG}} = P_{\mathrm{i}}/(P_{\mathrm{p}}P_{\mathrm{s}})$ as function of the focusing parameter $\mathfrak{l} = L/z_{\mathrm{Rd}}$ that expresses the crystal length in units of the Rayleigh length of the idler. The points represent the experimental data while the solid line shown the optimized theoretical efficiency calculated with the waist ratio $w_{\mathrm{s}}/w_{\mathrm{p}} = \lambda_{\mathrm{s}}/\lambda_{\mathrm{p}}$. In red and in black are shown the data and simulation relative to the short and long crystals respectively.

TEM_{00} beam, the far field divergence angle θ can be described by the relation $\theta = \lambda/(\pi n w_0)$ where n and w_0 are the refractive index and the waist of the radiation at wavelength λ. It is easy to demonstrate that the pump and the signal waves remain confined inside the inverted domain region over the whole crystal length at any focusing conditions for both the two crystal samples. This is not the case for the $\lambda_i \simeq 6$ μm idler beam: in reference to the data reported in Tab. 1.3, we can calculate a mean idler beam diameter of 690 μm and 990 μm at the output facet ($z = L/2$) of the long crystal for the $f = 75$ mm and $f = 50$ mm respectively. The same calculation can be performed for the shorter crystal resulting in an output beam of 320 μm and 460 μm mean diameters. Thus, during the propagation towards the output facet, the idler beam expands outside the orientation patterned layer into the bulk region where the absorption is larger and the QPM condition is no longer satisfied. Consequently, the difference between the idler's phase and the sum-phase of pump and signal is not strictly identical within and outside the QPM layer, affecting thus the overall phase coherence of the DFG process along the crystal at tight focusing compared to the looser focusing cases where all three waves remain quasi-phase matched over the whole crystal length. These interpretations of the possible cause of η_{DFG} saturation under too tight focusing can be checked in future by using samples with identical lengths but with a thicker, i.e. $800-1000$ μm, orientation patterned layer.

Levine [67] reported the values of $d_{14} = (37 \pm 2)$ pm/V at 10.6 μm, $d_{14} = (49 \pm 9)$ pm/V at 1.32 μm and $d_{14} = (47 \pm 10)$ pm/V at 2.12 μm using different non-phase-matched techniques. Shoij et al. [68] measured the second-order nonlinear optical coefficient d_{14} of GaP by means of non-phase matched SHG using the wedge technique[12]. In that work, a couple of wedged GaP crystal are pumped at 1313 nm and the generated radiation is collected in a photomultiplier tube taking into account the multiple reflection effects: they reported the most accurate value to date for the nonlinear d_{14} coefficient $d_{14} = (36.8 \pm 4)$ pm/V.

Since the d-coefficients are wavelength dependent, the value reported by Shoji has to been rescaled to our idler wavelength. R. C. Miller empirically noted that while the d-value depends on wavelength, if rescaled with the opportune function of refractive indexes, it yields a constant value which is called Miller's Delta [71]. The

[12]The nonlinear material is machined to a wedge with an apex angle of around 2°–3°and with a thickness at the base of the prism around few to tens times the coherence length l_c. This crystal is then placed perpendicular to the incident laser that induce the second-harmonic generation process. As already mentioned before, when phase matching condition is not satisfied, the phase difference between the pump and the generated light results in oscillation of the SH power when the thickness of the crossed nonlinear material changes. If the generated power is reported as function of the crystal position, the nonlinear coefficient can be derived from the oscillations amplitude. A reference crystal with well known nonlinearity is used to calibrate the second-harmonic signal [69], [70].

Table 1.4: Coefficients for the Sellmeier equation relative to gallium phosphide.

Coefficient	Value
A	2.78649
B	6.32098
C	$1.02{\cdot}10^{-6}$ [$^{\circ}\mathrm{C}^{-1}$]
D	0.29903 [μm]
E	$5.92{\cdot}10^{-8}$ [μm $^{\circ}\mathrm{C}^{-1}$]
G	$9.18{\cdot}10^{-9}$ [$\mu\mathrm{m}^{-2}$ $^{\circ}\mathrm{C}^{-1}$]
H	-0.00307 [$\mu\mathrm{m}^{-2}$]
T_0	22.9 [$^{\circ}$C]

Miller's rule can be used to calculate the rescaling factor

$$M_{14} = \prod_{i=1}^{3} \frac{n^2(\lambda_\mathrm{i}) - 1}{n^2(\Lambda_\mathrm{i}) - 1} \tag{1.49}$$

where the Λ_i are the wavelengths used by Shoji's and λ_i the wavelengths used in our DFG process. In order to evaluate the rescaling factor, the precise index of refraction value of GaP at all the involved wavelengths has to be considered. Recently, a new temperature-dependent Sellmeier equation [59] has been derived based on recent refractive index data measured on a bulk GaP prism. The Sellmeier equation results in the following expression

$$\begin{aligned} n^2 &= A + \frac{(B + CF)\lambda^2}{\lambda^2 - (D + EF)^2} + (H + GF)\lambda^2 \\ F &= (T - T_0)(T + T_0 + 546.30) \end{aligned} \tag{1.50}$$

where the temperature is expressed in degree Celsius and the coefficients are listed in Tab. 1.4. Using the Eq. 1.49 in conjunction with Eq. 1.50 we obtain a rescaling factor of $M_{14} = 0.82$ that can be used to convert Shoji's d_{14} coefficient measured at 1.31 μm at our wavelength of 5.83 μm. The result of the rescaling is d_{14}^{Shoji}(5.83 μm)=30.2 pm/V. This value yields a $d_{\mathrm{eff}} = (19 \pm 2)$ pm/V, in good agreement with our experimental value.

To conclude the characterization of this new crystal, the tuning curves in dependence of the signal wavelength and crystal temperature are studied.

Fig. 1.9 shows the DFG tuning curve as a function of the crystal temperature. Two different data sets are displayed: the red squares refer to the tight focusing condition with $f = 75$ mm while the black circles to the loosest focusing conditions obtained with focal length of 150 mm. Since the crystal patterning period Λ depends on temperature, when the temperature changes the phase matching condition changes as well. Thus we should expect a drop in efficiency if the temperature

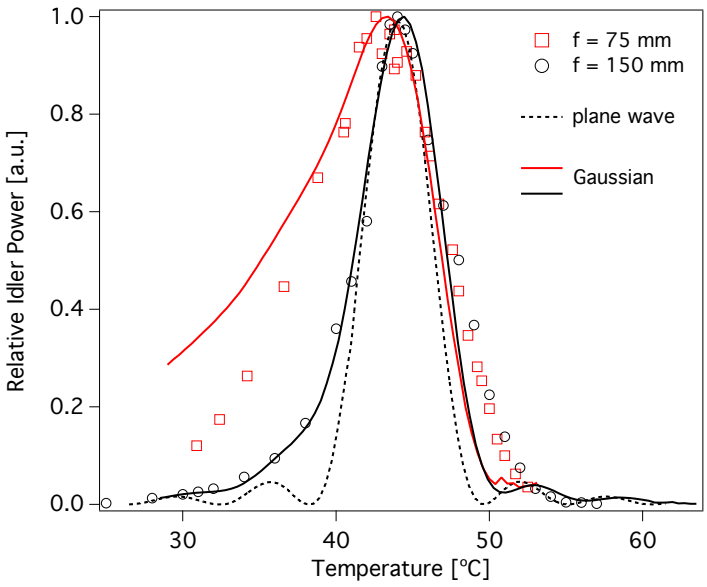

Figure 1.9: Temperature tuning curves reported for the strong and loose focusing conditions. The black round and the red squared markers refer to focal lengths of $f = 150$ mm and $f = 75$ mm respectively. The dashed line is the result of plane-wave theory while the solid lines show the fit over the experimental data using the Gaussian DFG theory. The idler power is normalized to unit.

drifts from the optimal value. In the plane wave approximation this effect is taken into account by the sinc function that appears in Eq. 1.26: when the temperature changes, the Sellmeier equation returns a different index of refraction, yielding a function $\Delta k(T)$. The dashed line in Fig. 1.9 shows the normalized idler generation efficiency as a function of the temperature dependent phase mismatch in plane wave approximation ($\approx \mathrm{sinc}^2(\Delta k(T)L/2)$: this curve shows a poor agreement with the experimental data, particularly with those for strong focusing. A better estimation can be obtained using Gaussian beam theory to take the focusing effect into account. Using Eq. 1.35 and introducing a temperature-dependent reduced parameter $\mathfrak{s}(T) = \Delta k(T) z_{\mathrm{Rd}}$ in the aperture function $h(\mathfrak{s}(T))$, the solid lines plotted in Fig. 1.9 are derived. In this case the main features of the experimental data as far as asymmetry and broadening are qualitatively predicted in both focusing conditions. Note how the beam aperture effect washes out the side lobes that are typical of the plane-wave tuning curve.

A similar analysis has been carried out for the dependence of the idler generation efficiency on the signal wavelength at fixed crystal temperature. The plane wave approximation is still proportional to the sinc term and for the Gaussian beam theory the aperture function has to be calculated for the reduced parameter $\mathfrak{s}(\lambda_{\mathrm{s}}) = \Delta k(\lambda_{\mathrm{s}}) z_{\mathrm{Rd}}(\lambda_{\mathrm{s}})$ that depends on the signal wavelength. In this case too, Gaussian beam theory correctly reproduces the main features of the experimental data, whereas the plane wave approximation fails. The two solid lines in Fig. 1.10 show narrow absorption dips corresponding to resonances with water transitions. Frequencies and intensities of the absorption lines are derived from the HITRAN online database[13], considering a 10-cm beam path in standard atmosphere, which is the distance travelled by the idler beam before reaching the MCT detector. We conclude that the thermo-optical Sellmeier equation reported in Eq. 1.50 is a reliable dispersion relation.

[13] http://hitran.iao.ru

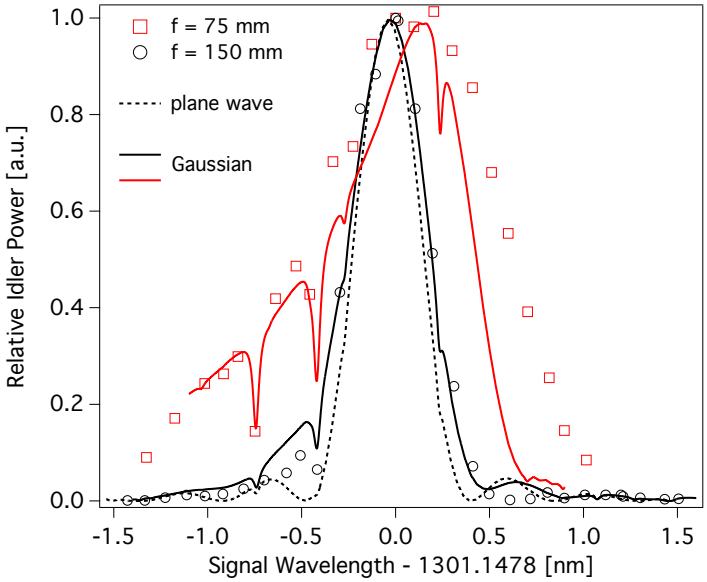

Figure 1.10: Signal wavelength tuning curves reported for the strong and loose focusing conditions. The black round and red squared markers refer to focal lengths of $f = 150$ mm and $f = 75$ mm respectively. The dashed line is the result of plane-wave theory while the solid lines show the fit over the experimental data using the Gaussian DFG theory taking into account the water absorption spectrum around 5.83 μm. The idler power is normalized to unit.

Chapter 2

Frequency Locking Chain

The mid-IR region of the electromagnetic spectrum is well covered by quantum cascade lasers. This compact devices are characterized by typical emitted powers of the order of tens of mW and tuning ranges of the order of hundreds of GHz. Their free running line width typically ranges from hundreds of kHz to several MHz, mainly due to the noise contributions from the QCL current driver and from temperature fluctuations. The frequency stabilization and reduction of their line width is therefore a mandatory step for applications in high resolution spectroscopy and new challenging experiments. Several techniques have been used to date to reduce the QCLs line width, such as frequency stabilization over sub-Doppler molecular transitions [32] or phase–locking to infrared frequency combs [72]. All these techniques have demonstrated the capability to achieve sub-kHz line widths. A drawback of these approaches is that a suitable molecular transition or a stable optical reference has to be available at the frequency of interest.

A different approach relies on locking the laser frequency to the narrow resonance of ultra-stable cavities with very high quality factors. Ultra-low expansion materials can be used to build ultra-stable cavities in the near infrared and mirrors with residual absorptions at the ppm level can provide finesses larger than 10^6. Unfortunately, as the laser wavelength increases towards the mid and far infrared, the efforts for realizing stable and high finesse cavities increase tremendously, mainly due to the difficulties in the development of mirror coatings and to the limitations due to substrate residual absorption. However, progress in the processing of high-purity materials, such as calcium fluoride, has reached the point where crystalline micro-resonators for mid infrared radiation with high finesse became possible.

During the last two years, we have demonstrated that it is possible to stabilize and narrow the line width of a QCL emitting at 4.3 μm by locking it to a high-Q ($> 10^7$) whispering galley mode micro-resonator (WGMR) [36, 41]. The emission frequency of the QCL laser was stabilized by means of an electronic locking achieving $\sim$10 kHz line width (full width at half maximum) over 1 second timescale, an unprecedented result for direct locking to a mid-IR optical resonator. The main

advantage of this apparatus, as compared to those using standard Fabry-Perot cavities, is that the micro-resonator works over the whole transparency range of the material used to realize the device: in case of calcium fluoride, it can be used from the UV to over 6 μm.

Another crucial condition for high-resolution spectroscopy is a reference to a frequency standard. The Global Positioning System (GPS) can be exploited to disseminate the frequency and typical accuracies of the order of 10^{-12} are achieved over one day average. If higher accuracy and stability is needed sophisticated local oscillators must be used. Nowadays, however, highly-stable and accurate frequency references can be delivered over hundreds of km by optical fibers from the national metrological institutes (INRIM in Italy, PTB in Germany, LNE-SYRTE in France, NPL in the UK and AGH in Poland). The instability of the optical signal transferred through the fiber networks is $1{\cdot}10^{-15}$ after one hour of averaging, while the instability of the fiber network itself is $1 \cdot 10^{-19}$.

Once a frequency standard is available, a frequency chain has to be built to reach the mid-infrared. There are various techniques to do so and they are mainly based on optical frequency combs. Unfortunately, the mid-IR spectral region is not covered by commercial combs and researchers are still exploring how to fill this gap [73]. State-of-the-art mid-IR optical combs are generated by nonlinear frequency conversion such as difference frequency generation in nonlinear crystals [74] or by parametric oscillation in optical micro-resonators [75, 76]. A more robust approach relies on the generation of mid infrared light by difference frequency of two near infrared laser, which are locked to an optical frequency comb. The power levels of DFG light are typically very low but suffice for phase-locking[1] QCLs.

2.1 The Optical Link

INRIM has developed a network of phase-stabilized fiber links reaching various laboratories. One branch of this network reaches the European Laboratory for Nonlinear Spectroscopy (LENS) in Sesto Fiorentino after 642 km of optical fiber. A basic sketch of this setup is shown in Fig. 2.1. The frequency of a fiber laser is kept at 194399.996 GHz ($\sim$1542.14 nm) with an uncertainty < 1 Hz by a double locking scheme. The short-term variations of the laser are stabilized by means of a Pound-Drever-Hall lock with a bandwidth slightly higher than 60 kHz to an ultra-low expansion glass (ULE) high-finesse Fabry-Perot cavity [77], while in the longer term the laser is phase-locked to an hydrogen maser with a bandwidth of 25 mHz through

[1] A phase-locked loop (PLL) is a feedback system where the signal to be stabilized, usually the beat note between two lasers, is compared to a stable radio-frequency reference (local oscillator) on a phase detector. In the most simple implementation this is an analog mixer in quadrature condition; in more sophisticated approaches it is a digital phase/frequency detector. It generates a phase error which is integrated by a proportional-integral loop. This feeds an actuator that maintains the beat note's phase constantly locked to the local oscillator's phase by acting on the frequency on the laser.

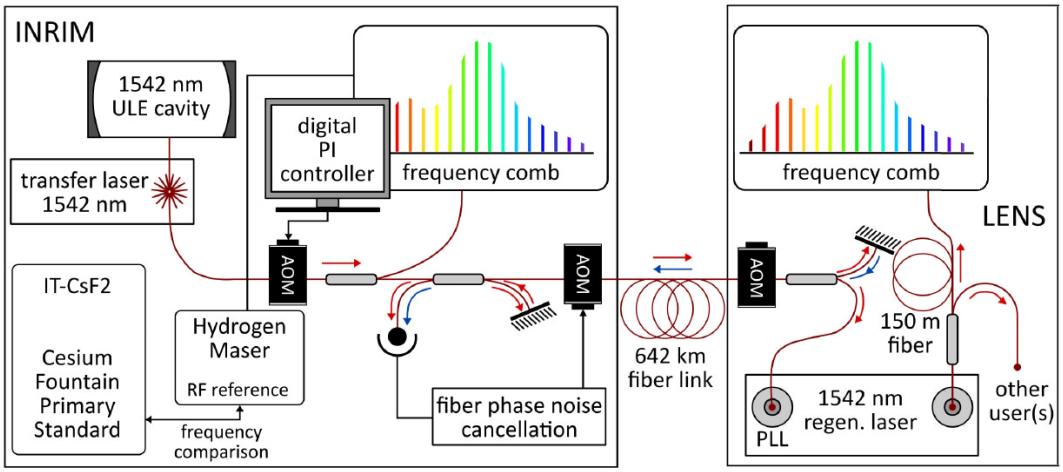

Figure 2.1: Sketch of the optical link setup. Left panel: generation of the optical link signal, frequency referenced to the Cs primary standard at INRIM (Turin). About 642 km of optical fiber connect the metrological institute to the end-user laboratory at LENS (Florence) where the optical reference is regenerated and distributed to different laboratories. In our case we use the regenerated radiation to stabilize an optical frequency comb.

an optical frequency comb. The hydrogen maser is used to reference and stabilize the optical frequency comb, which, in turn, is used to lock the frequency of the fiber laser. The stability of the laser is $3 \cdot 10^{-15}$ at one second. A periodic comparison of the hydrogen maser with a Cs fountain primary frequency standard ensures that the frequency of the fiber laser is known with an accuracy of $2 \cdot 10^{-16}$. This locking and comparison chain ensures excellent long term stability and SI-traceability. The optical reference laser is then disseminated through Italy via the optical fiber network. The 171-dB losses in the 642 km of optical path between INRIM and LENS are compensated by ten bidirectional erbium-doped fiber amplifiers [78]. One of the major challenges in the distribution of highly stable and accurate frequency over long distances is how to minimize the perturbations that occur all along the line. Any variation of the path length between the two end sites of the link results in a Doppler shift of the transmitted frequency: mainly temperature variations and vibrations over the line affect the transmitted frequency. These are compensated by a PLL that acts on the frequency of the transmitted laser [79, 80].

The stable fiber laser at INRIM is split into two arms: the first sends the light towards the remote laboratory through the fiber link while the second is locally back-reflected by means of a Faraday mirror that rotates the polarization of 90°. At LENS, the incoming light is frequency-shifted by 40 MHz by an acousto-optic modulator (AOM) and then it is again split into two portions: a part is the optical frequency reference while the remaining part is sent back to INRIM using a Faraday mirror. The light that goes back to Turin is shifted by 80 MHz because it passes

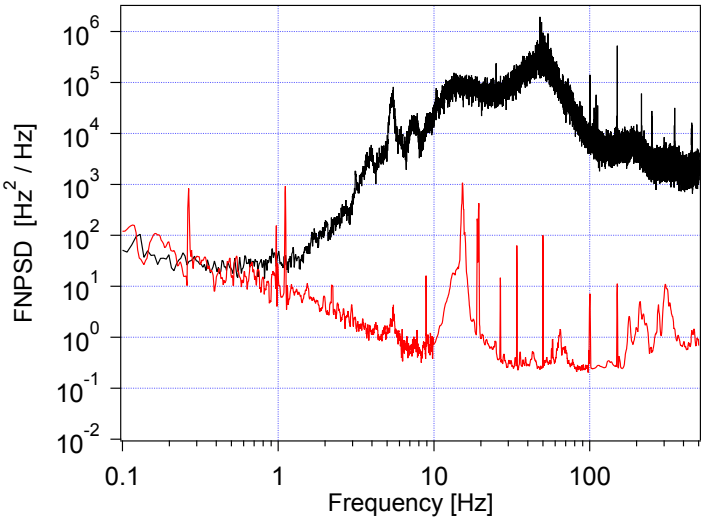

Figure 2.2: Measured frequency noise power spectral density (FNPSD) of the fiber link at LENS laboratories, 642 km away from the national metrological institute, and at INRIM in Turin. Red line: frequency noise of the fiber laser disciplined to the hydrogen-maser measured at INRIM. Black line: frequency noise of the comb-bridged beat note between a local laser at 1156 nm stabilized to a high-finesse ULE cavity and the fiber laser. Data from [77].

twice through the AOM. This allows to clearly distinguish the signal reflected back at LENS from the spurious back-reflections occurring along the path, which are not frequency-shifted. The round-trip light is then compared with the local one on a photodiode: the obtained beat note contains all the noise informations added by the 642 km fiber link and it is used to compensate any shift by means of a phase-lock loop that acts on a local AOM.

At LENS, the average power of the link signal is of a few nW over some mW of amplified-stimulated-emission background. This poor signal to noise ratio is dealt with a regeneration diode laser that is locked with a bandwidth of about 70 kHz at 100 MHz from the frequency sent over the fiber. This last laser is distributed over fibers to the end-user laboratories, placed in a range of 200 m. This allows to send up to about one mW of optical power to the end-users laboratories, a suitable power level for referencing an optical frequency comb.

The round trip delay time can be calculated as $\tau = nL/c = 6.4$ ms where $n = 1.468$ is the refractive index of the fiber that connects Turin to Florence, $L = 1284$ km is the round trip length and c is the speed of light in vacuum. This delay time reduces the maximum bandwidth on which the phase-lock loop can act to around 39 Hz.

Fig. 2.2 shows the frequency noise power spectral density of the reference fiber laser measured at INRIM and at LENS. The red line represent the frequency noise

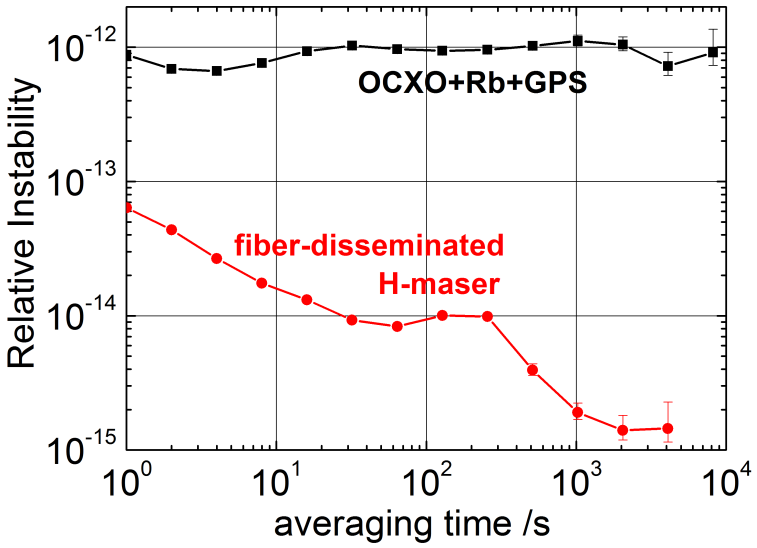

Figure 2.3: Relative instability of the optical frequency reference delivered to Florence compared with the stability of the local GPS-disciplined Rubidium-based local oscillator. OCXO stands for Oven Controlled Quartz Oscillator. Data from [81].

of the reference laser, disciplined to the hydrogen-maser, measured at INRIM by comparison with an independent cavity-stabilized laser. The black line represent the frequency noise of the beat note between the reference regenerated laser and a ULE-stabilized laser at 1156 nm through an optical frequency comb bridge. The presented data are taken from [77].

The relative instabilities of the disseminated optical frequency reference compared to the local GPS-disciplined Rubidium-based local oscillator at 10 MHz were characterized by INRIM and they are reported in Fig. 2.3. Over the long term, more than 1000 seconds, the optical reference signal is about three orders of magnitude more stable than the GPS-based reference.

2.2 Locking Scheme

The stability and accuracy of the fiber laser has to be transferred to the quantum cascade laser emitting at around 6 μm. This is not a trivial problem since there are about two octaves between the two frequencies. As we have seen in the first chapter, difference frequency generation allows to link the mid-IR radiation to two near-IR radiations at 1064 nm and 1300 nm. The wavelengths of these two lasers are less than 400 nm away from the reference laser and a frequency comb in the near infrared can bridge this gap.

In a frequency comb, the frequency[2] ν_m of a certain tooth is the sum of the so-

[2]In the following text we indicate with ν the optical frequencies and with f the radio-frequencies.

called carrier-envelope offset frequency f_{ceo} with the product of the tooth number N_m by the repetition rate f_{rep}:

$$\nu_{\text{m}} = f_{\text{ceo}} + N_m f_{\text{rep}} \tag{2.1}$$

Using a frequency comb it is also possible to know the exact frequency of any laser that has an emission frequency inside the range of the comb simply by measuring the beat note between a comb tooth and the laser. Furthermore, if the comb parameters, i.e. f_{rep} and f_{ceo}, are referred to a frequency standard, absolute frequency measurements can be performed. The practical way to do this is to lock the repetition rate of the comb so that the beat note of a tooth to the optical frequency reference distributed by the metrological institutes is fixed. Also the offset frequency has to be stabilized but it is less critical since $N_m f_{\text{rep}}$ is several orders of magnitude bigger than f_{ceo}.

To link two optical frequencies to a comb, in our case the pump and the signal lasers involved in the DFG process, the easiest way is by measuring their beat note with the respective closest comb tooth. If we indicate the 1064 nm laser frequency with ν_{p} and the 1300 nm laser frequency with ν_{s}, where the subscript p and s stand for pump and signal, we can express these absolute frequencies in terms of the comb parameters as

$$\begin{aligned} \nu_{\text{p}} &= f_{\text{ceo}} + N_{\text{p}} f_{\text{rep}} + f_{\text{p-c}} \\ \nu_{\text{s}} &= f_{\text{ceo}} + N_{\text{s}} f_{\text{rep}} + f_{\text{s-c}} \end{aligned} \tag{2.2}$$

where $f_{\text{p-c}}$ and $f_{\text{s-c}}$ are the frequencies of the beat notes between the pump and signal lasers with the comb teeth, respectively. Notice that all quantities have to be considered with the proper sign. Only f_{rep} and the lasers absolute frequencies are necessarily positive terms. We want to stabilize the frequency difference $\nu_{\text{p}} - \nu_{\text{s}} = \nu_{\text{i}}$ that correspond to light in the mid-IR. Thus, from Eq. 2.2 we have

$$\nu_{\text{i}} = \nu_{\text{p}} - \nu_{\text{s}} = (N_{\text{p}} - N_{\text{s}}) f_{\text{rep}} + f_{\text{p-c}} - f_{\text{s-c}} \tag{2.3}$$

We notice that f_{ceo} cancels out in the difference between pump and signal frequency. To simplify the description of the locking scheme that we have adopted, let us first consider the case of an ideal comb with fixed f_{rep}. In this case, the idler frequency can be kept constant by locking the quantity $(f_{\text{p-c}} - f_{\text{s-c}})$ because the term $(N_{\text{p}} - N_{\text{s}}) f_{\text{rep}}$ must be constant. The value $f_{\text{p-c}} - f_{\text{s-c}}$, namely the frequency variations of one laser with respect to the other, contains all the informations the PLL needs. For this reason one of the two lasers, say the pump laser, could in principle run unlocked (provided its free-running bandwidth is narrow enough), while $f_{\text{p-c}} - f_{\text{s-c}}$ is kept constant by acting only on the other laser, the signal in this case. However, this is impractical because the beat note frequency between the pump laser and the comb has always to be inside the limited bandwidth of the detector. Further, to avoid unnecessary action on the driver of the pump laser if the laser had to follow instabilities in f_{ceo}, the frequency is usually locked using $\bar{f}_{\text{p}} = f_{\text{p-c}} + f_{\text{ceo}}$ with the sign of $f_{\text{p-c}}$ opposite with respect to the term f_{ceo} as a signal for the PLL. Once $\bar{f}_{\text{p}}$

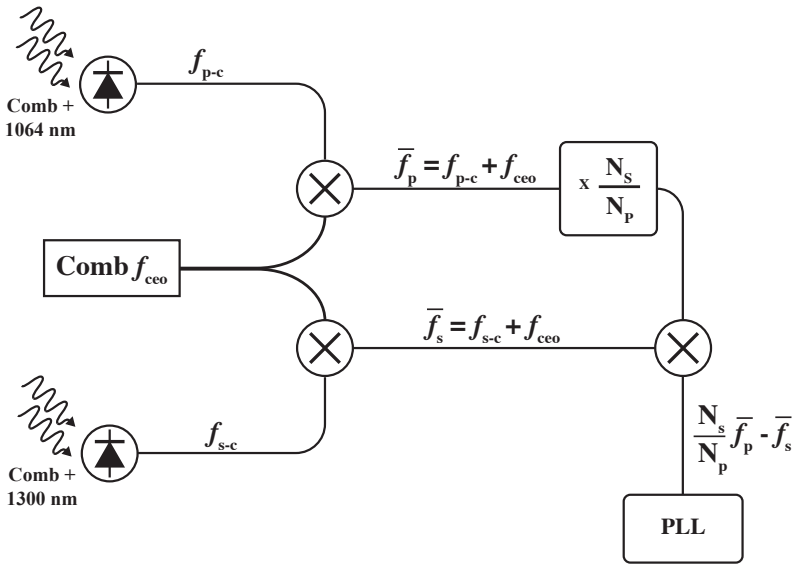

Figure 2.4: Basic signal processing scheme used to lock two optical frequencies by means of the so-called virtual beat note approach.

has been generated, the same can be done for the signal laser and the difference frequency for the phase-lock loop is thus generated as $\bar{f}_\mathrm{p} - \bar{f}_\mathrm{s}$, which is identical to Eq. 2.3.

If a real comb is used instead, where the stability of f_rep is finite, one immediately sees from Eq. 2.3 that the difference of the beat notes is not a good signal for the phase-lock loop because the term $(N_\mathrm{p} - N_\mathrm{s})f_\mathrm{rep}$ is not constant anymore. A conceptual difficulty arises from the fact that a variation of $\bar{f}_\mathrm{p}$ could either be due to a drift in the frequency of the pump laser or to a drift of the comb repetition rate. The appropriate correction to apply to the frequency of the signal laser to keep the difference frequency constant would be a shift of equal size and sign in the first case, but a shift scaled by $N_\mathrm{s}/N_\mathrm{p}$ in the latter case, because of the stretchable-ribbon-like behavior of optical frequency combs. A simple solution is available if the pump laser has a good short-term stability and can thus be loosely locked to a comb's tooth (lock bandwidth of, say, 100 Hz). Then, the PLL for the signal laser can be closed on

$$\frac{N_\mathrm{s}}{N_\mathrm{p}}\bar{f}_\mathrm{p} - \bar{f}_\mathrm{s} \tag{2.4}$$

with a much tighter lock. This procedure was proposed by H. R. Telle on 2002 and it is thoroughly described in [82]. Fig. 2.4 shows the conceptual signal processing scheme of this method. Now we want to derive an expression that describes how the different noise contribution are transferred to the idler radiation. The noise on the comb offset is irrelevant because the idler frequency does not depend on it. Three noise contributions have to be considered, coming from the comb repetition rate f_rep

and from the two optical frequencies ν_p and ν_s. Using Eq. 2.2 we can express these virtual frequencies $\bar{f}_\mathrm{p}$ and $\bar{f}_\mathrm{s}$ as

$$\bar{f}_\mathrm{p} = f_\mathrm{p\text{-}c} + f_\mathrm{ceo} = \nu_\mathrm{p} - N_\mathrm{p} f_\mathrm{rep} \tag{2.5}$$

and

$$\bar{f}_\mathrm{s} = f_\mathrm{s\text{-}c} + f_\mathrm{ceo} = \nu_\mathrm{s} - N_\mathrm{s} f_\mathrm{rep} \tag{2.6}$$

Now, we can write the Eq. 2.4 as

$$\frac{N_\mathrm{s}}{N_\mathrm{p}}\bar{f}_\mathrm{p} - \bar{f}_\mathrm{s} = \frac{N_\mathrm{s}}{N_\mathrm{p}}(\nu_\mathrm{p} - N_\mathrm{p} f_\mathrm{rep}) - \nu_\mathrm{s} + N_\mathrm{s} f_\mathrm{rep} = \frac{N_\mathrm{s}}{N_\mathrm{p}}\nu_\mathrm{p} - \nu_\mathrm{s} \tag{2.7}$$

or

$$\nu_\mathrm{s} = \frac{N_\mathrm{s}}{N_\mathrm{p}}\nu_\mathrm{p} - \frac{N_\mathrm{s}}{N_\mathrm{p}}\bar{f}_\mathrm{p} + \bar{f}_\mathrm{s} \tag{2.8}$$

and ν_i is

$$\nu_\mathrm{i} = \nu_\mathrm{p} - \nu_\mathrm{s} = \nu_\mathrm{p}\left(1 - \frac{N_\mathrm{s}}{N_\mathrm{p}}\right) + \left(\frac{N_\mathrm{s}}{N_\mathrm{p}}\bar{f}_\mathrm{p} - \bar{f}_\mathrm{s}\right) \tag{2.9}$$

Following the arguments previously exposed, we can use a phase-lock loop with high bandwidth to stabilize the term $N_\mathrm{s}/N_\mathrm{p}\bar{f}_\mathrm{p} - \bar{f}_\mathrm{s}$ to an external radio-frequency acting only on the signal laser and a very loose lock to stabilize the pump frequency to the comb tooth.

To derive the frequency noise of the idler radiation it is commonly adopted the notation in terms of frequency noise power spectral density[3] (FNPSD) $S_\nu(f)$ [83], that for the previous relation results in

$$S_{\nu,\mathrm{idler}}(f) = S_{\nu,\mathrm{pump}}(f)\left(1 - \frac{N_\mathrm{s}}{N_\mathrm{p}}\right)^2 + S_{\nu,\mathrm{LockSignal}}(f) \tag{2.10}$$

in which we have considered the noise of the pump laser independent from the noise introduced by the lock that acts on the signal laser $S_{\nu,\mathrm{LockSignal}}(f)$. If we consider the case in which the term $S_{\nu,\mathrm{LockSignal}}(f)$ is much smaller then the term $S_{\nu,\mathrm{pump}}(f)$, it follows that the stability of the pump near-IR laser is directly transferred to the mid-IR laser. In addition, the term $(1 - \frac{N_\mathrm{s}}{N_\mathrm{p}})^2$, that is less than one, acts in a way that only a fraction of the instabilities are transferred, resulting in a less noisy idler beam.

We have described the principle of the virtual beat note scheme. In the following the practical implementation is discussed. Fig. 2.5 shows the optical setup. This setup is an extension of the setup presented in Chapter 1 that was used to characterize the new OP-GaP crystal. All technical informations about the laser sources and optical components are to be found there.

[3] Alternatively, the phase noise power spectral density $S_\phi(f)$ can be used, which is related to $S_\nu(f)$ by the relation $S_\nu(f) = f^2 \cdot S_\phi(f)$.

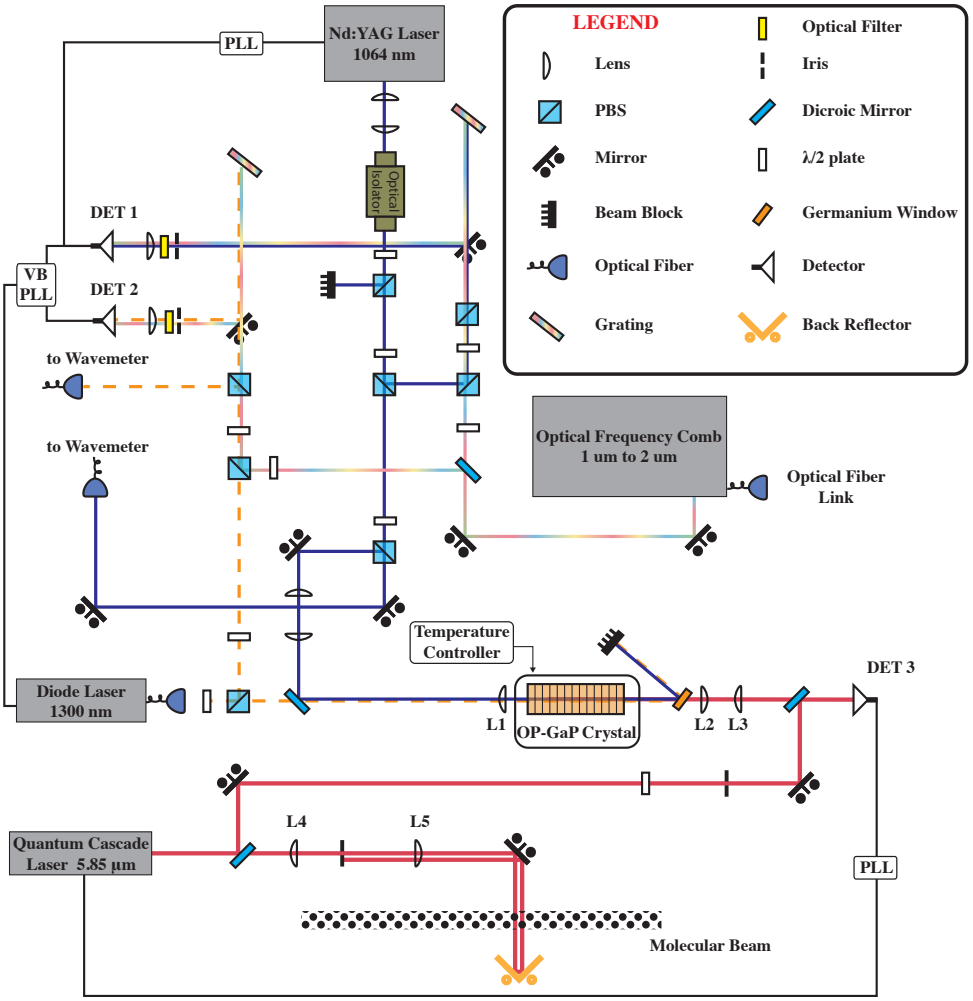

Figure 2.5: Optical setup used to generate radiation at around 6 μm that is directly referred to a remote frequency standard. The frequency standard reference light transferred from INRIM to LENS is locally regenerated and used to phase-lock an optical frequency comb. The 1064 nm laser is phase-locked to the comb while the 1300 nm laser is locked to it through the so-called virtual beat note (VB-PLL) scheme. These two lasers produce difference frequency generation inside an OP-GaP crystal. Finally the DFG radiation is used to phase-lock the emission of a QCL that drives the molecular transition.

The carrier-envelope offset frequency f_{ceo} of a commercial optical frequency comb (Menlo Systems GmbH, FC1500-100-WG) is stabilized at 20 MHz using a radio-frequency standard signal delivered by a local GPS-disciplined Rubidium-based local oscillator. The repetition rate frequency f_{rep} is phase-locked to the reference light at 1542.14 nm using an intra-cavity electro-optic modulator on a bandwidth of approximately 300 kHz. The locking frequency is properly chosen so that the comb repetition rate is exactly 100 MHz. The phase noise of the optical comb is then dominated by the residual noise of the stabilized 642 km fiber link [77].

The 1064 nm laser light, after been collimated, passes through an optical isolator to protect the laser from back-reflections. A first polarizing beam splitter is combined with a half-wave plate to allow for adjustment of the laser power without changing the laser amplifiers current, since this affects the laser output mode emission. The light is then split into three branches. Most of the power is used to pump the OP-GaP crystal, as explained in Chapter 1, while the remainder is sent to a wave meter and used to produce the beat note with the comb. The comb spectrum is split in two arms by means of a short-pass dicroic mirror with cutoff wavelength of 1180 nm (Thorlabs Inc., DMSP1180). The short-wavelength part is combined on a polarizing beam splitter with the 1064 nm radiation. The two overlapping beams are then reflected back towards a mirror by means of a diffraction grating (Thorlabs Inc., GR25-610) mounted in Littrow configuration to maximize the reflected power. The comb spectrum is diffracted and filtered out by an adjustable aperture that transmits the 1064 nm laser and a small part of the comb spectrum with wavelength around 1064 nm. Finally, the radiation is focalized on a 150 MHz bandwidth InGaAs photodiode (Thorlabs Inc., PDA10CF) where an interferometric filter around 1064 nm is placed to reduce undesired wavelengths. A very similar optical path is used to obtain the beat note between the diode laser emitting at around 1300 nm and the long-wavelength portion of the comb spectrum. For this beams all the optics are working around 1300 nm. A different diffraction grating (Thorlabs Inc., GR25-613) and interferometric filter are then used, while the detector is the same model. Both beat notes are detected with a minimum signal-to-noise ratio of 25 dB on a 100 kHz bandwidth. Their frequency has been indicated in the previous analysis as $f_{\text{p-c}}$ and $f_{\text{s-c}}$ for the pump and signal beams respectively.

In Fig. 2.6 the electronic setup used to process the beat notes signals is reported and reproduces the scheme shown in Fig. 2.4. All listed components are from Mini-Circuits. The beat note between the comb and the Nd:YAG laser, after been filtered and amplified, is used to frequency stabilize the 1064 nm laser via a phase-lock loop with bandwidth of about 500 Hz. The beat note frequency is then mixed with the comb carrier-envelop offset frequency f_{ceo}, filtered, amplified and sent as input to a 14-bit Direct Digital Synthesizer (DDS, Analog Devices, Inc., UG-207) that provides the term $\frac{N_{\text{s}}}{N_{\text{p}}}(f_{\text{p-c}} + f_{\text{ceo}})$ shown in Eq. 2.5. On the other side, the beat note between the laser diode and the comb is filtered and mixed with a local oscillator at frequency f_{LO}, also referenced to the GPS-Rb radio-frequency standard, to have the possibility of fine adjust the 1300 nm laser frequency. This signal is then filtered,

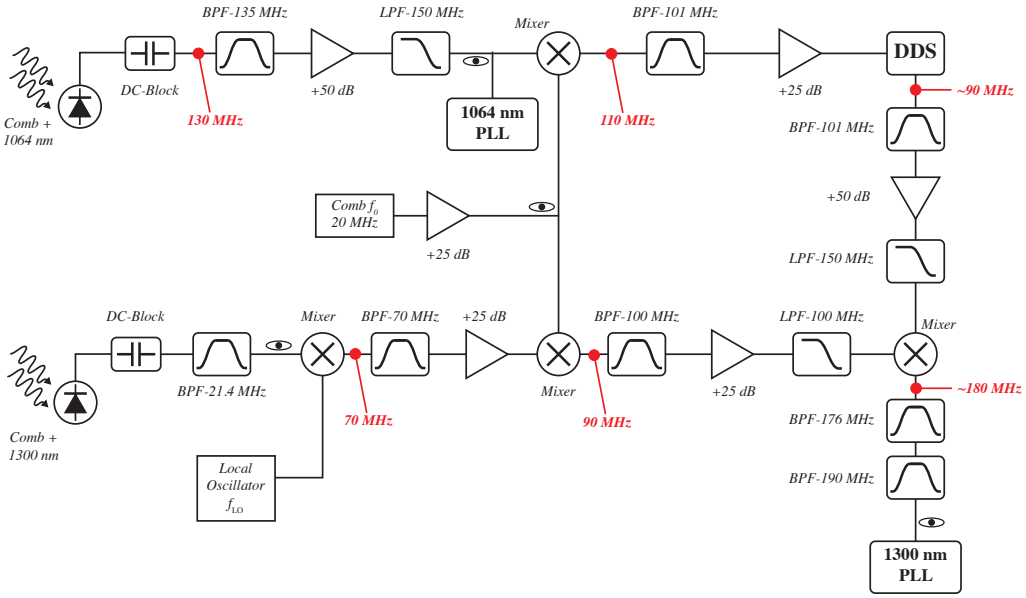

Figure 2.6: Electronic setup used to process the beat note signals and provide the correction signals for the 1064 nm and 1300 nm laser via phase-lock loops. The eye-like symbols indicate points where the signal is monitored. The red labels show the signal frequencies on the different lines.

amplified and mixed with the comb f_{ceo} to provide the term $\bar{f}_{\mathrm{s}}$ that is again filtered and amplified before being mixed with the filtered and amplified output of the DDS. The new sum-frequency signal is then again filtered and is used as the error signal for the phase-lock loop of the 1300 nm laser with a bandwidth exceeding 200 kHz. The presence of several monitors on the different signals allows a continuous monitor of locks to assure that phase coherence between different lasers is always maintained. The red labels on the figure show the signal frequencies on the different lines. For all the measurements presented in this thesis, the settings listed in Tab. 2.1 are used.

How the DFG of these two lasers is produced in the OP-GaP is described in the previous chapter. In order to increase the mid-IR generated power, a temperature stabilized quantum cascade laser (Alpes Lasers SA) is phase-locked to the DFG light and used for the spectroscopic measurement. The laser output is split in two beams: about 70% of the total power is collimated by means of a pair of positive lenses and sent towards the molecular beam. After the interaction with the molecules, the laser is back-reflected by means of a corner cube. A pinhole in the focus of the first lens filters away most of the back-reflected light, to which the QCL is very sensitive. The remaining power, about 30%, is combined in a non polarizing beam splitter with the radiation coming from the crystal: the beat note between the two radiation is detected by the Vigo detector with a bandwidth of about 10 MHz. Since the polarization of the DFG light is rotated by 90° with respect to the QCL, a half-wave

Table 2.1: Frequency and comb parameters used for the measurements presented in this thesis. The last row indicates the actual DDS output frequency due to its 14-bit resolution.

Parameter	Value
f_{rep}	100 MHz
f_{ceo}	20 MHz
N_{p}	2816364
N_{s}	2302371
$f_{\mathrm{p\text{-}c}}$	-130 MHz
$f_{\mathrm{s\text{-}c}}$	$\sim$ 20 MHz
f_{LO}	50 MHz
DDS ideal out	$-110 \cdot \frac{N_{\mathrm{s}}}{N_{\mathrm{p}}}$ MHz
DDS real out	-89.924743387 MHz

plate at 5.85 μm is placed in the QCL path to maximize the intensity of the beat note. Such a signal is used to feed a PLL that stabilizes the QCL by modulating its current with a bandwidth of 300 kHz. To change the emission frequency of the QCL and perform a frequency scan, the local oscillator of the PLL is tuned.

In Fig. 2.7 some typical recordings of the beat notes between different lasers are shown. The plot (a) shows the beat note between the comb and the regenerated reference light at 1542.14 nm. A PLL stabilizes the beat note frequency at 64 MHz to assure a repetition rate of 100 MHz. Panel (b) shows the beat note between the the comb tooth and the 1064 nm laser. In this case the beat note is stabilized at 130 MHz and it is broad because of the low locking bandwidth of about 500 Hz. On graph (c) and (d) the virtual beat note between the 1064 nm and the 1300 nm laser and the beat note between the QCL and the DFG light are shown. As usual, two shoulders appear on both sides of the frequency center. Their distance from the central peak correspond to the phase-lock loop bandwidth (around 300 kHz in (a) and (d) and 200 kHz in (c). In (b) such shoulders are not visible because the bandwidth is narrower than the mutual stability).

2.3 Characteristics of the 6 μm Radiation

In this section we derive the phase noise power spectral densities (PNPSD) of the different lasers used to generate the mid-IR radiation. We start from independent measurements of the PNPSD of the reference radiation at $\sim$1542.14 nm $S_{\phi,\mathrm{link}}(f)$, as described in [77, 81]. These measurements are available only at frequencies below 400 Hz. The repetition rate of the comb is stabilized on the beat note between the reference radiation and the tooth $N_{\mathrm{link}} = 1944001$. In the following we consider

(a) Comb vs Reference

(b) Comb vs Pump @ 1064 nm

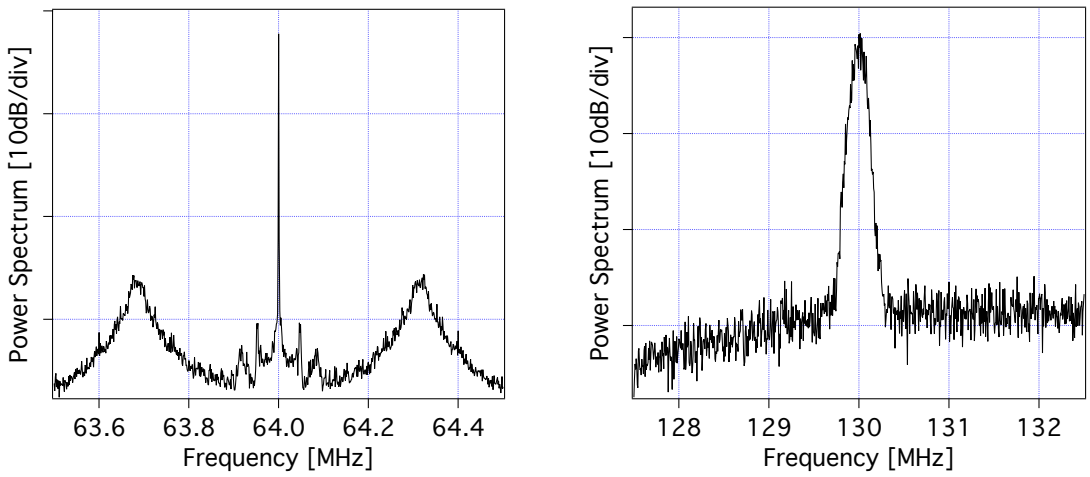

(c) Virtual beat note vs Signal @ 1300 nm

(d) QCL vs DFG

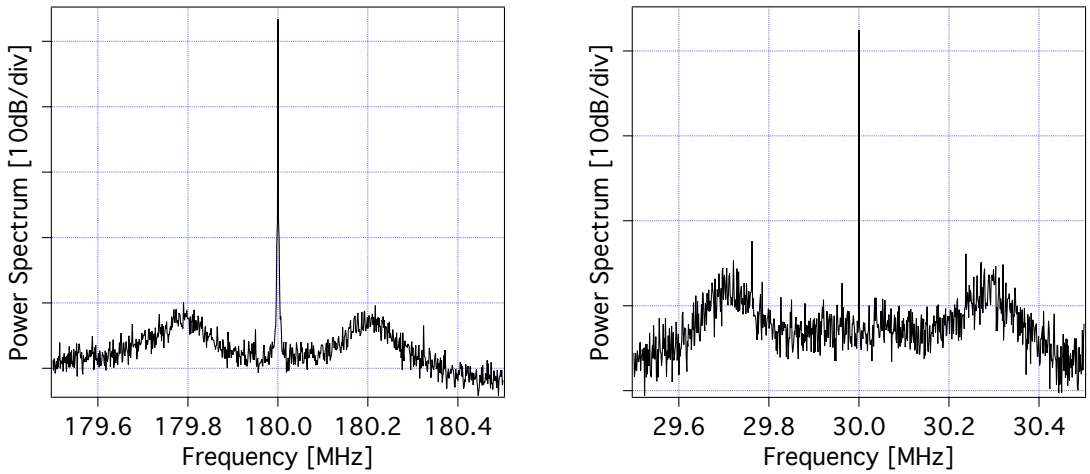

Figure 2.7: Beat notes of the different phase-lock loops acquired by means of a spectrum analyzer. (a): beat note between the comb and the reference laser at 1542 nm. Beat note between comb and pump (b) and between virtual beat note and signal (c). (d): beat note between the generated DFG and the QCL. All spectra are acquired with 10 Hz resolution bandwidth, except the data shown in (b) for which the resolution bandwidth is 300 Hz.

the case of ideal locks[4] and we neglect the noise due to the term f_{ceo}. Under this

[4]For ideal lock we intend a phase-lock loop that perfectly stabilize the beat note between the two lasers to a zero-noise radio-frequency reference.

assumptions the PNPSD on the comb repetition rate depends on the $S_{\phi,\mathrm{link}}(f)$ as

$$S_{\phi,\mathrm{rep}}(f) = \frac{S_{\phi,\mathrm{link}}(f)}{N_{\mathrm{link}}^2} = \frac{S_{\phi,\mathrm{link}}(f)}{1944001^2} \tag{2.11}$$

Once we have obtained the PNPSD of the comb repetition rate, we can easily calculate the propagation of such noise over the other teeth. The transfer of the repetition rate noise on the comb tooth that will beat with the pump laser can be obtained as

$$S_{\phi,\mathrm{N_p}}(f) = S_{\phi,\mathrm{rep}}(f)N_{\mathrm{p}}^2 = \left(\frac{N_{\mathrm{p}}}{1944001}\right)^2 S_{\phi,\mathrm{link}}(f) \tag{2.12}$$

and a similar calculation can be done for the tooth that will beat with the signal. In Fig. 2.8 the resulting spectra are shown. As we can see from the graph, the PNPSD for the two teeth are similar, with a slightly lower noise for the signal, due to the propagation of the repetition rate noise. The small bump at frequency around 40 Hz corresponds to the phase-lock loop bandwidth of the link.

We can use these estimated noises to extract informations about the free-running line width of the pump and signal lasers. The PNPSD of the laser beating with a comb tooth can be calculated from the PLL output going to the laser driver[5]. The results of this procedure is shown in Fig. 2.8 in black and grey for pump and signal, respectively. If we compare the blue and the black curve, i.e. comb tooth and the PLL output for the pump laser, we can see that the latter is much higher than the tooth noise for frequencies lower than 40 Hz. This noise is mainly due to the pump laser because the comb tooth is much more stable in this range. At higher frequencies, instead, the two noises are the same meaning that the PLL is copying the noise of the comb tooth onto the pump beam. The optimal locking bandwidth for this laser would be therefore about 40 Hz, but for technical limitation we have used a bandwidth of about 500 Hz that is still good because we expect that the pump laser noise in the region between 40–500 Hz is similar to the one of the comb tooth.

The grey curve is the PNPSD of the PLL output going to the driver of the signal laser. A comparison with the noise on the closest comb tooth suggests that the noise is only due to the signal laser and therefore a tight lock can be employed.

Using the Eq. 2.10, we derive the expected difference frequency generation PNPSD of the idler as

$$S_{\phi,\mathrm{DFG}}(f) = S_{\phi,\mathrm{N_p}}(f)\left(1 - \frac{N_{\mathrm{s}}}{N_{\mathrm{p}}}\right)^2 = \left(\frac{N_{\mathrm{p}} - N_{\mathrm{s}}}{1944001}\right)^2 S_{\phi,\mathrm{link}}(f) \tag{2.13}$$

This is shown in red on Fig. 2.8. Since the term $(1 - N_{\mathrm{s}}/N_{\mathrm{p}})$ is smaller than one, the noise transferred to the idler radiation is smaller than the one on the pump

[5]The PNPSD obtained from the PLL output signal going to the laser driver include both the contribution of the laser and the comb tooth. For this reason such data can only be used to estimate the dominant noise contribution at the different frequencies.

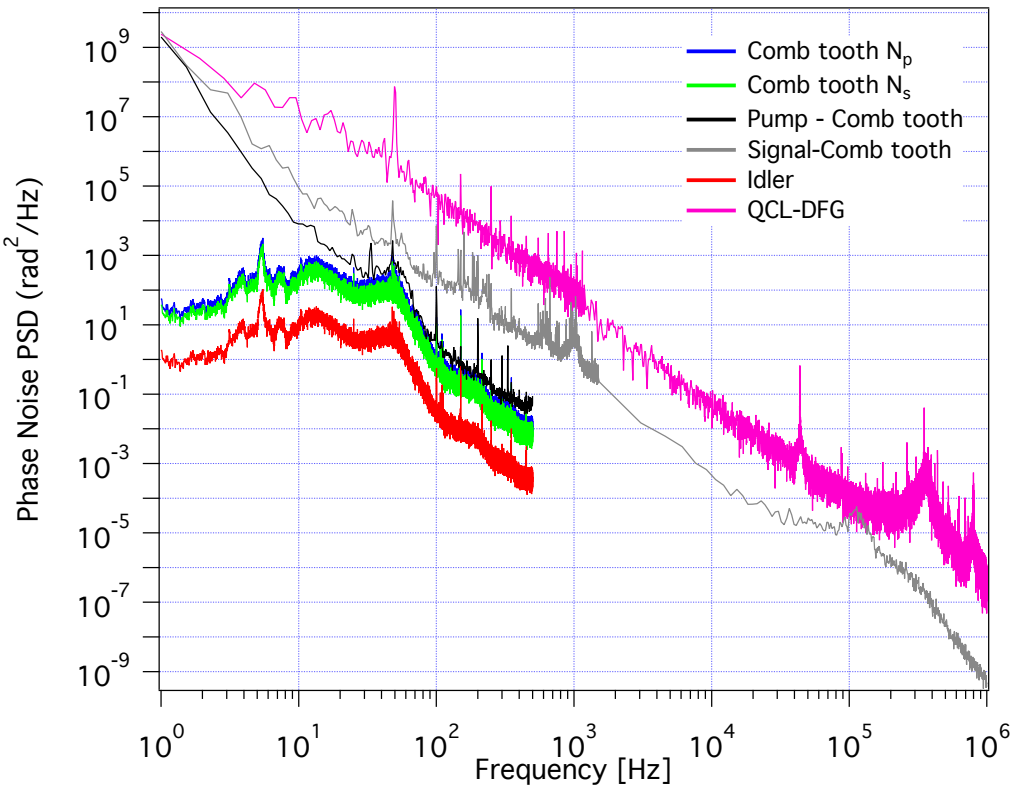

Figure 2.8: Calculated and measured phase noise power spectral densities. The phase noise of the comb tooth N_p and N_s, as well as at the idler frequency, are calculated from independent measurement of the PNPSD of the reference radiation at 1542.14 nm. The other dataset are obtained deriving the PNPSD from the PLL output signal that goes to the different laser drivers.

laser. Deriving the noise spectrum from the PLL output going to the QCL driver for locking it to the DFG radiation, we obtain the pink curve on the plot. This curve is always higher than the red curve in the common frequency range, thus the noise must be due to the free-running QCL. We therefore expect that the PLL will lower this curve to the level of the red one, thus transferring the stability of the idler frequency to the QCL. Unfortunately we cannot measure directly the mid-IR PNPSD to date. The main limitation are the intrinsic noise of the mid-IR detectors and the availability of a strong molecular transition close to the laser emission frequency. The estimation presented here is our best guess for the PNPSD of the ~ 6 μm source that we have developed.

In the former analysis we have assumed that the phase-lock loops are driven by a zero-noise frequency reference. In reality, all the PLL and local oscillators used in the locking chain are referenced to the local GPS-disciplined Rubidium-based

Table 2.2: Relative uncertainties due to the different contributions in the locking chain to reference the QCL to the primary frequency standard delivered by INRIM in Turin.

Contribution	Relative Uncertainty
Regeneration	$\sim 5 \cdot 10^{-19}$
PLL 1064 nm	$\sim 5 \cdot 10^{-19}$
PLL 1300 nm	$\sim 4 \cdot 10^{-18}$
PLL 5832 nm	$\sim 4 \cdot 10^{-19}$
LO (f_{LO})	$\sim 1 \cdot 10^{-18}$

reference that has a relative stability of $\delta\nu_{10\ \mathrm{MHz}} \simeq 1 \cdot 10^{-12}$, as reported in Fig. 2.3. As we are going to demonstrate, the final stability of the mid-IR laser source is only determined by the stability of the optical reference, since all the other contributions are several orders of magnitude lower.

Let us consider, for example, the PLL that stabilized the frequency of the pump laser at 130 MHz from the comb tooth N_{p}. The beat note between these two lasers is compared to the 10 MHz reference from the GPS-disciplined Rubidium-based reference multiplied by 13. The relative uncertainty introduced by this PLL is then

$$\frac{\delta\nu_{10\ \mathrm{MHz}} * 10\ \mathrm{MHz} * 13}{\nu_{\mathrm{p}}} \simeq 5 \cdot 10^{-19} \tag{2.14}$$

Doing the same calculation for all the other PLL and local oscillators involved in the locking chain, we get the results listed in Tab. 2.2. The comb repetition rate frequency f_{rep}, as well as its offset frequency f_{ceo}, are not reported in such a table because they do not contribute to the uncertainty of the idler radiation.

Using the parameters listed in Tab. 2.1, taking into account the limited resolution of the DDS, and using the Eq. 2.9 the mid-IR radiation results to be at the frequency of

$$\nu_{\mathrm{i}} = 51399149924743.4\ \mathrm{Hz} \tag{2.15}$$

with a relative instability only dominated by the link and reported in Fig. 2.3.

Chapter 3

CO Molecules

Carbon monoxide (CO) is an odorless and transparent gas that becomes liquid at 81.7 K under standard pressure conditions. It is naturally present in the atmosphere and it is a toxic product of combustion processes. Thus, modern combustion engines use expensive catalytic converters to oxidate CO to CO_2. Its relatively simple modeling makes it one of the most studied diatomic molecules.

CO has been proposed as a convenient system molecule to search for temporal and spatial variation of fundamental constants [84]. Being a simple molecule formed by relatively light atoms, carbon monoxide has been found in high abundance in interstellar clouds. By comparing the spectra of CO at large red-shift regions in the universe with present-days measurements, it is possible to constrain some variations of fundamental constants [85]. Alternatively, a repeated laboratory measurement can yield similar information, provided that the higher precision of the measurements compensates for the shorter time scales involved in the comparison [86].

It has been demonstrated that molecular beams of metastable CO can be manipulated and decelerated to a standstill using electric fields [87]. The relatively long lifetime of metastable CO makes it a suitable system for high precision measurements. The corresponding reduction of the transition time broadening in spectroscopic experiments is an intriguing perspective for high resolution measurements. In our group, we use Stark decelerators to slow down and also to trap CO molecules. Therefore, the experiments presented in this thesis are a step in the field of molecular manipulation for high precision experiments.

The six electrons of carbon and the eight electrons of oxygen in the ground state occupy the lowest molecular orbital resulting from the $1s$, $2s$ and $2p$ electronic states. The ground state is a $X^1\Sigma^+$ resulting in a closed-shell electronic configuration given by

$$X^1\Sigma^+ : (1s\sigma)^2(1s\sigma^*)^2(2s\sigma)^2(2s\sigma^*)^2(2p\pi)^4(2p\sigma)^2 \tag{3.1}$$

Ground state CO has a small permanent electric dipole moment of 0.112 Debye [88], oriented so that the oxygen is charged positively despite its larger electronegativity.

The first electronically excited state of CO is $a^3\Pi$. It has an orbital configuration given by

$$a^3\Pi : (1s\sigma)^2(1s\sigma^*)^2(2s\sigma)^2(2s\sigma^*)^2(2p\pi)^4(2p\sigma)^1(2p\pi^*)^1 \tag{3.2}$$

where the electron density around the carbon of the orbital $2p\pi^*$ is significantly lower then the orbital $2p\sigma$, from which the electron is excited [89]. For this reason this excited state has an order of magnitude larger electric dipole moment, experimentally measured to be 1.37 Debye [90], which points from the oxygen to the carbon atom. This large dipole moment makes this state suitable for manipulation with electric fields. The $a^3\Pi$ state is metastable with a relatively long lifetime of 2.63 ms [91]. This time is sufficiently long to use this state in molecular beam experiments where usual time from the first interaction to the detection is of the order of several hundreds of microseconds. Another advantage of metastable CO is that it carries around 6.0 eV of internal energy. This facilitates detection: when a molecule hits a clean gold surface, this internal energy is converted into a free Auger electron that can be efficiently detected, for example with a micro-channel plate detector. Finally, CO can be easily obtained in bottles, and the production of molecular beams is then straightforward. In this chapter, the Hamiltonian of the carbon monoxide is briefly reviewed with special attention to the vibrational and rotational part. The discussion is based on references [92–96], which are suggested for a more detailed analysis.

3.1 Hund's Case (a)

There are various ways in which the angular momenta can coupled to each other in diatomic molecules, giving rise to the various Hund's coupling cases [97]. The Hund's cases are usually indicated with letters from (a) to (e) that correspond to idealized cases where some terms, appearing in the molecular Hamiltonian and involving couplings between angular momenta, are assumed to dominate over all the other terms. The following angular momenta, neglecting the hyperfine structure, are involved in the description of Hund's cases:
$\hat{L}$: electronic orbital angular momentum
$\hat{S}$: electronic spin angular momentum
$\hat{J}$: total angular momentum
$\hat{N}$: total angular momentum excluding electron spin, so that $\hat{N} = \hat{J} - \hat{S}$
$\hat{R}$: rotational angular momentum of nuclei $\hat{R} = \hat{N} - \hat{L}$

The first of these cases, referred to as Hund's case (a), is illustrated in the vector diagrams shown in Fig. 3.1. It provides a good picture of the case of excited carbon monoxide molecule in the $a^3\Pi$ state, for small J values. This case describes the situation in which the coupling between electronic spin and electronic angular momentum is large compared to the interaction between nuclear rotation and elec-

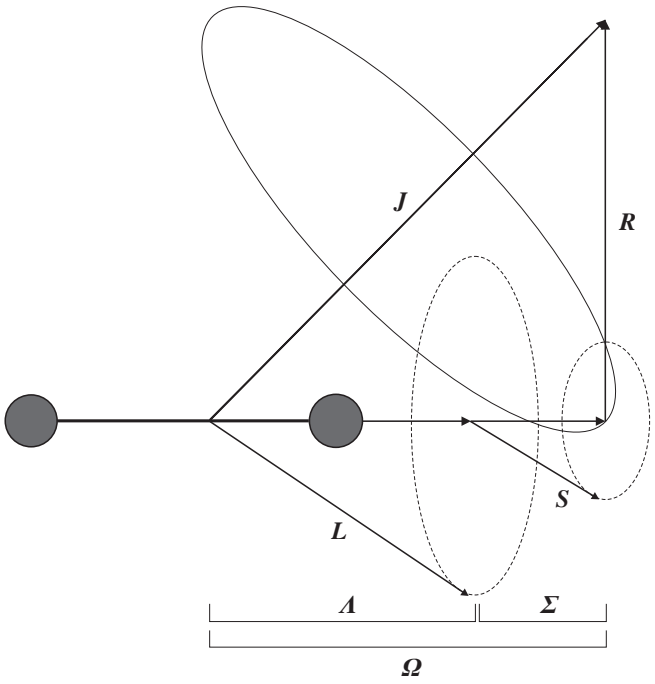

Figure 3.1: Angular momenta coupling in Hund's case (a). See text for details.

tronic motion, and both these interactions are much smaller than the electrostatic coupling of the electronic orbital angular momentum of the unpaired electrons to the internuclear axes. The projection $\hat{L}_z$ of the orbital angular momentum $\hat{L}$ on the the internuclear axis is well defined and yields the quantum number Λ. Furthermore the spin-orbit coupling is strong enough to couple the total electronic spin $\hat{S}$ to $\hat{L}$ so that also the projection of $\hat{S}$ over the internuclear axis, $\hat{S}_z$, is well defined and labeled with quantum number Σ.

These two projection quantum numbers give rise to a total electronic angular momentum projection $\Omega = \Lambda + \Sigma$ and the coupling between $\hat{\Omega}$ and $\hat{R}$ forms a total angular momentum given by $\hat{J} = \hat{\Omega} + \hat{R}$. The precession of $\hat{L}$ and $\hat{S}$ about the internuclear axes is assumed to be much faster than the nutation of $\hat{\Omega}$ and $\hat{R}$ about $\hat{J}$. Since $\hat{J}$ obeys to the common commutation relations of the angular momentum operators, it is possible to quantize its projection along a space-fixed axis, $\hat{J}_Z$, yielding the quantum number M. We can therefore define the following

eigenvalues corresponding to the operators:

$$\begin{aligned}
\hat{J}^2|JS\Omega\Lambda\Sigma M\rangle &= J(J+1)|JS\Omega\Lambda\Sigma M\rangle \\
\hat{S}^2|JS\Omega\Lambda\Sigma M\rangle &= S(S+1)|JS\Omega\Lambda\Sigma M\rangle \\
\hat{J}_z|JS\Omega\Lambda\Sigma M\rangle &= \Omega|JS\Omega\Lambda\Sigma M\rangle \\
\hat{L}_z|JS\Omega\Lambda\Sigma M\rangle &= \Lambda|JS\Omega\Lambda\Sigma M\rangle \\
\hat{S}_z|JS\Omega\Lambda\Sigma M\rangle &= \Sigma|JS\Omega\Lambda\Sigma M\rangle \\
\hat{J}_Z|JS\Omega\Lambda\Sigma M\rangle &= M|JS\Omega\Lambda\Sigma M\rangle
\end{aligned} \tag{3.3}$$

A problem of the chosen basis function is that the parity is not defined. In other words, such a basis is not an eigenfunction of the inversion operator that reverses the sign of all coordinates in the space-fixed coordinate system. Since the inversion operator commutes with any purely electromagnetic Hamiltonian, a definite parity function can be defined by symmetrizing the wave function

$$|JS\Omega\Lambda\Sigma M\pm\rangle = \frac{1}{\sqrt{2}}\big(|JS|\Omega||\Lambda||\Sigma|M\rangle \pm (-1)^{J-S}|JS-|\Omega|-|\Lambda|-|\Sigma|M\rangle\big) \tag{3.4}$$

Now, in this new base with definite parity, the quantum number Λ is assumed to be positive while Σ can still vary from $-S$ to S and Ω can consequently vary from $\Lambda - S$ to $\Lambda + S$. If $S \leq \Lambda$, Ω will always be positive and $J = \Omega, \Omega+1, \Omega+2, ...$ Unless an external electric field is applied or electronic states are perturbed, states with different parity are degenerate. The $\Lambda = 1$ states (Π states) can mix with $\Lambda = 0$ states (Σ states) that can remove the degeneracy. This effect can split the levels of different parity leading to the so called Λ-*doubling splitting*. In this case each J level splits in two states with opposite parity named by symbols + and −.

Since in the following text the spherical tensorial notation is used, we introduce the basic concepts of these operators to facilitate the reading. If we consider a generic vector $\boldsymbol{A}$ defined in a cartesian plane as $\boldsymbol{A} = A_x\boldsymbol{i} + A_y\boldsymbol{j} + A_z\boldsymbol{k}$ where $\boldsymbol{i}$, $\boldsymbol{j}$ and $\boldsymbol{k}$ are the cartesian unitary vector, the spherical tensor of rank 1 acting on it satisfies the following relations

$$\begin{aligned}
T^1_0(\boldsymbol{A}) &= A_z\boldsymbol{k} \\
T^1_{\pm1}(\boldsymbol{A}) &= \mp\frac{1}{\sqrt{2}}(A_x\boldsymbol{i} \pm iA_y\boldsymbol{j}) = \mp\frac{1}{\sqrt{2}}\boldsymbol{A}_\pm
\end{aligned} \tag{3.5}$$

where the term $\boldsymbol{A}_\pm$ appears more familiar if we consider the generic vector $\boldsymbol{A}$ as an angular momentum operator like $\hat{L}$, $\hat{S}$ or $\hat{J}$ in which, for example, the operators $\hat{J}_+$ and $\hat{J}_-$ are the ladder operators that satisfy the following commutation relations

$$\begin{aligned}
[\hat{J}_z, \hat{J}_\pm] &= \pm\hat{J}_\pm \\
[\hat{J}_+, \hat{J}_-] &= 2\hat{J}_z
\end{aligned} \tag{3.6}$$

In the following text it is also useful to write a scalar product between two generic vectors or operators $\hat{A}$ and $\hat{B}$ in terms of spherical tensors, where the following rule is valid

$$\hat{A} \cdot \hat{B} = \sum_q (-1)^q T^1_{-q}(\hat{A}) T^1_q(\hat{B}) \tag{3.7}$$

In this equation the q index ranges from $q = -1, 0, +1$ because the spherical tensor has rank 1.

3.2 Effective Hamiltonian for CO

The general Hamiltonian $\hat{H}$ for a molecule is a very complex operator because it includes many terms to describe the energetic levels precisely. Usually, it includes the kinetic energies of the electrons and nuclei and their respective attraction and repulsion, but also coupling between spins, spin-orbit and so on. Since all these terms of the complete Hamiltonian contribute with different weights to the final energy, the Hamiltonian can be simplified by making some assumptions. The most important is the Born-Oppenheimer approximation in which the coupling between the electronic and the nuclear motion is neglected. This assumption is based on the fact that the nuclear mass is much larger than the electron mass. Consequently, the electron cloud can adapt immediately to the nuclear motion. This allows to separate the electronic motion from the vibrational one, in each electronic state. A hierarchic structure can thus be defined, in which different terms in the complete Hamiltonian dominate over others, that can be treated as perturbations. In a diatomic molecule the energy splitting between different electronic states is typically of the order of 20000 cm^{-1}. Each of these states supports a set of closer energy levels due to the vibration of the molecular nuclei with a typical spacing of about 1000 cm^{-1}, that in turn shows a much closer set of rotational levels spaced by about 1 cm^{-1}.

This hierarchic structure is the starting point of the Effective Hamiltonian approach, which is a method to describe the leading contributions to the dynamics, by treating the weaker interaction terms perturbatively. The effective Hamiltonian can thus provide the same energy levels of the complete initial Hamiltonian, within the desired level of accuracy. For instance, electronic, vibrational and rotational levels are treated and solved separately, while their mutual weaker interactions, considered as perturbations, lead to energy correction and level splitting phenomena.

An approach to calculate the effective Hamiltonian is the use of a succession of contact or Van Vleck transformations [92]. The basic idea is to apply a unitary transformation T on the initial Hamiltonian to decouple as much as possible various subsets of the different degrees of freedom. This procedure allows to effectively decouple the electronic and vibrational states from all the remaining terms, such as rotations and spin-dependent terms.

Let us consider an Hamiltonian $\hat{H}$ as the sum of its diagonal part $\hat{H}^{(0)}$ with the

off-diagonal part $\lambda\hat{H}'$ as

$$\hat{H} = \hat{H}^{(0)} + \lambda\hat{H}' \tag{3.8}$$

where λ is the perturbation parameter. We introduce the unitary transformation T that can be cast in the form

$$T = e^{i\lambda S_1} e^{i\lambda^2 S_2} ... \tag{3.9}$$

where S_1, S_2, etc. are Hermitian operators that are chosen so that they remove the off-diagonal contributions of the order λ, λ^2, etc., respectively. The new Hamiltonian $\tilde{H}$, obtained by applying the following transformation

$$\tilde{H} = T^{-1}\hat{H}T \tag{3.10}$$

can be perturbatively decomposed into the following terms

$$\tilde{H} = \tilde{H}^{(0)} + \lambda\tilde{H}^{(1)} + \lambda^2\tilde{H}^{(2)} + ... \tag{3.11}$$

that have to be compared, order-by-order, with the right-hand terms of Eq. 3.10. By doing this, it is possible to correct the eigenvalues of the Hamiltonian $\tilde{H}^{(0)}$, that are the same of the diagonal matrix $\hat{H}^{(0)}$, with the off-diagonal contribution of $\hat{H}'$ at the desired order. We can therefore obtain an effective diagonal matrix with eigenvalues that approximate the eigenvalues of the initial non diagonal matrix to the desired accuracy.

In the following it is shown how to use this approach to solve the complex Hamiltonian of a diatomic molecule.

The complete Hamiltonian for a diatomic molecule, like carbon monoxide, can be written as a sum of different terms accounting for the different interactions. Let us first consider the case without any external field. The additional effect of external fields, in particular magnetic field, is included later in this chapter. This Hamiltonian can be written (in a molecule-fixed reference system) as

$$\hat{H} = \hat{H}_{\text{elec}} + \frac{\hat{P}_r^2}{2\mu} + B(r)hc(\hat{N} - \hat{L})^2 + \hat{H}_{\text{SO}}^{(e)} + \hat{H}_{\text{SO}}^{(n)} + \hat{H}_{\text{SS}}^{(e)} + \hat{H}_{\text{SS}}^{(t)} \tag{3.12}$$

where the first term corresponds to the sum of the kinetic electron energy and the coulomb potential between all the charged particles, while the second term accounts for the vibrational kinetic energy, in which μ is the reduced mass of the nuclei M_1 and M_2, i.e. $\mu = M_1M_2/(M_1 + M_2)$. The next term is the rotational kinetic energy, where the function $B(r)$ is the rotational coefficient, equal to $\hbar/(4\pi c\mu r^2)$, being r the distance between the two nuclei. The last four terms are respectively the spin-orbit and the spin-other-orbit operator, which contains the electronic and nuclear momenta and, finally, the scalar and tensor part of the spin-spin electron interaction. The explicit form of all the terms can be found in [96].

The procedure to obtain the effective Hamiltonian usually proceeds in two steps. First we decouple all the different electronic states by deriving an intermediate effective Hamiltonian acting only on all the vibrational states inside a single electronic

state. Thus, the operators remain functions of the vibrational coordinate r. In the second step, the terms in this Hamiltonian which couple the different vibrational states are removed, resulting in an operator that acts only inside the single vibrational state on one electronic level.

In the following n addresses a single electronic state. The first step consists on the application of the electronic contact transformation. This modifies the initial Hamiltonian $\hat{H}$ in a new Hamiltonian $\hat{H}_n$, on which the off-diagonal matrix elements on the basis n are removed at the desired order, without altering the eigenvalues of the initial Hamiltonian. For a molecule in which the spin-orbit coupling is smaller than the electronic interval, the Hund case (a) basis can be used as an electronic state vector with

$$\hat{H}_{\text{elec}}|n, S, \Lambda, \Sigma, r\rangle = V_n(r)|n, S, \Lambda, \Sigma, r\rangle \tag{3.13}$$

where $V_n(r)$ indicates the eigenvalue of the electronic Hamiltonian as a function of the internuclear distance r. The Hamiltonian $\hat{H}_{\text{elec}}$ can be considered, for the previous considerations, the zero-th order Hamiltonian, while all the others terms are the perturbation $\hat{H}'$. The $V_n(r)$ and $|n, S, \Lambda, \Sigma, r\rangle$ are thus the zero-th order eigenvalues and eigenstates. The perturbation process allows to write $\hat{H}'$ on the basis of $|n, S, \Lambda, \Sigma, r\rangle$ in such a way that the off-diagonal matrix elements in n are much smaller than the terms $V_n(r)$ accordingly to the perturbation order. The new Hamiltonian can thus be written as

$$\begin{aligned}
\hat{H}_n =& V_n(r) + V_n^{ad}(r) + V_n^{sp}(r) + \frac{\hat{P}_r^2}{2\mu} + \\
&+ B_n(r) hc \hat{N}^2 + A_n(r) hc \hat{L}_z \hat{S}_z + \\
&+ \gamma_n(r) hc \hat{N} \cdot \hat{S} + \frac{2}{3} hc \lambda_n(r)(3\hat{S}_z^2 - \hat{S}^2) + \\
&+ (o_n + p_n + q_n) \sum_{q=\pm 1} e^{-2qi\psi} T_q^1(\hat{S}) T_q^1(\hat{S}) \\
&- (p_n + 2q_n) \sum_{q=\pm 1} e^{-2qi\psi} T_q^1(\hat{J}) T_q^1(\hat{S}) \\
&+ q_n \sum_{q=\pm 1} e^{-2qi\psi} T_q^1(\hat{J}) T_q^1(\hat{J})
\end{aligned} \tag{3.14}$$

The last three terms represent the Λ-doubling contributions that, at this level of approximation, are non zero only for a Π electronic state. The new terms $V_n^{ad}(r)$ and $V_n^{sp}(r)$ can also be included in the $V_n(r)$, the zero-th order contribution to the electronic energy. The $V_n^{ad}(r)$ operator indicates the adiabatic contribution that describes the first-order effect of the nuclear kinetic energy within the electronic state. At first-order, its effect is much smaller than $V_n(r)$, but has to be considered, when the isotopic dependence of the electronic state is investigated. The term $V_n^{sp}(r)$ takes into account the spin-spin coupling at first-order and the spin-orbit-coupling at second-order to the electronic energy. The Hamiltonian $\hat{H}_n$ does not contain

any term coupling different electronic states, but, as mentioned before, a second transformation has to be performed in order to decouple the different vibrational states inside the single electronic state n.
In this case the new zero-th order Hamiltonian describing the vibrational motion results in the following equation

$$\left(V_n(r) + \frac{\hat{P}_r^2}{2\mu}\right)|n,v\rangle = hc(E_{ne} + G_{nv}^{(0)})|n,v\rangle \tag{3.15}$$

where we have introduced the vibrational quantum number v. In order to calculate the eigenvalues of this Hamiltonian, we can express the potential $V_n(r)$ as a power series of displacement $x = r - r_e$ of the internuclear distance r from its equilibrium position r_e. Assuming that the position $r = r_e$ corresponds to the minimum of the potential at which $V_n(r_e) = E_{ne}$, we can write the potential $V_n(r)$ as

$$\begin{aligned} V_n(r) =& V_n(r_e) + \left(\frac{\partial V_n(r)}{\partial r}\right)_{r_e} x + \frac{1}{2}\left(\frac{\partial^2 V_n(r)}{\partial r^2}\right)_{r_e} x^2 + ... \\ =& E_{ne} + \frac{1}{2}a_1 x^2 + \frac{1}{6}a_2 x^3 + \frac{1}{24}a_3 x^4 + ... \end{aligned} \tag{3.16}$$

where a_i are the expansion coefficients. It immediately follows that the second order term of this expansion gives rise to the harmonic oscillator Hamiltonian, for which the eigenvalues are known to be proportional to $(v+1/2)$. The higher order terms are the anharmonic terms, which can be solved for the harmonic oscillator Hamiltonian resulting in the following eigenvalues

$$G_{nv}^{(0)} = \omega_e\left(v + \frac{1}{2}\right) - \omega_e x_e\left(v + \frac{1}{2}\right)^2 + \omega_e y_e\left(v + \frac{1}{2}\right)^3 + ... \tag{3.17}$$

where the coefficients ω_e, $\omega_e x_e$ and $\omega_e y_e$ are spectroscopic coefficients commonly used in literature for the description of the vibrational eigenvalues. Notice that the superscript (0) in the vibrational eigenvalues remembers that only the zero-th vibrational potential energy function $V_n(r)$ has been used, while the higher order terms as $V_n^{ad}(r)$ and $V_n^{sp}(r)$ have been neglected. This assumption is justified in the case of a light molecule, as CO, and allows us to write an isotopically independent expression for the vibrational eigenvalues.

Using the operator in Eq. 3.15 as zero-th order Hamiltonian, all the remaining terms of Eq. 3.14 are treated as perturbations. As before, a second contact transformation is performed by considering only the first-order terms and the more significant second-order terms to derive the new effective Hamiltonian $\hat{H}_{nv}$, which acts only inside each vibronic state. The validity condition for this new operators, as usual, is that the perturbation matrix elements introduce contributions much smaller than the vibrational spacing. The first order terms can be simply considered as a modification of the various functions $X(r)$ appearing in Eq. 3.14, i.e. the

functions $B_n(r)$, $A_n(r)$, etc.. The modification consists in the expansion of the different functions as a power series of $(v + 1/2)$, due to the anharmonic oscillator corrections, as

$$X(r) = X_{ne} + b_1\left(v + \frac{1}{2}\right) + b_2\left(v + \frac{1}{2}\right)^2 + ... \tag{3.18}$$

where X_{ne} and b_i indicate the value of the function at $r = r_e$ and the expansion coefficients respectively. Since these terms introduce only minor corrections, the larger contribution is expected to come from terms that are strongly dependent on r, as the rotations. Therefore, it is common in literature to find only the function $B_n(r)$ expanded in power series as

$$B_{nv} = B_e - \alpha_e\left(v + \frac{1}{2}\right) + \gamma_e\left(v + \frac{1}{2}\right)^2 + \tag{3.19}$$

where $B_e = \hbar/(4\pi cI)$, being $I = \mu r_e^2$ the moment of inertia of the molecule, while α_e and γ_e are the other common spectroscopic coefficients used for the power expansion. The resulting $\hat{H}_{nv}$ effective Hamiltonian, for the rotation-spin structure of the vibronic state nv, can thus be written as

$$\frac{\hat{H}_{nv}}{hc} = E_{ne} + G_{nv} + \hat{H}_{\text{rot}} + \hat{H}_{\text{CD}} + \hat{H}_{\text{SO}} + \hat{H}_{\text{SS}} + \hat{H}_{\text{SR}} + \hat{H}_{\text{LD}} \tag{3.20}$$

in which the first two terms are the electronic state energy and the vibrational energy, while all the others are the following

Rotational kinetic energy

$$\hat{H}_{\text{rot}} = B_{nv}\hat{N}^2 \tag{3.21}$$

Centrifugal distortion

$$\hat{H}_{\text{CD}} = -D_{nv}\hat{N}^4 \tag{3.22}$$

This term results from the mixing of the vibrational levels due to the term $B_n(r)$. Also the coefficient D_{nv} is expanded in power series as

$$D_{nv} = D_e + \beta_e\left(v + \frac{1}{2}\right) + ... \tag{3.23}$$

where D_e and β_e are common reported spectroscopic constants.

Spin-orbit coupling

$$\hat{H}_{\text{SO}} = A_{nv}\hat{L}_z\hat{S}_z + \frac{A_{nDv}}{2}\{\hat{N}^2, \hat{L}_z\hat{S}_z\} \tag{3.24}$$

Here the second term is due to the centrifugal distortion of the spin-orbit due to the fact that the electronic motion is slightly influenced by the position of the nuclei. The curly bracket indicates the anti-commutator.

Spin-spin coupling

$$\hat{H}_{\mathrm{SS}} = \frac{2}{3}\lambda_{nv}(3\hat{S}_z^2 - \hat{S}^2) + \frac{\lambda_{nDv}}{2}\{\hat{N}^2, 3\hat{S}_z^2 - \hat{S}^2\} \tag{3.25}$$

Also this expression includes the second-order centrifugal distortion term modifying the spin-spin coupling

Spin-rotation coupling

$$\hat{H}_{\mathrm{SR}} = \gamma_{nv}\hat{N}\cdot\hat{S} + \frac{\gamma_{nDv}}{2}\{\hat{N}^2, \hat{N}\cdot\hat{S}\} \tag{3.26}$$

Again we have included the presence of a second-order contribution coming from the centrifugal distortion term

Λ-doubling term

$$\begin{aligned}
&\hat{H}_{\mathrm{LD}} = \\
&\frac{1}{2}\sum_{q=\pm1}\{(o_{nv}+p_{nv}+q_{nv}) + (o_{nDv}+p_{nDv}+q_{nDv})\hat{N}^2, e^{-2qi\psi}T_q^1(\hat{S})T_q^1(\hat{S})\}+ \\
&-\frac{1}{2}\sum_{q=\pm1}\{(p_{nv}+2q_{nv}) + (p_{nDv}+2q_{nDv})\hat{N}^2, e^{-2qi\psi}T_q^1(\hat{J})T_q^1(\hat{S})\}+ \\
&+\frac{1}{2}\sum_{q=\pm1}\{q_{nv}+q_{nDv}\hat{N}^2, e^{-2qi\psi}T_q^1(\hat{J})T_q^1(\hat{J})\}
\end{aligned} \tag{3.27}$$

This term produces a second-order effect that mixes different electronic states. Precisely, due to this term, each level labeled by a defined rotational, vibrational and electronic quantum number, splits in two states with opposite parity. This phenomena arises from the coupling between rovibrational states, lying within different electronic eigenstates, due to the rotational and spin-orbit Hamiltonians. Indeed, when these last terms are neglected, namely in the absence of rotations, the parity is a symmetry and therefore energy eigenstates, containing both states of opposite parity, are doubly degenerate. Now, $\hat{H}_{\mathrm{LD}}$ is the term responsible for the breaking of parity symmetry, thus leading to Λ-doubling splitting. In $\hat{H}_{\mathrm{LD}}$ there are three parameters, which can be fixed experimentally, and an exponential factor $e^{\pm 2i\psi}$, which multiplies each operator product and then ensures explicitly that $\hat{H}_{\mathrm{LD}}$ has non-zero matrix elements only between states with $\Lambda = 1$ and $\Lambda = -1$. In fact, by assuming an effective form of the Λ component of the wave function $|\Lambda\rangle = \frac{1}{\sqrt{2\pi}}e^{i\Lambda\psi}$, where the phase ψ is the electron orbital azimuthal angle, the matrix element $\langle\Lambda_1|e^{\pm 2i\psi}|\Lambda_2\rangle$, obtained by integrating over ψ, will be vanishing unless $\Lambda_1 = \pm 1$ and $\Lambda_2 = \mp 1$. Therefore, $\hat{H}_{\mathrm{LD}}$ can only connect states with $\Lambda = 1$ to states with $\Lambda = -1$. Relationships connecting parameters α_e, β_e, γ_e with ω_e, $\omega_e x_e$ and B_e can be found in [98]

and in [99]. The energy of the complete Hamiltonian is thus obtained by finding the eigenvalues of the different operators on the chosen basis set[1].

3.2.1 Eigenvalues of the Hamiltonian

In the previous section we have seen how to derive a simple form of the effective Hamiltonian for a well defined vibronic state $|nv\rangle$. In this section we provide the eigenvalues of the different contribution skipping sometimes the complete derivation procedure that can be found in [93, 94, 96]. The first term to solve is the rotational Hamiltonian that is proportional to $\hat{N}^2$. We can thus rewrite this terms as function of $\hat{J}$ and $\hat{S}$ as

$$\hat{H}_{\text{rot}} = B_{nv}\hat{N}^2 = B_{nv}(\hat{J}-\hat{S})^2 = B_{nv}(\hat{J}^2+\hat{S}^2-2\hat{J}\cdot\hat{S}) \tag{3.30}$$

Since the operators $\hat{J}^2$ and $\hat{S}^2$ are already diagonal in the Hund case (a) basis set, the eigenvalues are simply $J(J+1)$ and $S(S+1)$ respectively. The dot product cannot be directly evaluated on this basis, since it can mix terms of different Σ. To perform this calculation, we can write the dot product by using spherical tensors as

$$\hat{J}\cdot\hat{S} = \sum_q (-1)^q T^1_{-q}(\hat{J}) T^1_q(\hat{S}) \tag{3.31}$$

where the q index ranges from $q = -1, 0, +1$.

Since the $\hat{S}$ operator is defined in the molecules-fixed axis, while the operator $\hat{J}$ has to be defined in an external coordinate system, the spherical tensor base on $\hat{J}$ has to be rotated into the external coordinate system. This can be done by applying a rotational matrix on the spherical tensor based on $\hat{J}$ and the dot product can be solved providing a total rotational energy contribution equal to

$$\begin{aligned}
&\frac{1}{B_{nv}}\langle JS\Omega\Lambda\Sigma M|\hat{H}_{\text{rot}}|JS\Omega'\Lambda\Sigma' M\rangle = \\
&\delta_{\Omega\Omega'}\delta_{\Sigma\Sigma'}[J(J+1)+S(S+1)]- \\
&2\sqrt{J(J+1)(2J+1)}(-1)^{J-\Omega}\begin{pmatrix} J & 1 & J \\ -\Omega & \Omega-\Omega' & \Omega' \end{pmatrix} \\
&\sqrt{S(S+1)(2S+1)}(-1)^{S-\Sigma}\begin{pmatrix} S & 1 & S \\ -\Sigma & \Sigma-\Sigma' & \Sigma' \end{pmatrix}
\end{aligned} \tag{3.32}$$

[1] A first estimation of the total energy of the rovibrational motion of the nuclei, ignoring the spin dependent contributions, can be obtained using the Dunham expansion series [99]

$$E_T = \sum_{kl} Y_{kl}\left(v+\frac{1}{2}\right)^k [J(J+1)]^l \tag{3.28}$$

where the coefficients are

$$Y_{10}\approx\omega_e,\quad Y_{20}\approx\omega_e x_e,\quad Y_{01}\approx B_e,\quad Y_{02}\approx D_e,\quad Y_{11}\approx\alpha_e,\ \ldots \tag{3.29}$$

where a general Wigner $3-j$ symbol is defined in terms of Clebsch-Gordon coefficients by

$$\begin{pmatrix} j_1 & j_2 & j_3 \\ m_1 & m_2 & m_3 \end{pmatrix} = \frac{(-1)^{j_1-j_2-m_3}}{\sqrt{2j_3+1}} \langle j_1 m_1 j_2 m_2 | j_3(-m_3) \rangle$$

while δ_{ij} simply denotes the Kronecker-delta function.

The spin-orbit effective Hamiltonian term is equal to

$$\hat{H}_{SO} = A_{nv} \hat{L}_z \hat{S}_z \tag{3.33}$$

that is already diagonal on the basis set with eigenvalues

$$\langle JS\Omega\Lambda\Sigma M | \hat{H}_{SO} | JS\Omega\Lambda\Sigma M \rangle = A_{nv}\Lambda\Sigma \tag{3.34}$$

The two contributions, deriving from both the coupling of electron spins with each other and the coupling of the electron spin to the rotation of the nuclei, are represented by $\hat{H}_{SS}$ and $\hat{H}_{SR}$ terms which are respectively equal to

$$\begin{aligned} \hat{H}_{SS} =& \frac{2}{3}\lambda_{nv}(3\hat{S}_z^2 - \hat{S}^2) \\ \hat{H}_{SR} =& \gamma_{nv}\hat{N} \cdot \hat{S} \end{aligned} \tag{3.35}$$

The spin-spin Hamiltonian $\hat{H}_{SS}$ is diagonal in the Hund case (a) basis set. In fact, the operator $\hat{S}_z^2$ has the eigenvalue Σ, while the operator $\hat{S}^2$ has the eigenvalue $S(S+1)$. The eigenvalue of the first Hamiltonian is therefore

$$\langle JS\Omega\Lambda\Sigma M | \hat{H}_{SS} | JS\Omega\Lambda\Sigma M \rangle = \frac{2}{3}\lambda_{nv}(3\Sigma^2 - S(S+1)) \tag{3.36}$$

The spin-rotation Hamiltonian $\hat{H}_{SR}$ can be diagonalized, similarly to the case of the rotational operator. Since the total angular momentum $\hat{N}$ can be expressed as $\hat{N} = \hat{J} - \hat{S}$, the Hamiltonian $\hat{H}_{SR}$ has a term of the type $-\hat{S}^2$ that is diagonal over the Hund's case (a) basis and a term $\hat{J} \cdot \hat{S}$ that can mix states with different Σ values. Since we have already calculated the eigenvalues of this latter operator, we can directly write down the eigenvalues of the spin-spin operator as

$$\begin{aligned} &\langle JS\Omega\Lambda\Sigma M | \hat{H}_{SR} | JS\Omega'\Lambda\Sigma' M \rangle = \\ &\gamma\sqrt{J(J+1)(2J+1)}\ (-1)^{J-\Omega} \begin{pmatrix} J & 1 & J \\ -\Omega & \Omega-\Omega' & \Omega' \end{pmatrix} \\ &\sqrt{S(S+1)(2S+1)}\ (-1)^{S-\Sigma} \begin{pmatrix} S & 1 & S \\ -\Sigma & \Sigma-\Sigma' & \Sigma' \end{pmatrix} \\ &- \gamma\delta_{\Omega\Omega'}\delta_{\Sigma\Sigma'}S(S+1) \end{aligned} \tag{3.37}$$

Another important contribution is the Λ-doubling term $\hat{H}_{LD}$, resulting from the perturbation of a Π state, i.e. $\Lambda = 1$, by a different electronic $\Lambda = 0$ state, i.e. Σ

state. The effect of this interaction is to separate levels of different parity, which otherwise are degenerate. These contributions are in general not important unless a Σ state is nearby. In the case of $a^3\Pi$ state of CO, the $a'^3\Sigma^+$ state is located around 7000 cm^{-1} higher energy. The $v = 4$ vibrational level of the $a^3\Pi$ is only 200 cm^{-1} lower than the first vibrational state in $a'^3\Sigma^+$. For this reason, the coupling between these different electronic states has been included in the complete effective Hamiltonian. These terms are the following

$$\begin{aligned}\hat{H}_{LD} =&(o_{nv} + p_{nv} + q_{nv}) \sum_{q=\pm1} e^{-2qi\psi} T^1_q(\hat{S}) T^1_q(\hat{S}) \\ &- (p_{nv} + 2q_{nv}) \sum_{q=\pm1} e^{-2qi\psi} T^1_q(\hat{J}) T^1_q(\hat{S}) \\ &+ q_{nv} \sum_{q=\pm1} e^{-2qi\psi} T^1_q(\hat{J}) T^1_q(\hat{J})\end{aligned} \tag{3.38}$$

where the only non-zero matrix elements are those which connect the components $\Lambda = +1$ and $\Lambda = -1$. The coefficients o_{nv}, p_{nv} and q_{nv} are the usual spectroscopic coefficients, and in many articles they are reported already grouped as they appear, i.e. $(o_{nv} + p_{nv} + q_{nv})$, $(p_{nv} + 2q_{nv})$ and q_{nv}.

There are two central points concerning the Λ-doubling Hamiltonian: first, it can only connect states of different Λ and same parity. Second, the eigenvalues of $\hat{H}_{LD}$, in a definite-parity basis set, can be written as

$$\begin{aligned}&\langle JS\Omega\Lambda\Sigma M \pm |\hat{H}_{LD}| JS\Omega'\Lambda\Sigma' M\pm\rangle = \pm\frac{1}{2}(-1)^{J-S} \\ &\Big[(o_{nv} + p_{nv} + q_{nv})\delta_{\Omega+\Omega',0}\sqrt{(S-\Sigma-1)(S-\Sigma)(S+\Sigma+1)(S+\Sigma+2)} \\ &- (p_{nv} + 2q_{nv})\delta_{\Omega+\Omega',1}\sqrt{(J-\Omega+1)(J+\Omega)(S-\Sigma)(S+\Sigma+1)} \\ &+ q_{nv}\delta_{\Omega+\Omega',2}\sqrt{(J-\Omega+1)(J-\Omega+2)(J+\Omega-1)(J+\Omega)}\Big]\end{aligned} \tag{3.39}$$

while, if a non definite-parity basis set is used, it follows a much more complicated expression. The three terms explicitly show that the Λ-doubling Hamiltonian have matrix elements with $\Delta\Omega = 0, \pm1$.

The last contribution that we are going to consider is the centrifugal distortion. Since the rotational constant $B_n(r)$ depends on internuclear distance r, a second order correction term arises to be proportional to the fourth power of the operator $\hat{N}$ as

$$\hat{H}_{\text{rotcd}} = -D_{nv}\hat{N}^4 = -D_{nv}(\hat{N})^2(\hat{N})^2 \tag{3.40}$$

The eigenvalues of this operator can be found in close analogy to what has been done for the rotational terms, which depend on $\hat{N}^2$.

Also the other parameters in Eq. 3.14 depend on the internuclear distance r, and second order correction terms can be derived for all the relative operators. If

we consider the spin-orbit term, involving the coefficient $A_n(r)$ over the internuclear distance, we can derive the centrifugal distortion second order correction term to the spin-orbit as

$$\hat{H}_{SOcd} = \frac{A_{nDv}}{2}\{\hat{N}^2, T_0^1(\hat{L})T_0^1(\hat{S})\} \tag{3.41}$$

where A_{nDv} is the centrifugal distortion coefficient. All of these terms arise from second order coupling between the rotations of the molecules. The main other important second order terms are the following

$$\begin{aligned}
\hat{H}_{SScd} =& \frac{\lambda_{nDv}}{2}\{\hat{N}^2, 3\hat{S}_z^2 - \hat{S}^2\} \\
\hat{H}_{SRcd} =& \frac{\gamma_{nDv}}{2}\{\hat{N}^2, \hat{N}\cdot\hat{S}\} \\
\hat{H}_{LDcd} =& \frac{o_{nDv} + p_{nDv} + q_{nDv}}{2}\sum_{q=\pm1}\{\hat{N}^2, e^{-2qi\psi}T_q^1(\hat{S})T_q^1(\hat{S})\} \\
&- \frac{p_{nDv} + 2q_{nDv}}{2}\sum_{q=\pm1}\{\hat{N}^2, e^{-2qi\psi}T_q^1(\hat{J})T_q^1(\hat{S})\} \\
&+ \frac{q_{nDv}}{2}\sum_{q=\pm1}\{\hat{N}^2, e^{-2qi\psi}T_q^1(\hat{J})T_q^1(\hat{J})\}
\end{aligned} \tag{3.42}$$

whose treatments and solutions is described in the already previously cited publications. These terms are usually neglected in the majority of the molecular coefficient database because with the common resolution of the measured spectra their contribution cannot be resolved.

3.2.2 Molecular Constants of CO

Since the state with which we are working is an $a^3\Pi$ state, using the definite parity basis vectors we can write the eigenvector as

$$|(\Lambda = 1)(S = 1)(\Sigma = \Omega - 1)J\Omega M\pm\rangle \tag{3.43}$$

where Ω can assume only values 0, 1, and 2. All the different constants used in the previous sections to describe the different terms of the Hamiltonian and the relative eigenvalues are listed in Tab. 3.1, where the most accurate coefficients present in literature are reported. These parameters can be accurately determined from precise spectroscopic data. There are several publications in which this constants are derived, with different accuracies, but we have reported only the most precise. For ^{12}CO, experimental data used to extract molecular coefficients are available in [90], mainly based on the Λ-doubling splitting by means of radio-frequency and also addressed in millimeter and sub-millimeter wave spectroscopy of transitions between rotational states in different vibrational levels as reported in [100–102] and [103]. Rovibrational spectra [104] and [105] provide almost all the parameters for the different vibrational states up to $v = 3$; comparison with previous publications as [106]

and [107] is also reported. Optical spectra involving transitions from the absolute ground state to the $a^3\Pi$ state are presented in [106] and [86].

A list of these parameters for ^{12}CO is shown in Tab. 3.1 for the $v = 0$ and the $v = 1$ vibrational states in the excited $a^3\Pi$ state. All the units are in cm^{-1}. The parameter E_{ne} is an offset parameter chosen in a way that the zero energy corresponds to the absolute ground state of the carbon monoxide, i.e. the $X^1\Sigma^+, v = 0, N = 0$ state.

Some of the cited articles use the R^2- or N^2-Hamiltonian formalism[2] and the obtained parameters cannot be directly compared. For this purpose the transformation listed here have been used [104]

$$\begin{aligned} A^N_{nv} &= A^R_{nv} - A^R_{nDv} - \gamma^R_{nv} \\ B^N_{nv} &= B^R_{nv} + q_{nv}/2 + 2D^R_{nv} \\ \gamma^N_{nv} &= \gamma^R_{nv} - p_{nv}/2 \\ A^N_{nDv} &= A^R_{nDv} \\ D^N_{nv} &= D^R_{nv} \\ a_{nv} &= -o_{nv} \\ p^+_{nv}/2 &= p_{nv} \\ q^+_{nv}/2 &= q_{nv} \end{aligned} \tag{3.44}$$

where the parameters denoted with the superscript R are those obtained in the $R-$Hamiltonian formalism, while the superscript N indicates the coefficient obtained in the $N-$Hamiltonian formalism. See for example [102]. Special attention has to be paid on the parameter A_{nv}: sometime this parameter comes from fitting procedures regarding the parameter A_{nDv} or γ_{nv}. As described in [96], it is not possible to fit the parameters A_{nDv} and γ_{nv} at the same time and the value of A_{nv} is influenced by the choice of the parameter varied. For this reason the comparison between A_{nv} values from different articles has to be made carefully.

3.2.3 Energy Levels Calculations

The molecular coefficient values listed in Tab. 3.1 have been used to derive the energy levels of the lower rotational states in the lowest vibrational state $v = 0$ of the electronic state $a^3\Pi$ with $\Omega = 0, 1, 2$. The results of this calculation are shown in Fig. 3.2, where energies are indicated in cm^{-1}. The three manifolds are labelled by the different values of Ω. For every rotational level, the Λ-doubling splitting is also shown together with its parity. Finally, the energy of the $|v = 1, J = 1, -\rangle$ state was also calculated, yielding a transition energy for the vibrational excitation

[2]We have derived the rotational Hamiltonian as $\hat{H}_{\rm rot} = B_{nv}\hat{N}^2$. In many paper the rotational Hamiltonian is written in terms of the operator $\hat{R}^2 = (\hat{N} - \hat{L})^2$ and the spectroscopic molecular constants used in the two cases have to be carefully matched.

Table 3.1: Molecular parameters of the $a^3\Pi$ state of ^{12}CO in the vibrational level $v = 0$ and $v = 1$. All parameters are given in cm^{-1}. The number inside parenthesis indicates the uncertainty over the last reported digits for each coefficient.

Parameter $a^3\Pi$ of ^{12}CO	Value [cm^{-1}]	
E_{ne}	48471.537(2)	
ω_e	1743.76134(73)	
$\omega_e x_e$	14.578941(462)	
$\omega_e y_e$	-0.0049200(764)	
B_e	1.69115125(817)	
D_e	$6.2493(794)\cdot10^{-6}$	
α_e	0.0189083(114)	
γ_e	$-6.126(286)\cdot10^{-5}$	
β_e	$1.801(638)\cdot10^{-7}$	
	$v = 0$	$v = 1$
A_{nv}	41.432(2)	41.278(3)
A_{nDv}	$1.06(11)\cdot10^{-3}$	$-3.49(8)\cdot10^{-4}$
B_{nv}	1.68167658(6)	1.662623(2)
D_{nv}	$6.3771(7)\cdot10^{-6}$	$6.412(5)\cdot10^{-6}$
λ_{nv}	$1.78(7)\cdot10^{-2}$	0.0268(6)
γ_{nv}	$1.40(13)\cdot10^{-2}$	0
$o_{nv} + p_{nv} + q_{nv}$	0.8753(14)	0.9113(3)
$p_{nv} + 2q_{nv}$	$5.60(29)\cdot10^{-3}$	$4.14(3)\cdot10^{-3}$
q_{nv}	$6.16(4)\cdot10^{-5}$	$6.3(4)\cdot10^{-5}$

$a^3\Pi_1 : |v = 1, J = 1, -\rangle \leftarrow |v = 0, J = 1, +\rangle$ of 1714.52 cm^{-1} ($\sim$ 5.83 μm). Using the frequency standard referenced mid-IR radiation discussed in Chapter 1 and 2, at the end of this thesis we will see that we measure this transition at $\sim$1714.49 cm^{-1}, about 1 GHz away.

3.2.4 Effect of External Magnetic Field

When the molecules, as well as atoms, are subjected to an external magnetic field $\boldsymbol{B}$, the Zeeman effect induces a splitting of the energy levels. This splitting is proportional to the molecule magnetic moment operator, written as the sum of the orbital and spin contributions, each one multiplied by the relative gyromagnetic factor g_L and g_S, as

$$\hat{\mu} = -\mu_B(g_L\hat{L} + g_s\hat{S}) \tag{3.45}$$

where μ_B is the Bohr magneton with $g_L = 1$ and $g_S \simeq 2.00232$. The Zeeman Hamiltonian can thus be written as

$$\hat{H}_{\text{Zeeman}} = -\boldsymbol{B} \cdot \hat{\mu} = \mu_B \boldsymbol{B} \cdot (g_L\hat{L} + g_s\hat{S}) \tag{3.46}$$

If no higher accuracy is needed, all the other contributions arising from the nuclear spin or from the rotating motion of the molecule can be neglected. Using the spherical tensor operator, the dot product can be written as

$$\hat{H}_{\text{Zeeman}} = \sum_p (-1)^p \mu_B T^1_p(\boldsymbol{B})(g_L T^1_{-p}(\hat{L}) + g_S T^1_{-p}(\hat{S})) \tag{3.47}$$

where the index p refers to the space-fixed coordinate system over which the spherical tensor, acting on the magnetic field $\boldsymbol{B}$, can be easily defined. The previous equation results in the following eigenvalues

$$\begin{aligned}
&\langle JS\Omega\Lambda\Sigma M|\hat{H}_{\text{Zeeman}}|J'S\Omega'\Lambda\Sigma'M'\rangle = \\
&\sum_p \mu_B T^1_p(\boldsymbol{B})(-1)^{M-\Omega+p}\begin{pmatrix} J & 1 & J' \\ -M & -p & M' \end{pmatrix}\begin{pmatrix} J & 1 & J' \\ -\Omega & \Omega-\Omega' & \Omega' \end{pmatrix} \\
&\sqrt{(2J+1)(2J'+1)} \\
&\left[g_L\Lambda\delta_{\Sigma\Sigma'} + g_S(-1)^{S-\Sigma}\sqrt{S(S+1)(2S+1)}\begin{pmatrix} S & 1 & S \\ -\Sigma & -\Sigma-\Sigma' & \Sigma' \end{pmatrix}\right]
\end{aligned} \tag{3.48}$$

In reference to the symmetrization of the basis under parity operator expressed in Eq. 3.4, when the Hamiltonian is evaluated over the defined parity basis vectors, it turns out that the Zeeman Hamiltonian only mixes states with the same parity.

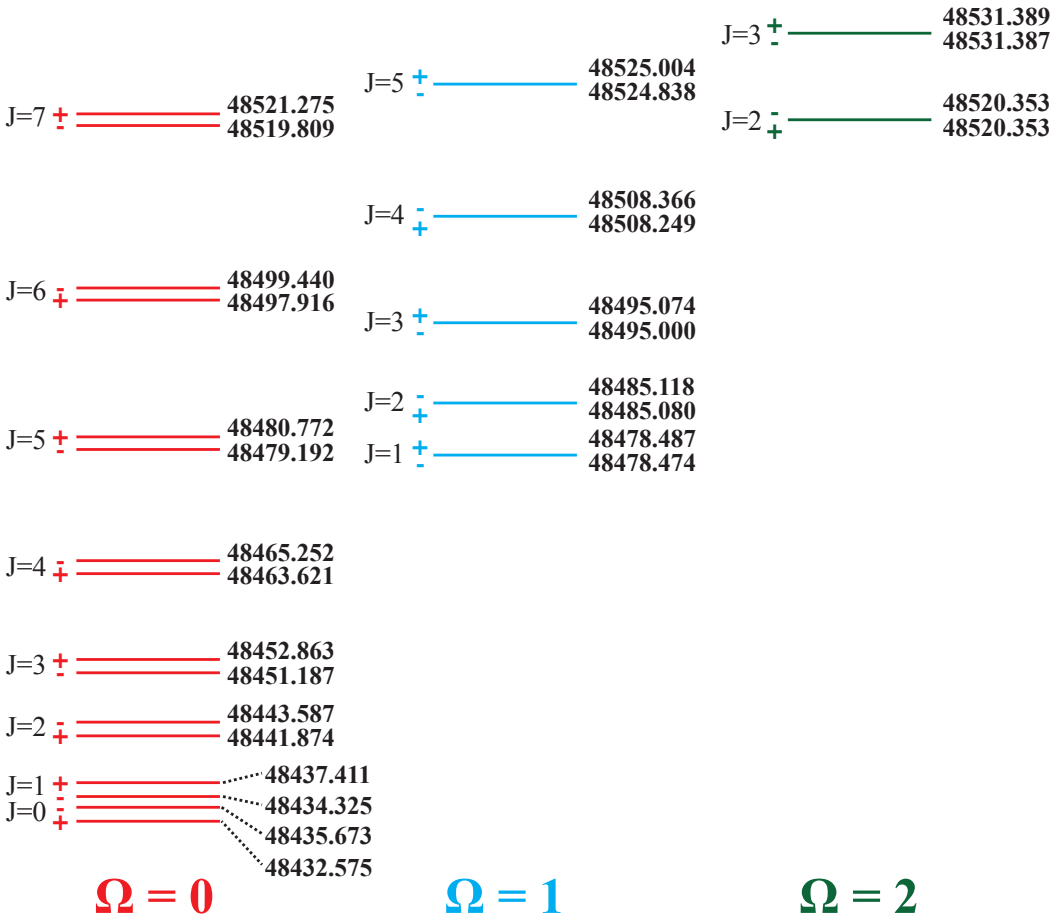

Figure 3.2: Rotational levels in the $a^3\Pi$, $v = 0$ state. The spin-orbit coupling determines three manifold corresponding to the different Ω values. Each rotational level is then split into two components with opposite parity by the Λ-doubling term. The energy of each level is expressed in cm^{-1}, where the zero energy corresponds to the energy of the absolute ground state of the molecule $X^1\Sigma^+, v = 0, N = 0$.

Chapter 4

Experimental Setup

A sketch of the molecular beam is shown in Fig. 4.1. A mixture of 20% carbon monoxide in krypton is expanded through the nozzle of a refrigerated, pulsed valve. The valve is contained in a first vacuum chamber, which is maintained at a pressure of about 10^{-5} mbar by means of a 520 l/s turbomolecular pump backed by a membrane pump. A 1-mm diameter skimmer divides the first chamber from a second one, which is maintained at an average pressure between 10^{-7} mbar and 10^{-6} mbar by means of two 260 l/s turbomolecular pumps backed by the same membrane pump. The valve is operated at a 10 Hz repetition rate and it produces a short packet of supersonic molecules. After the skimmer, the molecules are selectively excited from their electronic ground state to the first excited state $a^3\Pi_1$ in the $|v = 0, J = 1, +\rangle$ level by means of a pulsed laser emitting at 206 nm (see Fig. 4.2 for the energy levels diagram of CO). From this intermediate state, the desired vibrational transition is induced by means of the mid-IR laser, described in Chapter 1 and 2, at wavelength of about 6 μm that transfers the molecules into the $|v = 1, J = 1, -\rangle$ level. This transition takes place in a region where the magnetic field is precisely controlled with an external set of three pairs of coils, allowing to perform the transition measurements at different values and directions of the magnetic field. After this second excitation the molecules fly towards the detector: they can be either revealed using an Auger-electrons detector, where the whole arrival time distribution is recorded, or by means of resonance multi-photon ionization (REMPI). In the latter case a third pulsed laser, emitting at about 283 nm, ionizes the molecules with a resonant two-photon process via the $b^3\Sigma^+$ state. All the laser excitations and detections take place in this second chamber where, due to the lower pressure, collisions between background molecules and the beam are negligible.

4.1 Apparatus

The molecules are introduced into the vacuum region by means of a modified series 99 General Valve (Parker Hannifin Corp.). This valve has a 0.76 mm aperture

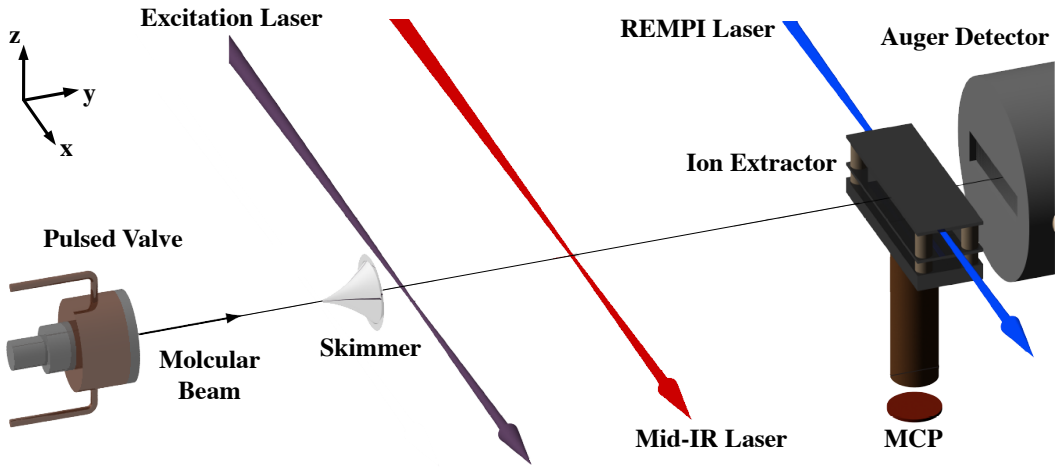

Figure 4.1: Overview of the molecular beam. The beam is generated by a pulsed, cooled valve and than skimmed by a 1 mm diameter skimmer. The supersonic expansion prepares the molecules in the lower rotational levels of their ground state. They are than selectively excited by the excitation laser at around 206 nm. After interacting with the frequency standard referenced mid-IR laser, the molecules continue their flight towards the detecting region where they can be revealed by means of an Auger-electrons detector or by means of resonance multi-photon ionization.

sealed by a conical poppet that is connected to a ferrite element. To open the valve, a short pulse of current (typically $\sim$100 μs, 300 V) is sent through a solenoid surrounding the ferrite element. The temperature of the valve body is controlled by a flow of cold nitrogen gas, which is pre-cooled with liquid nitrogen, and a resistive heater. The temperature of the valve is monitored with a type-K thermocouple and a PID controller (Schneider Electric SE, Eurotherm 2408) acts on the resistive heater stabilizing the temperature at the desired value. The commercial valve has been modified so that the pre-load on the spring counteracting the motion of the ferrite element can be adjusted. This operation can be carried out without breaking the vacuum and it allows to fine adjust the valve sealing and opening conditions in a large range of temperature. Adjustment of the valve position can also be done without breaking the vacuum. The backing pressure of the valve is set to 1 bar (2 bar absolute).

The supersonic expansion has the great advantage of cooling down the molecules: the internal energy of the molecules is converted, during the expansion, in kinetic energy with the effect of a narrow distribution of population in the lowest energy levels and a supersonic translational velocity. Since the expansion is a basic key for the experiment, we briefly discuss the underlying physics, see references [108, 109] for a more complete analysis.

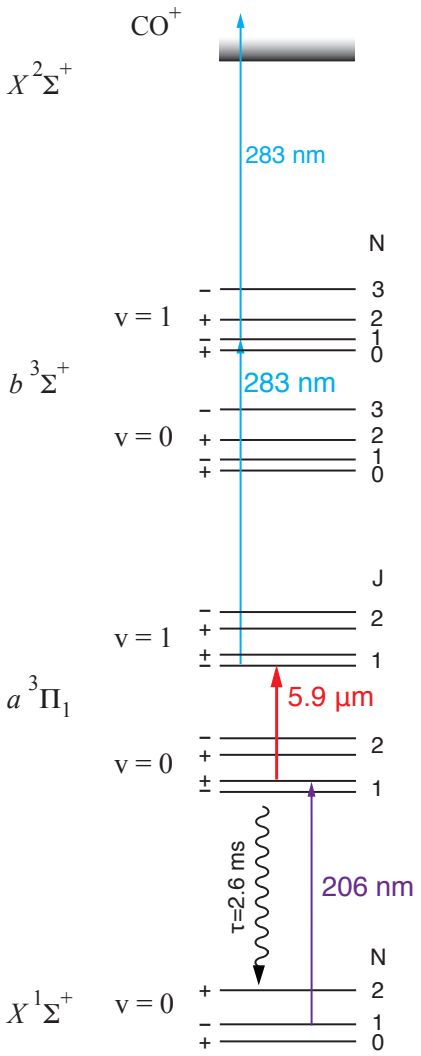

Figure 4.2: Energy level diagram of the relevant states of CO. Thanks to the supersonic expansion, only the lower rotational levels of the ground state $X^1\Sigma^+, v = 0$ are populated. The excitation laser at around 206 nm is used to induce the transition $a^3\Pi_1 : |v = 0, J = 1, +\rangle \leftarrow X^1\Sigma^+ : |v = 0, N = 1\rangle$ that decays back to the ground state with decay time of 2.6 ms. Once the molecules are excited, a vibrational excitation to the state $|v = 1, J = 1, -\rangle$ is triggered by the mid-IR laser. For REMPI, a third laser is used to ionize the vibrationally excited molecules passing through the intermediate state $b^3\Sigma^+ : |v = 1, N = 1\rangle$.

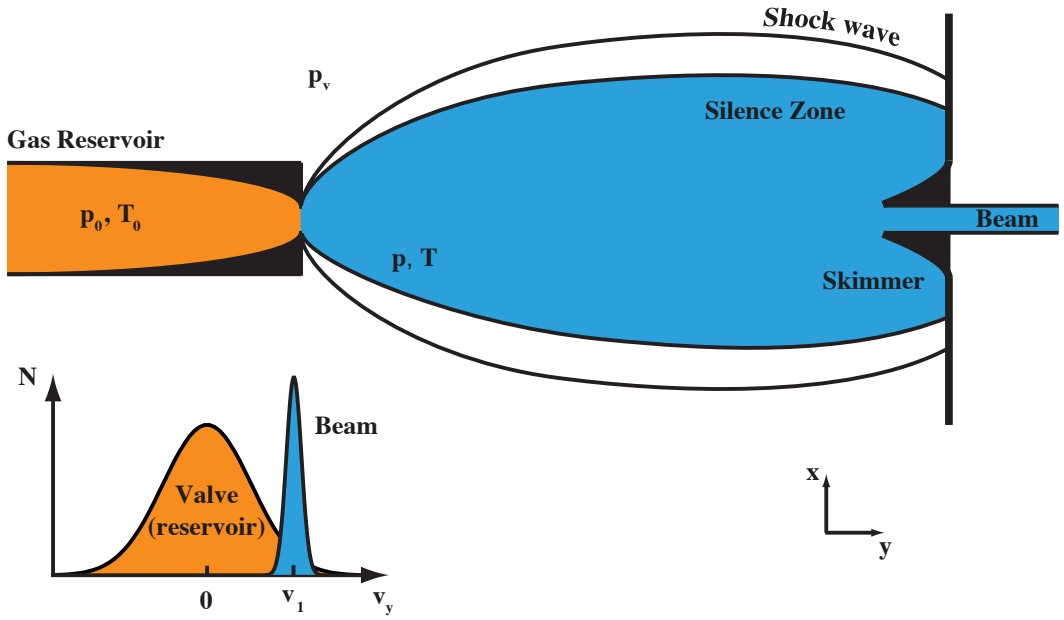

Figure 4.3: Supersonic expansion. A gas reservoir (valve) on the left contains a gas at pressure p_0 and temperature T_0 at thermal equilibrium. Once the valve opens the gas undergoes a supersonic expansion into vacuum region with pressure p_{v}. The presence of a skimmer allows for the central part of the beam to pass through it and the obtained molecular beam travels at supersonic speed over the $\hat{y}$ direction with very small velocity components in both transverse directions. The shock zone and the internal zone of silence are also indicated. In the lower plot, the distribution of velocity along the $\hat{y}$ axis $N(v_y)$ is reported when gas is stored into the reservoir (orange) and after the skimmer (blue).

4.1.1 Supersonic Expansion

In general, the expansion of a gas at high pressure p_0 into vacuum, at pressure p_{v}, say five or more orders of magnitude lower than p_0, can occur via an effusive or via a supersonic expansion. In an effusive expansion the number of collisions experienced by the molecules leaving the reservoir tends to zero. In this case the mean free path of the molecules inside the reservoir is larger than the diameter of the hole connecting the reservoir to the vacuum. The velocity distribution of an effusive beam depends on the temperature T_0 of the reservoir.

A supersonic expansion is schematized in Fig. 4.3. To obtain a supersonic expansion, the number of collisions inside the nozzle must be large. This case can be described using the continuum model of gas flow in which the gas is described in terms of continuum mass distribution instead of single particles. At high initial pressure p_0 the effect of viscosity can be neglected and the expansion is so fast that the particles are not able to exchange heat with the surroundings. The expansion

can thus be considered adiabatic and isentropic to a good approximation. We can therefore write the total energy of a mole of the gas with molar mass M in terms of its enthalpy $H = U + pV$ and its kinetic-flow energy $Mv^2/2$. Here, U is the internal energy, V the volume of the container and p its pressure. Since the total energy must be conserved we can write

$$U_0 + p_0V_0 + \frac{1}{2}Mv_0^2 = U + pV + \frac{1}{2}Mv^2 \tag{4.1}$$

where the left side of the equation represents the total energy inside the reservoir and the right side the total energy after the expansion in the vacuum chamber. Usually the mass exiting the valve can be neglected with respect to the total mass of the gas in the reservoir and thermal equilibrium inside the valve is assumed. In this case the mean velocity of the molecules inside the reservoir, v_0, can be neglected. Since the pressure in the vacuum chamber is much smaller than the source pressure, Eq. 4.1 simplifies as

$$U_0 + p_0V_0 = U + \frac{1}{2}Mv^2 \tag{4.2}$$

If all the initial energy $U_0 + p_0V_0$ is converted into kinetic energy, we obtain a cold molecular beam traveling at velocity $v_{\max}$

$$v_{\max} = \sqrt{\frac{2H_0}{M}} \tag{4.3}$$

For a calorically perfect gas, the molar heat capacity C_p at constant pressure is assumed to be constant and the enthalpy can be written in terms of temperature as $H(T_0) = C_\mathrm{p}T_0$. We thus can write Eq. 4.3 as

$$v_{\max} = \sqrt{\frac{2C_\mathrm{p}T_0}{M}} \tag{4.4}$$

If the ideal gas undergoes an adiabatic expansion, the final gas temperature can be related to the initial pressure p_0, temperature T_0 or volume V_0 by the following relations

$$\begin{aligned} \frac{T}{T_0} &= \left(\frac{p}{p_0}\right)^{\frac{\gamma-1}{\gamma}} = \left(\frac{p}{p_0}\right)^{\frac{R}{C_\mathrm{p}}} \\ \frac{T}{T_0} &= \left(\frac{V}{V_0}\right)^{1-\gamma} = \left(\frac{V}{V_0}\right)^{\frac{1}{1-C_\mathrm{p}/R}} \end{aligned} \tag{4.5}$$

where p denotes the final pressure after the expansion, R the ideal gas constant and $\gamma = C_\mathrm{p}/C_\mathrm{v} = \frac{f+2}{f}$ is the heat capacity ratio, or adiabatic coefficient, calculated using the molar heat capacitance at constant volume C_v and expressed in terms of number of degrees of freedom f. In the previous equation, the relation $C_\mathrm{p} = \gamma R/(\gamma - 1)$ for ideal gases is used.

As shown in Fig. 4.3, the rapid expansion creates a shock zone with thickness depending on the density of the background gas in the vacuum chamber. The

internal isentropic region is called *zone of silence* because the speed of sound in the expanding gas drops to about zero. Here the expansion properties are independent of p, because the supersonic flow in this region is not influenced by any external conditions.

For the CO we have $\gamma = 7/5$ and $C_\mathrm{p} = 7R/2$. Thus a reservoir at room temperature yields a maximum velocity of about 790 m/s. However, equations 4.4 and 4.5 suggest that both the final temperature T and velocity v_max can be reduced by acting on the parameters T_0, M and C_p—which is desirable because spectroscopy is facilitated by cold and and slow beams. If for example the reservoir temperature is lowered to 90 K, we obtain a beam velocity of about 430 m/s. Furthermore reducing T_0 from room temperature to 90 K results in a reduction of the final beam temperature of another factor 3. To further reduce the final temperature and velocity we have to act on the molecule mass and heat capacitance. Since there is no way to directly change the physical properties of CO, we can mix a small fraction of CO with a heavy noble gas such as krypton, in the so-called *seeding technique*. In this condition the molar mass M and the molar heat capacitance C_p have to be recalculated following the relations

$$M = \sum_i a_i M_i \quad \text{and} \quad C_\mathrm{p} = \sum_i a_i C_{\mathrm{p},i} \tag{4.6}$$

that represent the average of the molar mass M_i and the molar heat capacitance $C_{\mathrm{p},i}$ of the mixture elements weighted by their mole fractions a_i. The new average mass is higher than that of a non seeded beam and the final velocity decreases. In addition, since the carrier gases are monoatomic, their heat capacitance equal to $C_\mathrm{p} = 5/2R$, smaller than pure CO. The optimal conditions for our experiments have been found to be a mixture of 20% CO in krypton at 2.0 bar (absolute), with the valve kept at 140 K. The expected maximum velocity is 294 m/s, against an observed 310 m/s. If we assume a pressure $p = 5 \cdot 10^{-5}$ mbar, we obtain a final calculated temperature of $T \sim 0.2$ K.

It is important to notice that the estimation of final temperature refers only to the translational motion and it is used to characterize the velocity spread of the beam in the forward direction. It does not correspond to the temperature of the internal degrees of freedom of the molecules. The energy transfer between the molecules during the expansion is mediated by collisions. The collisional cross section for elastic scattering, which yields translational energy transfer, is bigger than the inelastic cross section, which yields energy transfer between rotations or vibrations. Consequently, rotations and vibrations are not cooled as efficiently as the translational motion. Thus we have

$$T_\mathrm{trans} < T_\mathrm{rot} < T_\mathrm{vib} \tag{4.7}$$

Vibrations are usually about one order of magnitude warmer than rotations that, in turn, are one order of magnitude warmer than translations.

4.2 Laser System

After the supersonic expansion and the passage through the skimmer, the CO molecules are distributed over the lowest rotational levels of the $X^1\Sigma^+$, $v = 0$ ground state. The ground state of CO has a small electric dipole moment that makes this state not suitable for Stark manipulation. The first electronic excited state, instead, presents an electric dipole moment of 1.37 Debye, more than one order of magnitude higher than in the ground state, and suitable for molecular manipulation using electric fields. This thesis work did not deal with Stark decelerators but it is part of a broader endeavor aimed at ultra-precise measurements using cold molecules. Deceleration and trapping of polar molecules are thus parts of future experiments. Moreover, the spectroscopic data available in literature for excited states are, nowadays, less accurate than for the ground state, thus making measurements on the $a^3\Pi$ state more interesting.

The transition between the states $X^1\Sigma^+$ and $a^3\Pi$ connects a singlet to a triplet spin state and is therefore spin-forbidden. However, the $a^3\Pi$ is spin-orbit coupled with the singlet state $A^1\Pi$. Since in diatomic molecules the spin-orbit coupling maintains the angular momentum along the internuclear axes, the mixing is mainly for the $|\Omega| = 1$ state. Hence, the transition can be driven with a few mJs of laser light with an appropriately narrow bandwidth. The selected transition is

$$a^3\Pi_1 : |v = 0, J = 1, +\rangle \leftarrow X^1\Sigma^+ : |v = 0, N = 1, -\rangle \tag{4.8}$$

at (1453233648 ± 5) MHz [86], corresponding to about 206.29 nm.

The laser system is shown in Fig. 4.4. It is based on an optical parametric oscillator. A frequency doubled 5 ns pulsed Nd:YAG laser at 532 nm (Spectra Physics, Quanta Ray Pro-230) with 10 Hz of repetition rate is used as primary laser source for this system. The radiation is split into two arms: the first part is frequency doubled in a BBO crystal to produce pulses at 266 nm, while the second part pumps a four mirror OPO cavity. Here two KTP crystals produce radiation at 917 nm and at 1267 nm, but only the shorter wavelength is resonant with the cavity. In order to precisely control the emitted light frequency, a commercial 917 nm cw diode laser (Toptica Photonics AG, DL 100 PRO) is used to seed the cavity and to stabilized its length. A small periodic modulation is in fact applied at the piezo on which one of the four mirrors is mounted, providing an error signal for a lock-in amplifier. The lock-in determines the deviation from the resonance and acts on the piezo to stabilize the cavity length to a multiple of the seeding wavelength. The pulsed beam exiting the OPO cavity is then combined with the 266 nm radiation in a second BBO crystal to produce the desired UV light by sum frequency generation. This system delivers about 2 mJ at 206 nm with a bandwidth of 150 MHz.

The frequency of the UV light depends directly on the frequency of the Nd:YAG laser's fourth harmonic at 266 nm. Therefore a small part of the Nd:YAG output is coupled to a temperature-controlled iodine cell for frequency stabilization. A differential photodiodes arrangement is used to measure the cell absorption independently

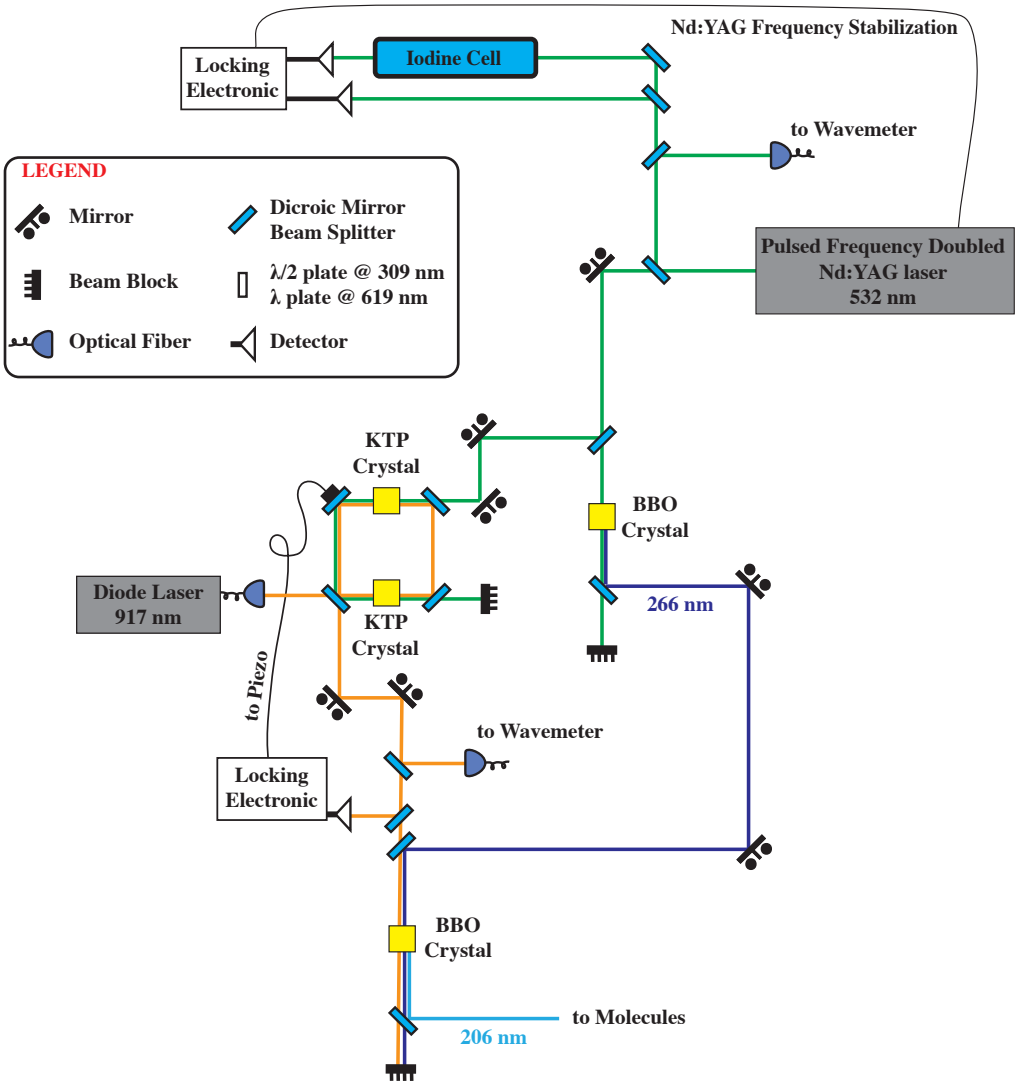

Figure 4.4: Experimental overview of the laser system used to produce radiation at 206 nm with a repetition rate of 10 Hz. The UV light is produced by sum frequency of the fourth harmonic of a Nd:YAG at 266 nm with the output of an OPO at 917 nm. The pulsed Nd:YAG laser is stabilized in frequency with a temperature-stabilized iodine cell.

from laser power shot-to-shot fluctuations. The laser is locked to the slope of the I_2 transition centered at 18789.289 cm^{-1}.

4.3 Detection of Metastable CO

Metastable CO molecules can be detected in two ways. The Auger detector allows to detect the whole molecular arrival time distribution in a single measurement. This method does not distinguish between vibrational and rotational levels in the $a^3\Pi$ state. The second method uses resonance-enhanced multi-photon ionization (REMPI) with a pulsed laser at the entrance of a time-of-flight tube and then detects the ions with a micro-channels plate (MCP). This method is state selective, as the laser is tuned on a specific transition, so only one quantum state is detected at a time. Both detectors can be mounted in the machine together but only one at a time can be used to avoid noise.

4.3.1 Auger Detector

The first detection method is relatively straight forward and consists in making the CO molecules impinge on a gold surface. At the core of this detection method there is the Auger process, which results in the release of an electron when metastable CO hits the metal surface [110], [111]. When a metastable CO molecule approaches the gold surface, an electron in the conduction band of the metal can tunnel in the lower unoccupied orbital of the molecule. The energy released during this process is transferred to the electron lying on the higher energy orbital that can now leave the molecule with non-zero kinetic energy. Every metal with a working function lower than 6 eV—the internal energy of metastable CO—is a good candidate for this process. Gold is particularly convenient because it can be easily kept clean and pure. In our setup, the target is a gold-plated copper rod[1] heated to 150°C to keep it clean. The conversion efficiency from metastable CO to electrons is estimated to be of the order of few percents [94]. Finally, the electron are collected on a MCP detector.

The main advantage of this detection method is the possibility to measure the whole arrival time distribution in each measurement cycle. On Fig. 4.5 an example of Auger detector signal is shown: the signal from the MCP is amplified (Phillips Scientific, 6954) and sent to a digital scope (Agilent Technologies, Inc., Acqiris DC438). The acquired signal is then processed and the arrival time distribution is obtained. Knowing the central peak arrival time with respect to the 206 nm laser pulse and the geometry of the machine, the molecular beam mean velocity can be derived, as well as the velocity spread.

[1] An intermediate layer of nickel with a thickness of a few microns is used to avoid diffusion of gold into the copper substrate.

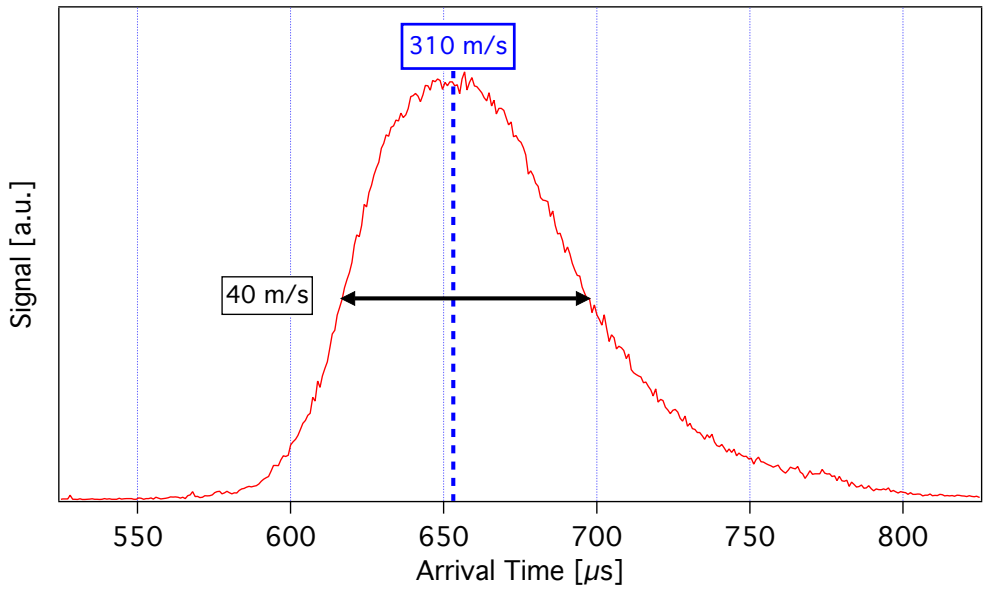

Figure 4.5: Arrival time distribution of metastable CO molecules at the Auger detector. This acquisition refers to a molecular beam obtained by supersonic expansion of a mixture of 20% CO in Krypton with initial pressure and temperature of 1 bar and 140 K. The distribution is centered around molecules that travel at 310 m/s with a velocity spread of about 40 m/s.

4.3.2 REMPI

REMPI is a general detection method that involves a resonant single or multiple photons absorption to an intermediate electronic state followed by an other absorption process that ionizes the molecule. The excitation laser is usually a tunable pulsed source that provides the high energy pulses needed to induce the multiphoton absorption. In our case, a frequency doubled Nd:YAG 10 Hz laser source (InnoLas Photonics GmbH, SpitLight 1200) is used to pump a tunable pulsed dye laser (Radiant Dyes Laser & Accessories GmbH, NarrowScan). The pump laser pumps two cuvettes with Fluorescine 27 dye diluted in methanol. A grating allows to finely tune the emission frequency, which has a line width of the order of 0.03 cm^{-1}. The emission spectrum of Fluorescine 27 spans the 541 to 571 nm region when pumped at 532 nm. This radiation is then frequency doubled with a BBO crystal. One example of REMPI spectrum is shown in Fig. 4.6. It refers to the transition $b^3\Sigma^+ : |v = 1, N\rangle \leftarrow a^3\Pi_1 : |v = 0, J = 1, -\rangle$. Once the molecules have been ionized, a constant voltage is applied to a couple of plates (indicated as 'Ion Extractor' in Fig. 4.1) to create an electric field that accelerates the molecules towards an MCP.

Unless an electric field strong enough to mix the parity of the states is present,

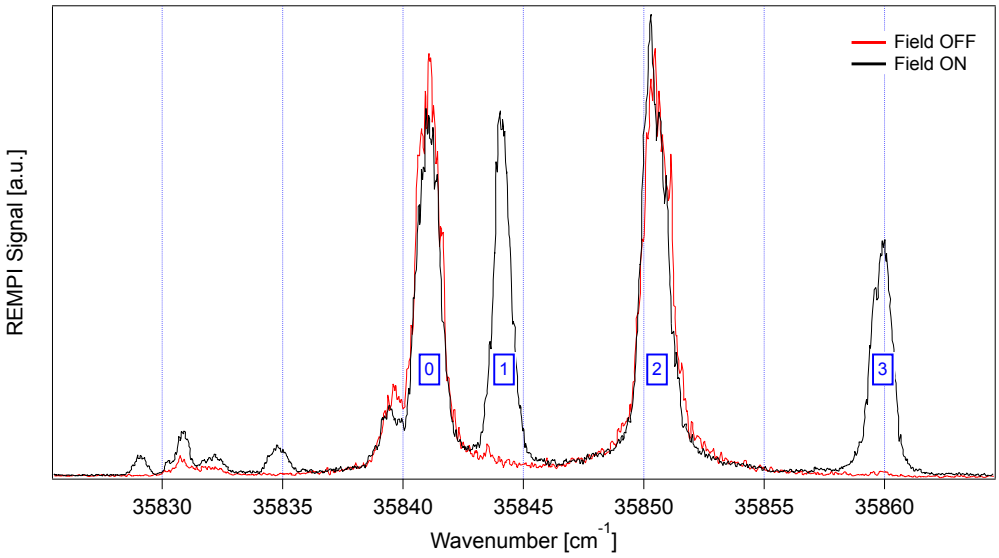

Figure 4.6: 1+1 REMPI spectrum relative to the transition $b^3\Sigma^+ : |v = 1, N\rangle \leftarrow a^3\Pi_1 : |v = 1, J = 1, -\rangle$, where the arrival rotational quantum number N is indicated on the figure inside a blue box. This spectrum is recorded using 0.3 mJ of laser power. The spectrum recorded without electric field is shown in red and the spectrum recorded with electric field is shown in black. The presence of the electric field mixes the parity of the states and disrupts the parity selection rule. The weak peaks at low energies are not assigned.

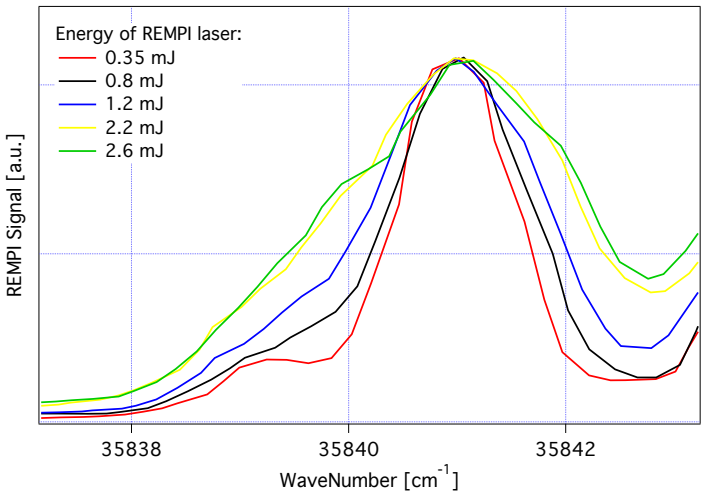

Figure 4.7: Dependence of the REMPI transition line width on pulse energy. The peak corresponds to the transition $b^3\Sigma^+ : |v = 1, N = 0\rangle \leftarrow a^3\Pi_1 : |v = 0, J = 1, -\rangle$.

only the transitions involving a change of parity can be excited. Because the initial level has negative parity, the intermediate $b^3\Sigma^+ : |v = 1, N\rangle$ state can only have positive parity, i.e. only $N = 0$ or $N = 2$ are allowed since their parity is $(-1)^N$. The REMPI spectrum corresponding to this situation is shown with red color in Fig. 4.6. However, if an electric field is present during the excitation, the parity selection rule breaks down. This situation is shown with black color.

To accurately determine all transition frequencies, power broadening has to be avoided. We thus optimized the laser power to contain the broadening effect while maintaining a good signal-to-noise ratio. Fig. 4.7 shows the effect of the REMPI laser power: the height of the reported line has been normalized to stress the effect of power broadening. A laser energy of 0.3 mJ per pulse is used to measure the transition central frequencies that are listed on Tab. 4.1. The frequency accuracy is 0.08 cm^{-1} due to the resolution and absolute calibration of the wave meter used.

Table 4.1: List of the photon energies that correspond to (1+1) REMPI transitions. The error over the reported value is 0.08 cm^{-1}, due to the resolution and calibration of the wave meter.

N	REMPI laser $[cm^{-1}]$
	$b^3\Sigma^+ : \|v = 1, N\rangle \leftarrow a^3\Pi_1 : \|v = 1, J = 1, -\rangle$
0	35841.06
1	35844.10
2	35850.41
3	35859.83
	$b^3\Sigma^+ : \|v = 0, N\rangle \leftarrow a^3\Pi_1 : \|v = 0, J = 1, +\rangle$
0	35354.42
1	35358.08
2	35365.50
3	35376.28

Chapter 5

High Resolution Spectroscopy

The resolution achieved in a spectroscopic experiment depends on several factors as the gas conditions (temperature and pressure), the laser power and beam dimension and so on. When dealing with a low-pressure gas, the resolution is usually dominated by inhomogeneous broadening due to the Doppler effect. In the past, several Doppler-free techniques have been developed to enhance the accuracy and the precision of measurements, such as saturated absorption spectroscopy, polarization spectroscopy, and two-photon spectroscopy. Supersonic beams are not intrinsically Doppler-free, but they yield a strongly reduced velocity distribution. Furthermore, when the beam is produced by supersonic expansion, the distribution of the population is compressed in the lower vibrational and rotational states and the very few collisions between particles make pressure broadening and pressure shift nearly absent. All these factors make molecular beams very advantageous for high resolution spectroscopy experiments.

This chapter introduces the main line broadening contributions, with particular attention to their line widths and line shapes. The techniques to control the residual Doppler shift and external magnetic field are then presented. We conclude with the high precision spectroscopic measurement results.

5.1 Line Broadening Mechanisms

Atomic and molecular absorption and emission lines are never monochromatic. They are characterized by a spectral distribution $g(\nu)$ around the central frequency $\nu_0 = (E_i - E_k)/h$, corresponding to the difference between the upper and lower energy state involved in the transition. The function $g(\nu)$ is called *line profile* and the frequency interval $\Delta\nu = |\nu_2 - \nu_1|$, for which $g(\nu_1) = g(\nu_2) = g(\nu_0)/2$, is named *full-width at half maximum (FWHM)* of the spectral line or simply *line width*. The line profile consists of different contributions originating both from intrinsic characteristics of the transition, such as the natural line width, and from the specific experimental conditions, such as Doppler, collisional, and transit time broadenings.

When the goal of an experiment is the determination of the central frequency of a transition, the line profile plays a leading role in the accuracy of the results.

The line profile can be expressed in terms of transmission or absorption, under the assumption of a spatially homogeneous absorber distribution and a monochromatic light source, by the Beer-Lambert law

$$I(\nu, n, L) = I_0 \exp[-\alpha(\nu, n)L] \tag{5.1}$$

where I_0 and $I(\nu, n, L)$ are the incoming and the transmitted light intensity at frequency ν, $\alpha(\nu, n)$ is the linear absorption coefficient, L is the interaction path length between light and medium and n is the density of the absorbers. In order to separate the line-shape dependence, the absorption coefficient α can be expressed as a product between the line-strength of the transition, S, and the normalized line profile $g(\nu)$

$$\alpha(\nu, n) = nSg(\nu) \tag{5.2}$$

5.1.1 Natural Line Width

The most fundamental contribution to the line profile is the natural line width originating from the energy-time uncertainty relation $\Delta t \Delta E \geq \hbar/2$. Thus, if the lifetime of a quantum state is limited to the time Δt, the uncertainty on the energy of that state must be larger than $\hbar/(2\Delta t)$. In general, when measuring the frequency of emitted or absorbed radiation between two states E_i and E_k, the energy of the emitted or absorbed photon is centered around $(E_i - E_k)$ with a spread of the order of $(\hbar/\tau_i + \hbar/\tau_k)$, where τ_i and τ_k are the lifetimes of states $|i\rangle$ and $|k\rangle$.

Thus far we have mentioned only the width of the profile. To understand the shape of the line profile, we use an analogy to the classical harmonic oscillator. We consider the case of spontaneous emission between state $E_i \rightarrow E_k$ and describe the excited electron using the classical damped harmonic oscillator model with angular frequency ω, spring force constant k, mass m and damping term γ that takes into account the radiative energy loss. The amplitude $x(t)$ of the oscillation can be derived by solving the following differential equation

$$\ddot{x} + \gamma\dot{x} + \omega_0^2 x = 0 \tag{5.3}$$

where $\omega_0^2 = k/m$. The real solution of Eq. 5.3 can be written as

$$x(t) = x_0 \mathrm{e}^{-(\gamma/2)t} \cos(\omega_0 t) \tag{5.4}$$

where the boundary conditions $x(0) = x_0$ and $\dot{x}(0) = 0$ were imposed, and the damping term is assumed to be small, i.e. $\gamma \ll \omega_0$. In this case the angular frequency $\omega_0 = 2\pi\nu_0$ corresponds to the central frequency of transition $\nu_0 = (E_i - E_k)/h$. The presence of the exponential term in Eq. 5.4 makes the amplitude of the oscillation decrease gradually over time so that the emitted frequency cannot be monochromatic, as it would be for an oscillation with constant amplitude. In order to derive

the line profile, it is more convenient to work in the frequency space and decompose the position $x(t)$ in terms of monochromatic oscillation with frequency ω and amplitude $A(\omega)$

$$x(t) = \frac{1}{\sqrt{2\pi}} \int_0^\infty A(\omega) \mathrm{e}^{i\omega t} \mathrm{d}\omega \quad \text{and} \quad A(\omega) = \frac{1}{\sqrt{2\pi}} \int_{-\infty}^\infty x(t) \mathrm{e}^{-i\omega t} \mathrm{d}t \tag{5.5}$$

The integral can be easily solved and the normalized line shape profile $g_L(\omega)$ can be calculated from module of complex amplitude $A(\omega)$ that, in the vicinity of the central frequency ω_0 where $(\omega - \omega_0)^2 \ll \omega_0^2$, reduces to the normalized Lorentzian profile

$$g_L(\omega) = \frac{\gamma/2\pi}{(\omega - \omega_0)^2 + (\gamma/2)^2} \tag{5.6}$$

The FWHM of this function is expressed by the parameter γ. If the transition takes place from a state with energy E_k and mean lifetime τ_k that can only decay to the ground state, the energy-time uncertainty relation $\Delta t \Delta E \simeq \hbar/2$ can be used to derive the frequency uncertainty $\Delta\omega$ that therefore results in

$$\Delta\omega = \gamma = 1/\tau_k \tag{5.7}$$

Furthermore, if the lower level E_i is not the ground state but can further decay with time constant τ_i to an even lower state, the Lorentzian profile line width becomes

$$\Delta\omega = \sqrt{1/\tau_i^2 + 1/\tau_k^2} \tag{5.8}$$

We have just described the case in which the line width is due to spontaneous emission from an excited state, but it can be shown that the line shape is Lorentzian also for absorption.

The natural-lifetime broadening is called *homogeneous* because it is equal for all molecules in any given sample and for a given transition. On the other side, when the probability is not the same for all molecules but depends, for example, on their velocity, we speak of *inhomogeneous broadening*. The most common example of this effect is the Doppler broadening.

5.1.2 Doppler Broadening

Doppler broadening is one of the major contributions to the line width, especially in gases at relatively low pressure, and it is due to the thermal motion of the particles undergoing the transition under investigation. Let us consider a molecule that moves with velocity $\vec{v} = \{v_x, v_y, v_z\}$ and a plane wave propagating in the $\hat{x}$ direction $\vec{E} = \vec{E}_0 \exp i(\omega t - kx)$, both described relatively to the laboratory frame with axes $\hat{x}$, $\hat{y}$, and $\hat{z}$. The angular frequency ω of the radiation in the rest frame appears Doppler

shifted[1] in the moving frame of molecule according to

$$\omega' = \omega - \vec{k} \cdot \vec{v} \tag{5.10}$$

Thus, the external radiation can be absorbed by the molecules only if ω' coincides with its eigenfrequency ω_0, i.e. when

$$\omega = \omega_0 + \vec{k} \cdot \vec{v} \tag{5.11}$$

When the molecule moves against (along) the direction of the wave propagation, the scalar product is negative (positive) and the absorption frequency is reduced (increased). Because only the component of the velocity along $\vec{k}$ leads to a Doppler shift, we rewrite Eq. 5.11 as

$$\omega = \omega_0(1 + v_x/c) \;\rightarrow\; \frac{\delta}{\omega_0} = \frac{v_x}{c} \tag{5.12}$$

where $\delta = \omega - \omega_0$ is called *detuning*. Molecules with $v_x \neq 0$ will absorb the radiation at frequencies different from ω_0 and the absorption line profile will be broadened.

In the presented experiment we use a supersonic molecular beam ($\hat{y}$ direction) that is first intersected by the mid-IR laser ($\hat{x}$) and then by the transverse REMPI laser ($\hat{z}$). Since the REMPI laser is perpendicular to the mid-IR laser beam, it acts as an aperture that selects only a small part of the molecular beam. In order to simplify the following discussion and since the Doppler broadening is only due to the molecular velocity component parallel to the excitation laser, we can restrict our analysis to the $\hat{x}$ axis. The REMPI laser beam is approximately Gaussian with a waist over the direction $\hat{x}$ of $w_x \simeq 0.7$ mm. We assume that the number of ionized molecules is proportional to the laser intensity and that they are homogeneously distributed over the REMPI laser spot. We can therefore map the Gaussian spatial distribution of the REMPI intensity to the molecule velocity distribution v_x as

$$\exp\left(-\frac{2x^2}{w_x^2}\right)dx \propto \exp\left(-\frac{2(v_x t)^2}{w_x^2}\right)dv_x \tag{5.13}$$

where we have used the relation $x = v_x t$, indicating with t the time that the molecule need to move from the valve nozzle to the ionization laser. Using Eq. 5.12 we can now map the velocity distribution to the mid-IR laser frequency as

$$\exp\left(-\frac{2(v_x t)^2}{w_x^2}\right)dv_x \propto \exp\left(-\frac{2(\omega-\omega_0)^2 c^2 t^2}{\omega_0^2 w_x^2}\right)d\omega \tag{5.14}$$

[1]Here we are dealing only with the first order Doppler effect. The second order, instead, can be written as

$$\Delta\omega^{2\text{nd}} = -\omega_0 \frac{v^2}{2c^2} \tag{5.9}$$

This term is independent of the velocity direction and cannot be removed by Doppler-free techniques such as saturation or two-photon spectroscopy.

The expected line profile is therefore Gaussian, centered at the frequency ω_0 with a full width at half maximum (FWHM) value of

$$\begin{aligned}\Delta\omega =& \sqrt{2\ln 2}\,\omega_0 \frac{w_x}{c\,t} \\ =& \sqrt{2\ln 2}\,\omega_0 \frac{w_x\, v_y}{c\,d}\end{aligned} \tag{5.15}$$

where we have expressed the time t in terms of the nozzle-REMPI distance d and mean velocity of the molecules along the molecular beam propagation direction v_y. Since in our case we have $d = 310$ mm, $w_x = 0.7$ mm and $v_y = 310$ m/s, the residual Doppler broadening can be estimated as

$$\Delta\nu = \Delta\omega/(2\pi) \simeq 150 \text{ kHz} \tag{5.16}$$

5.1.3 Transit Time Broadening

Another source of inhomogeneous broadening is due to the limited interaction time T during which the molecules interact with the laser field. If we consider a molecular beam with mean velocity $v = 300$ m/s that is intersected transversally by a laser beam of diameter 1 mm, the interaction time T is of a few microseconds. In order to derive the contribution to the line profile due to this effect, we can consider an electric field $E = E_0 \cos(\omega_0 t + \phi)$ oscillating at constant frequency ω_0 and interacting with the molecules only for a finite time interval T. The frequency spectrum associated with the electric field is determined by taking the square of its Fourier transform. Considering an unlimited interaction time between the cw field and the molecules, the result would be a delta function $\delta(\omega_0)$. In practice, due to the limited interaction time, the result is the square of a sinc function with argument $(\omega-\omega_0)T/2$. However, laser beams typically have a Gaussian beam profile. When this is taken into account, the transition line profile can be written as

$$g_T(\omega) = \frac{w}{v\sqrt{2\pi}} \exp\left(-\frac{(\omega-\omega_0)^2}{2v^2/w^2}\right) \tag{5.17}$$

where w is the waist of the beams. Therefore the transit time limited full width at half maximum (FWHM) results in

$$\Delta\omega_T = \frac{2v}{w}\sqrt{2\ln 2} \sim 2.4v/w \tag{5.18}$$

where the term $v/w = 1/T$ takes into account the limited interaction time between the molecules and the laser source. The shorter is the time, the broader is the line.

5.1.4 Overall Line Profile

In order to take into account the different broadening mechanisms, we can estimate the theoretical FWHM values relative to the different contributions presented so

Table 5.1: Estimation of full width at half maximum $\Delta\nu = \Delta\omega/(2\pi)$ due to the different broadening contributions for a molecular beam moving at the mean velocity v_y=310 m/s and a 4 mm waist of the mid-IR laser.

Type	$\Delta\nu$ [kHz]	Line shape
Natural	0.085	Lorentzian
Doppler	∼150	Gaussian
Transit Time	∼30	Gaussian

far. If we consider the 2.6 ms life-time of the excite state $a^3\Pi_1 : |v = 0, J = 1, +\rangle$ be the same as the state $a^3\Pi_1 : |v = 1, J = 1, -\rangle$, the Eq. 5.8 can be used to obtain the natural line width. Using the Eq. 5.18 we can then calculate the transit time contribution assuming a mid-IR beam waist of 4 mm and a longitudinal mean velocity $v_y \sim 310$ m/s. Since Doppler broadening has already been calculated in Eq. 5.16, we reported the different contributions, with their characteristic line shape, in Tab. 5.1.

There are other broadening contributions that are not listed in the previous discussion for example the power and collisional broadenings and the contribution of the laser frequency profile. Working with supersonic molecular beams, collisions between molecules are strongly suppressed and pressure broadening can be neglected. In our case the laser frequency profile can also be neglected because it is several orders or magnitude narrower than the measured transition spectral width. In our case the laser line width can be estimated in a few of hundreds Hz, while we measure a molecular FWHM of about 1 MHz. All the other contributions are also neglected.

Doppler broadening and transit time broadening with a Gaussian laser beam produce a Gaussian line broadening and the overall profile is the convolution of these two line shapes. Because the convolution of two Gaussian functions of type $f = A\exp -\frac{(x-x_1)^2}{2\sigma_1^2}$ and $g = B\exp -\frac{(x-x_2)^2}{2\sigma_2^2}$ is still a function of the same type with width $\sigma_{f\star g} = \sqrt{\sigma_1^2 + \sigma_2^2}$, we can therefore treat the two inhomogeneous contributions as a unique Gaussian line shape broadening with parameter $\sigma_{f\star g}$.

A more precise analysis of the Doppler broadening shows that the Gaussian profile is not a correct representation of the line shape because not all the molecules with a velocity component v_z absorb light at the exact frequency $\omega(v_z) = \omega_0(1 + v_z/c)$, but in a frequency range given by the Lorentzian profile $g_L(\omega)$. The overall line profile is a Voigt profile that can be written as

$$V(\omega, \sigma, \gamma) = \int_{-\infty}^{+\infty} G(\omega', \sigma)L(\omega - \omega', \gamma)d\omega' \tag{5.19}$$

where G and L are respectively the Gaussian and the Lorentzian centered profiles

$$G(\omega,\sigma)=\frac{1}{\sigma\sqrt{2\pi}}\exp\left(\frac{-\omega^2}{2\sigma^2}\right)\quad\text{and}\quad L(\omega,\gamma)=\frac{\gamma/\pi}{\omega^2+\gamma^2} \tag{5.20}$$

There is no analytical solution for this integral but there are fast and readily-available computational procedures for doing this. The Voigt profile can also be expressed in terms of the real part of the Faddeeva function $w_{\mathfrak{F}}(z)$

$$V(\omega,\sigma,\gamma)=\frac{\Re[w_{\mathfrak{F}}(z)]}{\sigma\sqrt{2\pi}}\quad\text{where}\quad z=\frac{\omega+i\gamma}{\sigma\sqrt{2}} \tag{5.21}$$

that can be easily implemented in a fitting program. Investigation of spectral line shapes and their analysis is a complex problem in high resolution experiment [112], but the Voigt profile is often a good compromise between trustable results and complexity in data analysis.

Now that we have described the possible line profiles, we have to understand which of them better fits our experimental data. The mid-IR laser drives the vibrational transition $|v=1,J=1,-\rangle \leftarrow |v=0,J=1,+\rangle$ in the state $a^3\Pi_1$ of CO. Once the molecules are vibrationally excited, they are state selectively detected by means of REMPI detection method. An example of such detection as function of the vibrational laser frequency is reported on the top of Fig. 5.1. The vertical unit is arbitrary.

In the bottom part of the figure the residuals of the measured data fitted with a Gaussian, Lorentzian and Voigt function are shown. For each fitting function the root mean square (rms) value is reported, which can be used for a quantitative estimation of the quality of the fit. In the Lorentzian case there is a clear modulation in the residuals that is absent in the other two cases, in fact the main difference between the Gaussian and Lorentzian profile lies on the different tails. Note that the Gaussian and Voigt residuals are similar to each other, reflecting the fact that the line-shape is mainly due to Gaussian profile. Considering the line broadening contributions listed in Tab. 5.1 we expect in fact that the main contribution is Gaussian. The fitting routine provides a Lorentzian line width consistent with the estimated value, while the Gaussian contribution results in 700 kHz, a rough agreement with the 150 kHz estimated value.

The Voigt profile results to be the best fitting function as shown from the residuals and the smallest rms value. The residual fluctuations around null-frequency value in the residual plots are mainly due to power and frequency fluctuations of the 206 nm laser used to prepare the molecules in the $a^3\Pi_1$ state. These fluctuations involve the number of molecules that are excited and their effect is therefore proportional to the number of detected molecules: this explains why the fluctuations are bigger around the transition center. For each measurements we have analyzed the residuals, with particular attention to their symmetry with respect to the transition center, and decide if reject or not the acquired data. We are interested in

the determination of the center of the absorption and the symmetry of the residual, especially on the tails of the transition, can be used to understand if uncontrolled UV laser power fluctuations or other effects have altered the data. If the residuals are symmetric, the fitting routine can accurately provide the parameter relative to the central frequency. If indeed there are different trends in the residuals, the fit can interpret these displacements as a shift of the central frequency.

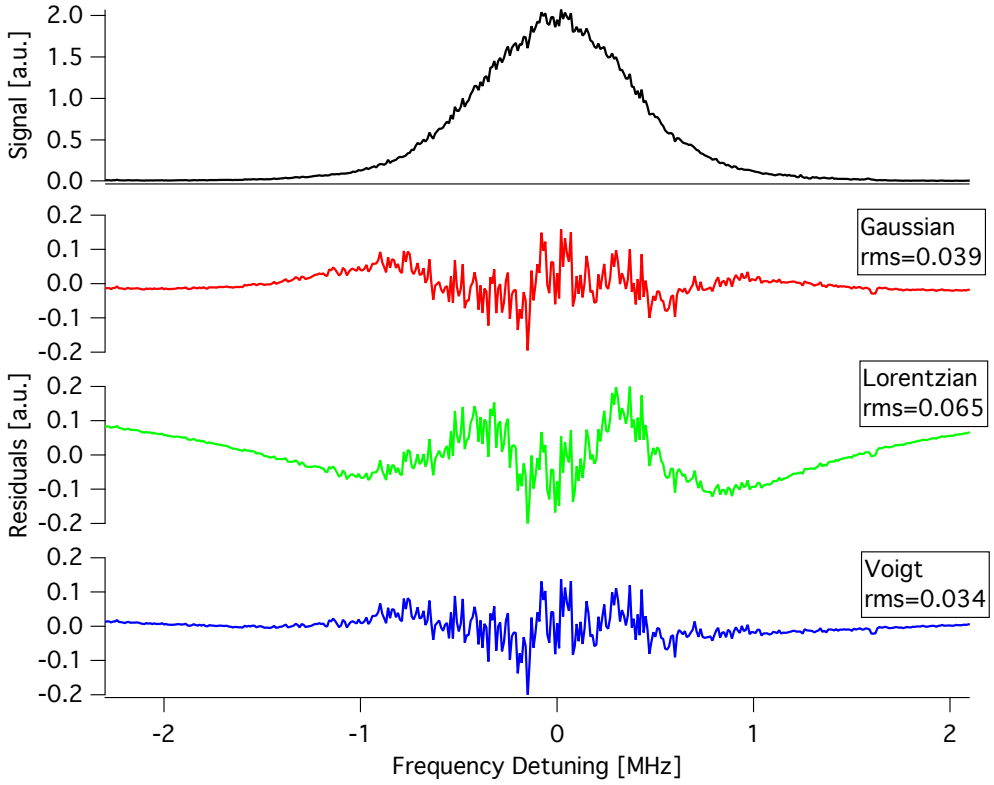

Figure 5.1: Comparison with the measured vibrational transition line-shape (top of figure) fitted using Gaussian, Lorentzian and Voigt function. Residuals are given in terms of units of the original signal. Root mean square (rms) values of the residuals are reported. The experimental data were taken in about 30 minutes acquisition time.

5.2 Controlling the First-Order Doppler Shift

Beside broadening the transition, the Doppler effect can also shift the frequency of the transition center ν_0 if the molecular beam is not perfectly perpendicular to the excitation laser. This is summarized by the relation $\nu = \nu_0 + \vec{k} \cdot \vec{v}/(2\pi)$, where ν is the laser transition frequency and $\vec{k}$ and $\vec{v}$ the wave vector of the mid-IR laser

and the molecule velocity respectively. If we consider the case of collimated laser and molecular beams that form an angle $\alpha + \pi/2$ one respects to the other, the scalar product in the previous equation does not vanish. This term induces a shift δ_ν between the real transition frequency ν_0 and its measured value ν_{meas} that can be expressed as

$$\delta_\nu = \nu_{\text{meas}} - \nu_0 = \frac{\nu_0\, v \sin\alpha}{c} \tag{5.22}$$

In order to avoid such a shift, the experimental setup has to allow for a fine adjustment of the angle between the laser light and the molecular beam. In order to optimize the alignment, a pair of parallel, counter-propagating laser beams can be used for interaction with the molecules. The Doppler shift induced by the first beam will be equal in amplitude but opposite in sign with respect to the other. Therefore, the optimal alignment between laser and molecular beam is achieved when the line profiles measured by the two beams are perfectly superimposed. The easiest way to ensure the overlapping between two beams is by retro-reflecting the laser beam with a mirror but this solution cannot be used in our case because the QCL is extremely sensible to optical feedback and good optical isolators at about 6 μm are not available. Thus, a viable alternative involves the use of a corner-cube, that reflects back the incident beam by 180°, independently on the incident beam angle. In order to avoid feedback onto the QCL, the counter-propagating beams are slightly shifted one respect to the other, without compromising their parallelism. A pinhole is used to avoid the second beam to reach the QCL. This setup is shown in Fig. 5.2 and explained below.

The QCL radiation is collimated right after the laser output by means of a 4 mm focal length aspherical lens and than split into two arms: the first is used for the lock with the DFG light while the second is expanded by a factor of 5 using a Keplerian type beam expander and sent to probe the molecular beam. Thanks to the corner cube, this arm interacts twice with the molecular beam.

When $\alpha = 0$ the IR beam intersects the molecular beam at right angle and there is no Doppler shift: the frequency of the measured transition appears to be the same for both the two antiparallel beams. In Fig. 5.3 some typical recordings of the vibrational transition $a^3\Pi_1 : |v = 1, J = 1, -\rangle \leftarrow |v = 0, J = 1, +\rangle$ are shown at different α values when both antiparallel beams interact with the molecules. When $\alpha = 0$, a single peak is clearly visible in the graph: its shape remains the same if both the two antiparallel beams are used or only one. This means that there are no broadening or shifting effects due to the presence of the second beam. This transition is centered at frequency $\nu = \nu_0$.

Let us consider now the case in which α is different from zero. The measured transition frequency for each laser beam results shifted from ν_0 by the quantity $\delta_{\nu 1}$ and $\delta_{\nu 2}$ respectively, following Eq. 5.22. The frequency distance between the two apparent transitions is

$$\delta_{\nu 1} - \delta_{\nu 2} = \frac{2\,\nu_0\, v\, \sin\alpha}{c} = 2\frac{v}{\lambda}\sin\alpha \tag{5.23}$$

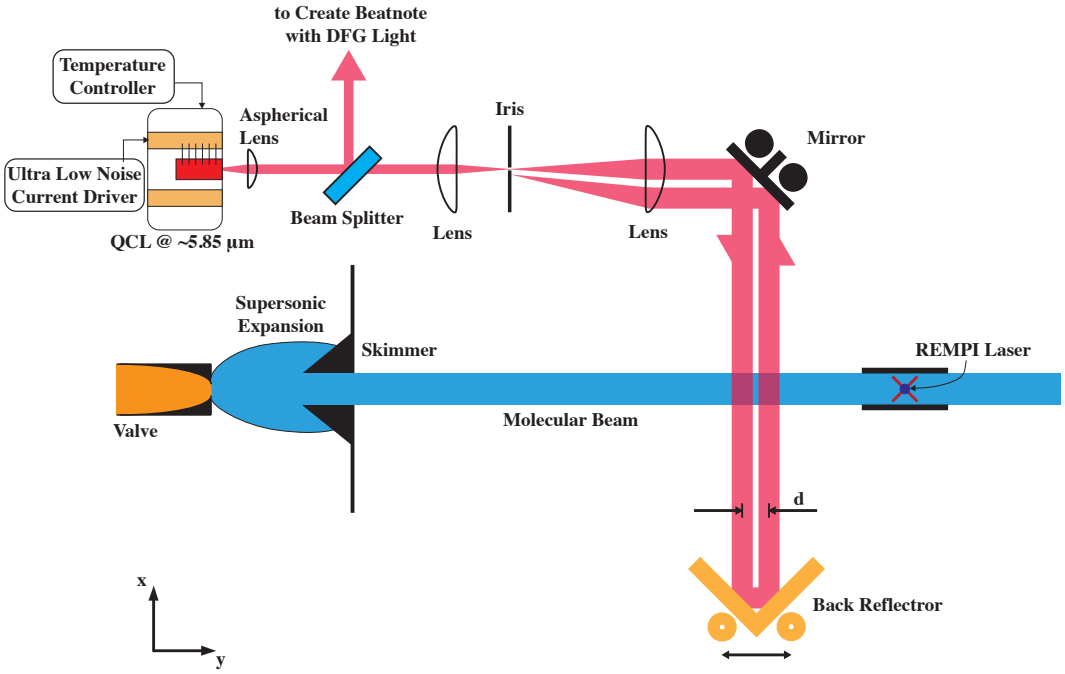

Figure 5.2: Detail of experimental apparatus used to ensure the perfect perpendicularity between mid-IR laser and molecular beam. The QCL output is collimated by means of an aspherical lens and split in two arms. One path creates the beat note with the DFG light while the other is sent to a beam expander and then towards the molecular beam. After a first interaction with molecules, the IR beam is reflected using the back-reflector. The position on the $\hat{y}$ axis of the back-reflector defines the distance d between the two antiparallel beams. The presence of a pinhole in the focus of the first lens of the Keplerian telescope prevents that the reflected beam reaches the laser source. On the right of the figure, the position of the REMPI laser is shown as a blue spot at the center of a red cross. Changing its position over the $\hat{x}$ axis allows to finely tune the angle α between the molecular and IR beams.

There are three ways to change the angle α: either moving the molecular beam or the IR laser beam or the ionization laser. The first case requires the adjustment of the valve position with respect to the skimmer, but this procedure is not very reproducible nor finely tunable. Moving the IR laser beam is much easier and can be done controlling the angle of incidence of the beam over the last mirror used to send it towards the molecular beam. However, the best choice is to move the REMPI laser. In this case it is sufficient to translate the beam spot over the $\hat{x}$ axis, i.e. the direction perpendicular to the molecular beam and parallel to the infrared laser. Since controlling a shift turns out to be easier than controlling an angle, we chose this method. In fact we can express the ionization laser position x, with respect to the beam axis, for small angles as

$$x = d \tan \alpha \approx d\alpha \tag{5.24}$$

where d is the valve-ionization laser distance, equal to 310 mm in our case.
Using Eq. 5.23 and Eq. 5.24 we can write the relation between the ionization laser position x and the distance in frequency experienced by the two antiparallel IR laser beams as

$$\delta_{\nu 1} - \delta_{\nu 2} = 2\frac{v}{\lambda} \sin \alpha = 2\frac{v}{\lambda} \frac{x}{\sqrt{d^2 + x^2}} \tag{5.25}$$

Since the two beams experience the same Doppler shift but with opposite sign, when $\delta_{\nu 1} - \delta_{\nu 2} = 0$ the ionization laser beam is in the position that makes the molecular beam perfectly perpendicular to the IR beams, i.e. $x = 0$.

Up to here, the two IR beams were assumed to be perfectly antiparallel. Now we discuss the implications of a deviation from this assumption. If the corner-cube is not perfect, an angle β is formed between first and the back-reflected beam, and the previous equation can be written as

$$\delta_{\nu 1} - \delta_{\nu 2} = \frac{v}{\lambda}[\sin \alpha - \sin(\beta - \alpha)] = \frac{v}{\lambda}[\sin \alpha(1 + \cos \beta) - \sin \beta \cos \alpha] \tag{5.26}$$

Under this condition the position x at which the two beams experience the same Doppler shift but with opposite sign is a function of the angle β as

$$x = d\frac{\sin \beta}{1 + \cos \beta} = d \tan\left(\frac{\beta}{2}\right) \tag{5.27}$$

The above formula implies that when β is not zero, it is still possible to find a position of the REMPI laser $x \neq 0$ at which the difference between the two Doppler shifts vanishes. However this does not imply $\nu = \nu_0$.

From these consideration it appears evident that the angle β has to be minimized. In order to guarantee the best parallelism between the two IR beams, the back-reflector is an aluminum, monolithic, CNC-machined piece that holds two squared mirrors. The alignment of the optics was checked and optimized by means of a HeNe collimated laser beam over a long distance to assure $\beta < 1 \cdot 10^{-4}$. Comparing the

Eq. 5.24 with Eq. 5.27 we obtain that $\alpha = \beta/2$. Thus, from Eq. 5.22, a value of $\beta = 1 \cdot 10^{-4}$ yields a shift of the order of $\nu_0 v\beta/(2c)$, that results in $\delta_\nu/\nu = 5 \cdot 10^{-11}$ for $v = 310$ m/s, as in our case.

In Fig. 5.4 the difference between the shift experienced by the two antiparallel beams $\delta_{\nu 1} - \delta_{\nu 2}$ is reported as function of the position of the REMPI laser x. Eq. 5.25 is used to fit the resulting data. The horizontal error bars are the experimental uncertainty on the positioning of the UV laser spot while the vertical ones are calculated from fit errors using the usual error propagation rules. From the data shown in Fig. 5.4 we obtain a parameter $2v/\lambda = (110.0 \pm 0.7)$ MHz, from which we extract the average molecular beam velocity $v = 320$ m/s, in good agreement with respect to the estimated velocity of the beam of 310 m/s.

5.3 External Magnetic Field Compensation

Electric and magnetic static fields induce Stark and Zeeman shifts which must be avoided. The state $a^3\Pi_1$: $|v = 0, J = 1\rangle$ of CO, for example, experiences a Stark shift of less than 100 kHz·cm/kV, for fields weaker than 200 V/cm. The external electrical fields are naturally shielded by the vacuum chamber and all voltages inside the chamber are off when the vibrational transition takes place. Magnetic shielding is much more complex and usually requires building shielding boxes of materials with very high permeability. In $v = 0$ and $v = 1$ states, the Zeeman shift determines a sub-structure of the transitions with $\Delta M = 0, \pm 1$. If we consider the transition with $\Delta M = +1$, there are two possible transitions from the state $v = 0$ to the state $v = 1$ (i.e. $M = 0 \leftarrow -1$ and $M = 1 \leftarrow 0$). These two transitions are separated by about 10 kHz/Gauss and a similar separation can be found in the other transitions with $\Delta M = 0$ and $\Delta M = -1$. If we compare the frequency of any of $\Delta M = 0$ with any of $\Delta M = \pm 1$ transitions, we find the latter to be more affected by the magnetic field with respect to the former, with a frequency shift of $\sim$500 kHz/Gauss. To actively compensate the stray fields, we use three couples of coils in quasi-Helmholtz configuration.

In the following we refer with C_{Bz} to the coil pair used to compensate the external magnetic field over the $\hat{z}$ direction, and with C_{Bx} and C_{By} to the pairs used to compensate field over the axes $\hat{x}$ and $\hat{y}$ respectively. All six coils are made by 20 windings of insulated copper wire with 0.8-mm diameter. For a rough estimate of the current required for compensation, a Hall sensor was used to measure the magnetic field B in the three orthogonal axes. Since the sensor has a linear sensitivity k, its voltage output V_{out} can be described, in the general case, as $V_{\text{out}} = V_{\text{bias}} + kB$, where V_{bias} is the output voltage when the magnetic field component perpendicular to the sensor is null. In order to get rid of the V_{bias} term, the detector was installed inside the vacuum apparatus, where the molecules interact with the infrared light, by means of a device that can rotate the sensor over 180°. If the output voltage does not change by rotating the sensor by 180° it means that the magnetic field along the

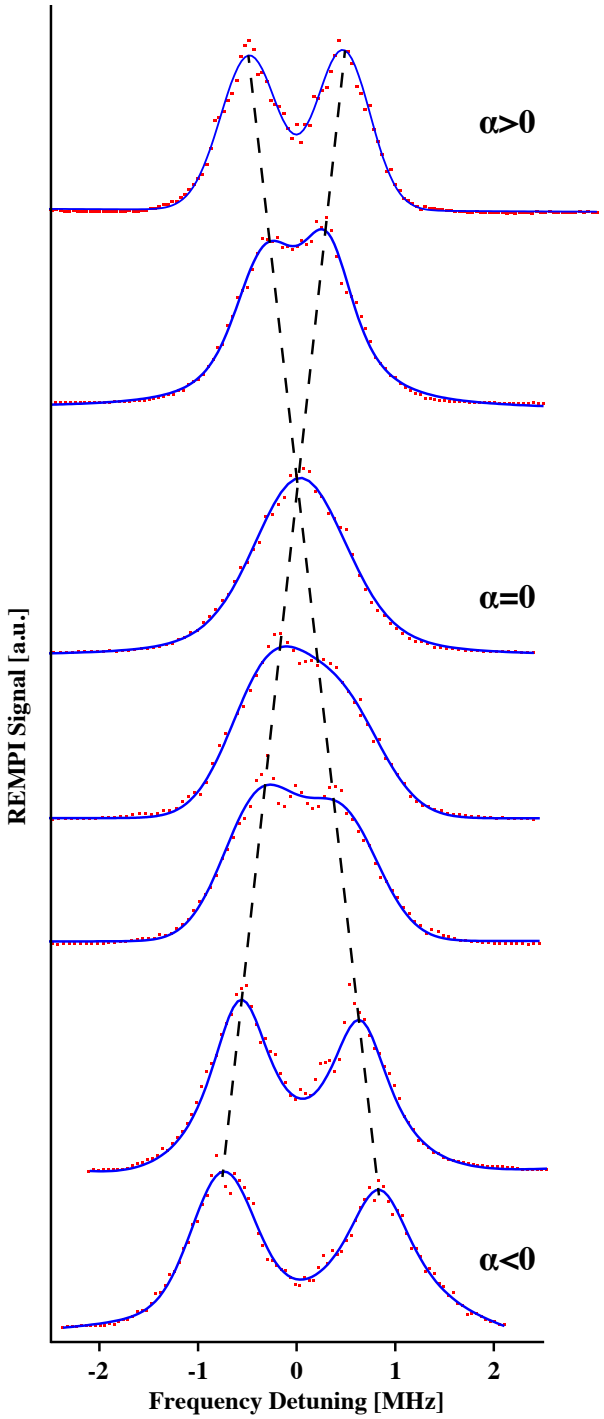

Figure 5.3: Recordings of the vibrational transition $a^3\Pi_1 : |v = 1, J = 1, -\rangle \leftarrow |v = 0, J = 1, +\rangle$ in CO, measured using both antiparallel beams. The frequency of the mid-IR laser is scanned while the REMPI signal is recorded. Each point represents the average over multiple acquisition cycles. All fitting curves are double Voigt profiles. The different graphs represent different values of the angle α: from first to last graph, the angle was moved from positive to negative sign.

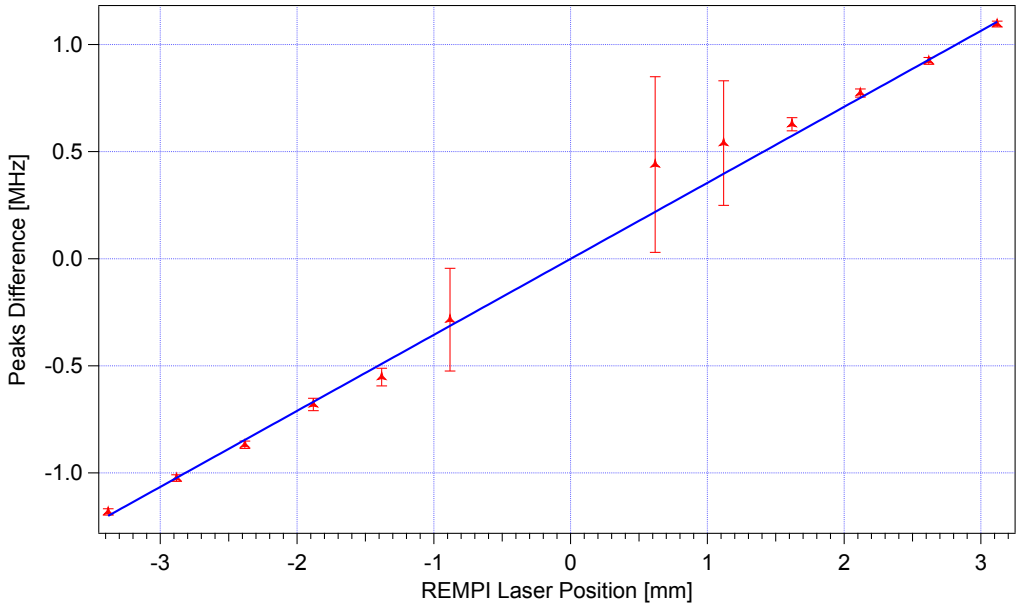

Figure 5.4: Distance in frequency between the transition induced by the two counter-propagating IR beams as function of the REMPI laser position over the $\hat{x}$ direction. A fit is performed using the function reported in Eq. 5.25 and the fit results are used to determine the position of the ionization laser to ensure the perpendicularity between mid-IR laser and molecular beams. At $x = 0$ the two peaks collapse into one.

direction perpendicular to the sensor is compensated.

Using this technique we were able to compensate the external magnetic field at a level of the sensor error. The second columns of Table 5.2 lists the measured current value of each coil that compensate the external magnetic field.

The next step for controlling the Zeeman shift exploits the different sensitivity to the magnetic field of different transitions. Since the transitions $\Delta M = \pm 1$ are more sensible to magnetic field than the $\Delta M = 0$, we used the former to compensate the field. Thus, for each direction of the magnetic field, a $\Delta M = \pm 1$ transition was chosen. Then the current of the coils is adjusted to the condition where the shift is minimized[2]. The recorded spectra are similar to what we have measured with the back-reflector in Fig. 5.3 but this time the splitting of the lines is due not to the Doppler effect but to the Zeeman spitting. In Fig. 5.5 some recorded traces are reported showing the Zeeman splitting of vibrational transition as function of current for the C_{By} coil pair that produce magnetic field over the $\hat{y}$ axis. In order to have transitions with $\Delta M = \pm 1$ the polarization of the mid-IR beam was set to be linear and parallel to the $\hat{z}$ axis. The frequency difference δ_ν^{M} between the

[2]A linearly-polarized laser drives transitions with $\Delta M = 0$ or $\Delta M = \pm 1$ if the polarization is parallel or perpendicular to the magnetic field, respectively.

Table 5.2: Currents used in the three coil pairs to compensate external magnetic fields. The second columns reports the values measured with the Hall sensors and the third one the value extracted from the Zeeman splitting of vibrational transition.

	Current [mA]	
Coils	Sensor	Molecules
C_{Bx}	180±130	205±4
C_{By}	1889±120	2120±8
C_{Bz}	644±170	646±3

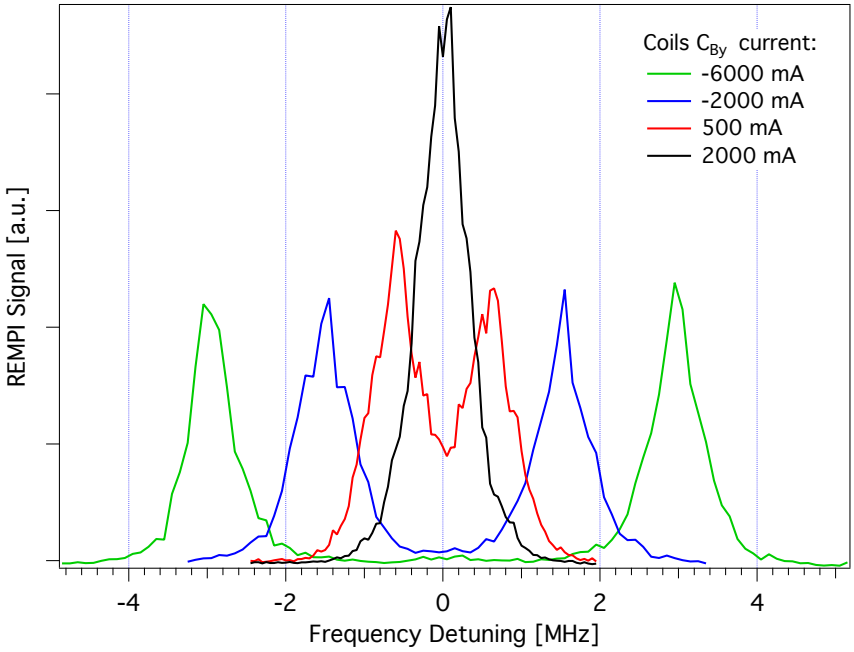

Figure 5.5: Recording of the vibrational transition $a^3\Pi_1 : |v = 1, J = 1, -\rangle \leftarrow |v = 0, J = 1, +\rangle$ in CO measured at different current applied to the coils C_{By} that produce a magnetic field over the $\hat{y}$ axis. The reported spectra are acquired using an mid-IR beam linearly polarized along the $\hat{z}$ axis. The recorded REMPI signal is reported versus the frequency of the mid-IR beam.

$\Delta M = +1$ and the $\Delta M = -1$ transitions as function of the applied current I through the coil C_{By} is shown on the second graph in Fig. 5.6. On the other two graphs the same results are shown for the coil C_{Bx} and C_{Bz} with IR beam linearly polarized over the $\hat{z}$ and $\hat{y}$ axes respectively. The ampere-meter used introduces an error on the current measurement of $\pm(1\%+3\text{dgt})$, while the error over the frequency difference δ_ν^{M} follows the propagation of the center frequency uncertainty given by the Voigt profile fit. In order to calculate the compensation current values, a linear fit of the shift δ_ν^{M} is performed over the coil current. For example, if we consider the compensation of the magnetic field over the $\hat{y}$ direction, the experimental data are fitted with the function $\delta_\nu^{\mathrm{M}} = a + bI_y$ where $a = (1553 \pm 4) \cdot 10^{-3}$ MHz and $b = (-732.2 \pm 1.0) \cdot 10^{-6}$ MHz/mA are the coefficients resulting from the fitting routine. The compensation current is calculated as $I_y^{Coil} = -a/b$ and the error is propagated. The resulting compensation current for the external field on the $\hat{y}$ axis is $I_y = (2120 \pm 8)$ mA. In Tab. 5.2 the compensation current values for the three pairs of coils are reported. Notice that the compensation values measured using the sensor and the molecules are consistent with each other except for the C_{By} case; this discrepancy can be due to a non perfect positioning of the probe with respect to the overlapping region between molecules and mid-IR radiation. The values obtained from the spectroscopic measurements were chosen to compensate external magnetic fields.

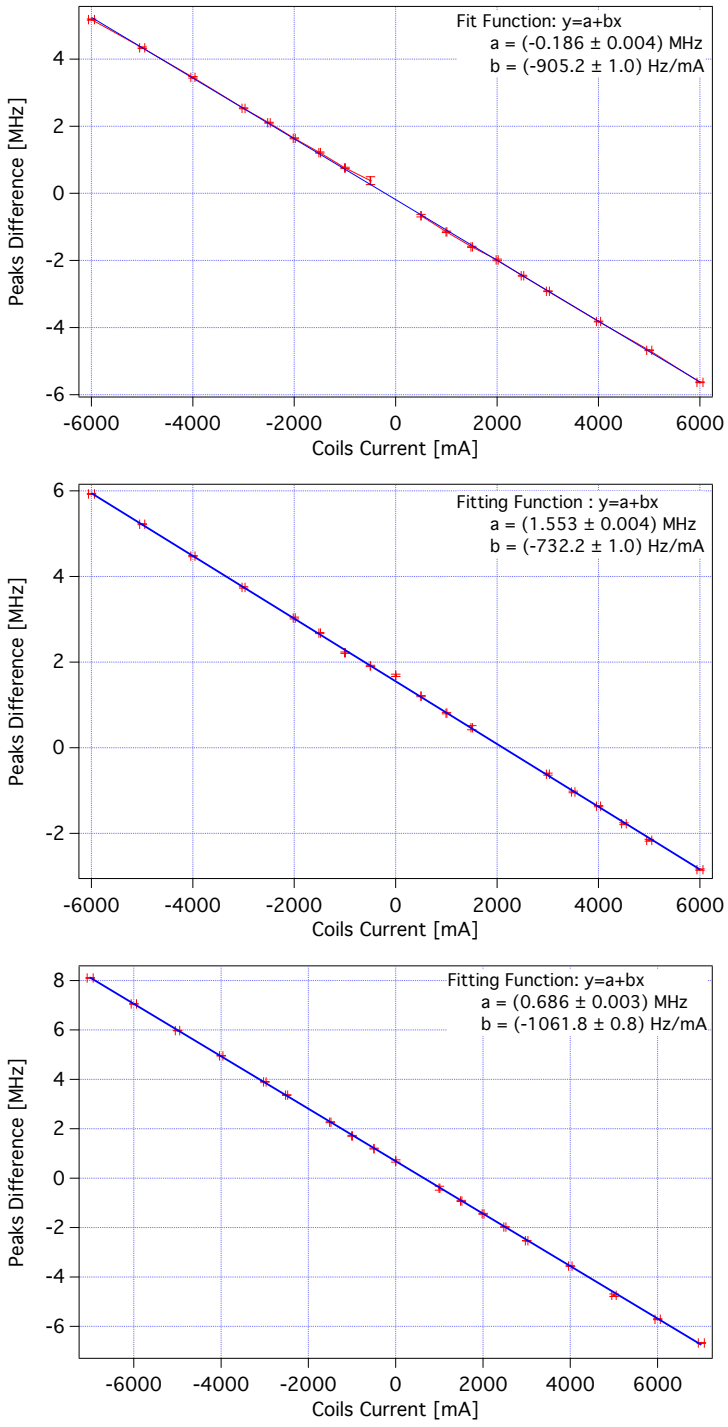

Figure 5.6: The distance in frequency δ_ν^{M} between the $\Delta M = +1$ and the $\Delta M = -1$ in the transition $a^3\Pi_1 : |v = 1, J = 1, -\rangle \leftarrow |v = 0, J = 1, +\rangle$ as function of the current I through the compensation coil pair $\mathrm{C_{Bx}}$, $\mathrm{C_{By}}$, $\mathrm{C_{Bz}}$ respectively on the top, middle and bottom graphs. The experimental data are fitted with linear function $\delta_\nu^{\mathrm{M}} = a + bI$ and the resulting coefficients value are listed on top of the corresponding plot.

5.4 kHz Resolution for Vibrational Transition at 5.83 μm

In Fig. 5.7 a typical recording of the vibrational transition is shown. The experimental data are fitted with a Voigt profile using the open source software for data analysis Minuit[3]. The parameters of the fitting routine are the transition center, the Gaussian and Lorentzian contributions to the line width and their errors. For each fit, particular attention is paid on the residuals as previously explained. Only measurements with symmetric residuals with respect to the transition central frequency are processed and taken into account for the final determination of the transition frequency.

The residual Zeeman splitting and Doppler broadening due to the non perfect alignment of the REMPI beam are taken into consideration by the fitting routine, whereas the offset due to $\beta \neq 0$ will be treated later.

The central frequency of the transition extracted from the fit is reported as a single point in the plot shown in Fig. 5.8. The relative error bar correspond to the standard deviation provided by the fitting routine over the frequency center. In order to determine the accuracy on the measurement of the frequency center value, several measurements have been performed and are reported in the same graph. The distribution of points is scattered around the average value that is shown as a blue line. The average value is (51399115446.9 ± 1.7) kHz, where the error is the standard deviation of the mean. The different measurements are not consistent with each other: this means that the error provided by the fitting routine over a single measurement is much lower than some kind of slow variation effects that result in a spread of the measured vibrational frequencies. One source of this effect is the slow variation of the energy and the frequency of the 206 nm radiation mainly generated by the frequency doubled Nd:YAG pulsed laser used to pump the OPO system. Since this radiation is used to prepare the molecules in the $a^3\Pi_1$ state, where the vibrational transitions starts, a power variation results in a variation of the number of molecules that are excited and consequently revealed. These power instabilities can slightly change the shape of the acquired line profile, that can be interpreted by the fitting routine as a small shift of the transition frequency center. A similar contribution comes also from the frequency fluctuations of the same 206 nm source. As described in the Chapter 4, the frequency of the pulsed 532 nm laser is long term stabilized on a temperature controlled iodine cell. Nonetheless, residual frequency fluctuations, of the order of 30-50 MHz, can alter the efficiency of the excitation process. To prove this contribution, we have noticed that when the frequency of the 532 nm light clearly drifts, the fitting routines provide a line central frequency shifted by more than 30 kHz from the average value. When no visible frequency drift is noticed and the fitting residuals are considered symmetric, the values is used for the estimation of the final transition frequency.

[3]https://seal.web.cern.ch/seal/snapshot/work-packages/mathlibs/minuit

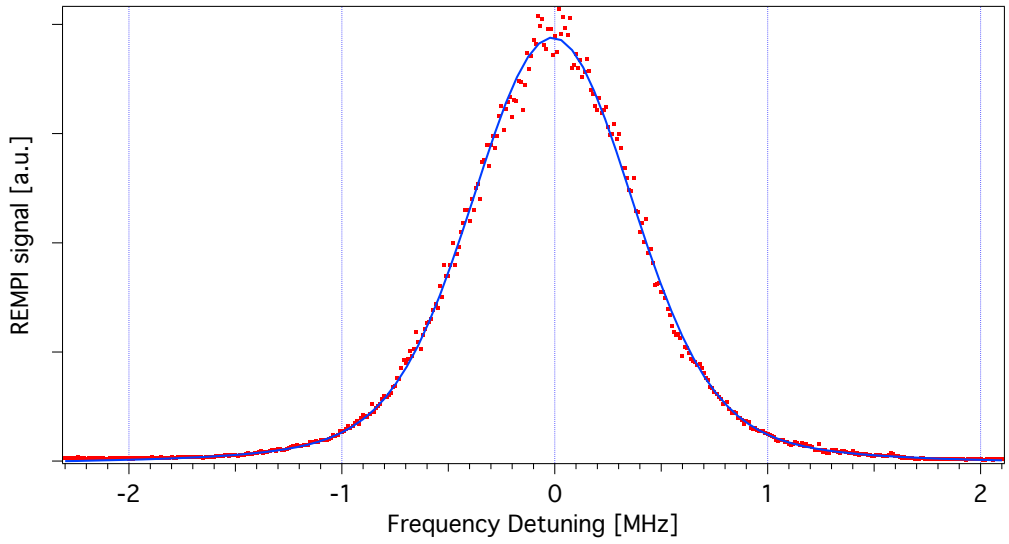

Figure 5.7: Transition $a^3\Pi_1 : |v = 1, J = 1, -\rangle \leftarrow |v = 0, J = 1, +\rangle$ as function of the infrared laser detuning. The experimental data (dots) are fitted with a Voigt profile (solid line).

About the residual Doppler shift, we have measured the angle β to be less than $1 \cdot 10^{-4}$ that results in a maximum Doppler shift of 2.6 kHz, derived by the Eq. 5.22, in which we have used $v = 310$ m/s and $\alpha = \beta/2$. Considering this additional error contribution, our best estimation for the vibrational transition $a^3\Pi_1 : |v = 1, J = 1, -\rangle \leftarrow |v = 0, J = 1, +\rangle$ is

$$a^3\Pi_1 : |v = 1, J = 1, -\rangle \leftarrow |v = 0, J = 1, +\rangle = (51399115447 \pm 3) \text{ kHz} \qquad (5.28)$$

The relative accuracy of our measurements is $6 \cdot 10^{-11}$, more than four order of magnitude better than the most accurate value reported to date in literature of (51399.15±0.09) GHz [105].

This setup is able to measure vibrational transitions in the mid-IR with a precision of the order of the tens of kHz, in only a few minutes. The quality of the measurements can then be refined by subsequent averaging, to the level of 3 kHz. This is possible thanks to the transverse molecular beam excitation that strongly reduce the Doppler broadening. The availability of a mid-IR source referenced to the primary standard ensures the possibility to precisely address the transition.

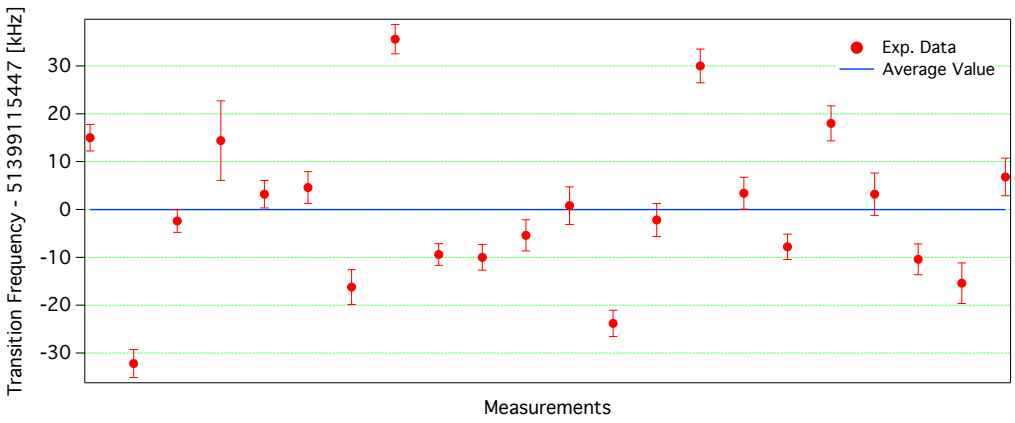

Figure 5.8: Central frequency of the transition $a^3\Pi_1 : |v = 1, J = 1, -\rangle \leftarrow |v = 0, J = 1, +\rangle$ measured during different experimental cycles distributed over one month. The error bars are referenced to the standard deviation on the central peak frequency determination provided by the fitting routine. The blue solid line is the average value of all the reported measurements. The standard deviation of the reported points is 7.9 kHz around its average value of 51399115447 kHz, and the standard deviation of the mean is 1.7 kHz.

Conclusion

It has been shown in this thesis how to obtain a laser source in the mid-IR with mW power that is remotely referenced to the primary frequency standard. This radiation has been used in a high-resolution spectroscopy experiment on a molecular beam to measure the vibrational transition $|v = 1, J = 1, -\rangle \leftarrow |v = 0, J = 1, +\rangle$ in the $a^3\Pi_1$ excited state of carbon monoxide with an accuracy of the order of parts in 10^{11}. This measurement is more than four orders of magnitude more accurate than the best value reported in literature to date [105].

The setup is very versatile: the investigation of other transitions can be performed with minor changes. DFG radiation between about 1620 and 1720 cm^{-1} can be produced simply by changing the crystal temperature and the signal laser frequency. The 1–10 μm range can be covered using GaP crystals with different patterns. Since only a minimal part of the QCL power is used for its frequency stabilization, almost the whole QCL power can thus be employed on the spectroscopic experiment.

The main limitation in the accuracy and precision is due to the Doppler effect, affecting both line broadening and frequency shifts. In order to overcome this limit, we are planning to develop an intrinsic Doppler-free measurement based on a two-photon absorption spectroscopy. The line width will then be limited by transit time broadening that can be reduced by decelerating the molecules.

Bibliography

[1] T. L. Nicholson, S. L. Campbell, R. B. Hutson, G. E. Marti, B. J. Bloom, R. L. McNally, W. Zhang, M. D. Barrett, M. S. Safronova, G. F. Strouse, W. L. Tew, and J. Ye, "Systematic evaluation of an atomic clock at $2 \cdot 10^{-18}$ total uncertainty," *Nature Comm.*, vol. 6, p. 6896, 2015.

[2] B. Darquié, C. Stoeffler, A. Shelkovnikov, C. Daussy, A. Amy-Klein, C. Chardonnet, S. Zrig, L. Guy, J. Crassous, P. Soulard, P. Asselin, T. R. Huet, P. Schwerdtfeger, R. Bast, and T. Saue, "Progress toward the first observation of parity violation in chiral molecules by high-resolution laser spectroscopy," *Chirality*, vol. 22, p. 870, 2010.

[3] J. J. Hudson, D. M. Kara, I. J. Smallman, B. E. Sauer, M. R. Tarbutt, and E. A. Hinds, "Improved measurement of the shape of the electron," *Nature*, vol. 473, p. 493, 2011.

[4] T. A. Collaboration, J. Baron, W. C. Campbell, D. DeMille, J. M. Doyle, G. Gabrielse, Y. V. Gurevich, P. W. Hess, N. R. Hutzler, E. Kirilov, I. Kozyryev, B. R. O'Leary, C. D. Panda, M. F. Parsons, E. S. Petrik, B. Spaun, A. C. Vutha, and A. D. West, "Order of magnitude smaller limit on the electric dipole moment of the electron," *Science*, vol. 343, p. 6168, 2013.

[5] A. Shelkovnikov, R. J. Butcher, C. Chardonnet, and A. Amy-Klein, "Stability of the proton-to-electron mass ratio," *Phys. Rev. Lett.*, vol. 100, p. 150801, 2008.

[6] J. Bagdonaite, W. Ubachs, M. T. Murphy, and J. B. Whitmore, "Constraint on a varying proton-electron mass ratio 1.5 billion years after the big bang," *Phys. Rev. Lett.*, vol. 114, p. 071301, 2015.

[7] S. A. Levshakov, M. G. Kozlov, and D. Reimers, "Methanol as a tracer of fundamental constants," *Astrophys. J.*, vol. 738, p. 26, 2011.

[8] S. A. Levshakov, P. Molaro, A. V. Lapinov, D. Reimers, C. Henkel, and T. Sakai, "Searching for chameleon-like scalar fields with the ammonia method," *Astron. Astrophys.*, vol. 512, p. A44, 2010.

[9] P. J. Mohr, D. B. Newell, and B. N. Taylor, "Codata recommended values of the fundamental physical constants: 2014," *Rev. Mod. Phys.*, vol. 88, p. 035009, 2016.

[10] S. Perlmutter, "Nobel lecture: Measuring the acceleration of the cosmic expansion using supernovae," *Rev. Mod. Phys.*, vol. 84, p. 1127, 2012.

[11] B. P. Schmidt, "Nobel lecture: Accelerating expansion of the universe through observations of distant supernovae," *Rev. Mod. Phys.*, vol. 84, p. 1151, 2012.

[12] A. G. Riess, "Nobel lecture: My path to the accelerating universe," *Rev. Mod. Phys.*, vol. 84, p. 1165, 2012.

[13] B. Ratra and P. J. E. Peebles, "Cosmological consequences of a rolling homogeneous scalar field," *Phys. Rev. D*, vol. 37, p. 3406, 1988.

[14] J. Bagdonaite, P. Jansen, C. Henkel, H. L. Bethlem, K. M. Menten, and W. Ubachs, "A stringent limit on a drifting proton-to-electron mass ratio from alcohol in the early universe," *Science*, vol. 339, p. 46, 2013.

[15] J. Crassous, C. Chardonnet, T. Saue, and P. Schwerdtfeger, "Recent experimental and theoretical developments towards the observation of parity violation (PV) effects in molecules by spectroscopy," *Org. Biomol. Chem.*, vol. 3, p. 2218, 2005.

[16] D. W. Rein, "Some remarks on parity violating effects of intramolecular interactions," *J. Mol. Evol.*, vol. 4, p. 15, 1974.

[17] V. Letokhov, "On difference of energy levels of left and right molecules due to weak interactions," *Phys. Lett. A*, vol. 53, p. 275, 1975.

[18] M. Ziskind, C. Daussy, T. Marrel, and C. Chardonnet, "Improved sensitivity in the search for a parity-violating energy difference in the vibrational spectrum of the enantiomers of CHFClBr," *Eur. Phys. J. D*, vol. 20, p. 219, 2002.

[19] M. Quack and J. Stohner, "Combined multidimensional anharmonic and parity violating effects in CDBrClF," *J. Chem. Phys.*, vol. 119, p. 11228, 2003.

[20] P. Schwerdtfeger, T. Saue, J. N. P. van Stralen, and L. Visscher, "Relativistic second-order many-body and density-functional theory for the parity-violation contribution to the C–F stretching mode in CHFClBr," *Phys. Rev. A*, vol. 71, p. 012103, Jan 2005.

[21] L. I. Schiff, "Measurability of nuclear electric dipole moments," *Phys. Rev.*, vol. 132, p. 2194, 1963.

[22] M. Pospelov and A. Ritz, "Electric dipole moments as probes of new physics," *Ann. Phys.*, vol. 318, p. 119, 2005.

[23] F. Hoogeveen, "The standard model prediction for the electric dipole moment of the electron," *Nucl. Phys. B*, vol. 341, p. 322, 1990.

[24] J. L. Flowers and B. W. Petley, "Progress in our knowledge of the fundamental constants of physics," *Rep. Prog. Phys.*, vol. 64, p. 1191, 2001.

[25] M. de Podesta, R. Underwood, G. Sutton, P. Morantz, P. Harris, D. F. Mark, F. M. Stuart, G. Vargha, and G. Machin, "A low-uncertainty measurement of the Boltzmann constant," *Metrologia*, vol. 50, p. 354, 2013.

[26] L. Moretti, A. Castrillo, E. Fasci, M. D. D. Vizia, G. Casa, G. Galzerano, A. Merlone, P. Laporta, and L. Gianfrani, "Determination of the Boltzmann constant by means of precision measurements of $H_2^{18}O$ line shapes at 1.39μm," *Phys. Rev. Lett.*, vol. 111, p. 060803, 2013.

[27] R. Maulini, I. Dunayevskiy, A. Lyakh, A. Tsekoun, C. Patel, L. Diehl, C. Pflügl, and F. Capasso, "Widely tunable high-power external cavity quantum cascade laser operating in continuous-wave at room temperature," *Electronic Letters*, vol. 45, p. 107, 2009.

[28] Q. Y. Lu, Y. Bai, N. Bandyopadhyay, S. Slivken, and M. Razeghi, "2.4 W room temperature continuous wave operation of distributed feedback quantum cascade lasers," *Appl. Phys. Lett.*, vol. 98, p. 181106, 2011.

[29] S. Borri, S. Bartalini, P. Cancio, I. Galli, G. Giusfredi, D. Mazzotti, M. Yamanishi, and P. D. Natale, "Frequency-noise dynamics of mid-infrared quantum cascade lasers," *IEEE J. Quant. Elec.*, vol. 47, p. 984, 2011.

[30] S. Bartalini, S. Borri, P. Cancio, A. Castrillo, I. Galli, G. Giusfredi, D. Mazzotti, L. Gianfrani, and P. D. Natale, "Observing the intrinsic linewidth of a quantum-cascade laser: Beyond the Schawlow-Townes limit," *Phys. Rev. Lett.*, vol. 104, p. 083904, 2010.

[31] S. Bartalini, S. Borri, I. Galli, G. Giusfredi, D. Mazzotti, T. Edamura, N. Akikusa, M. Yamanishi, and P. D. Natale, "Measuring frequency noise and intrinsic linewidth of a room-temperature DFB quantum cascade laser," *Opt. Express*, vol. 19, p. 17996, 2011.

[32] F. Cappelli, I. Galli, S. Borri, G. Giusfredi, P. Cancio, D. Mazzotti, A. Montori, N. Akikusa, M. Yamanishi, S. Bartalini, and P. D. Natale, "Subkilohertz linewidth room-temperature mid-infrared quantum cascade laser using

a molecular sub-Doppler reference," *Opt. Lett.*, vol. 37, no. 23, pp. 4811–4813, 2012.

[33] M. S. Taubman, T. L. Myers, B. D. Cannon, R. M. Williams, F. Capasso, C. Gmachl, D. L. Sivco, and A. Y. Cho, "Frequency stabilization of quantum-cascade lasers by use of optical cavities," *Opt. Lett.*, vol. 27, p. 2164, 2002.

[34] E. Fasci, N. Coluccelli, M. Cassinerio, A. Gambetta, L. Hilico, L. Gianfrani, P. Laporta, A. Castrillo, and G. Galzerano, "Narrow-linewidth quantum cascade laser at 8.6 μm," *Opt. Lett.*, vol. 39, p. 4946, 2014.

[35] M. G. Hansen, E. Magoulakis, Q.-F. Chen, I. Ernsting, and S. Schiller, "Quantum cascade laser-based mid-IR frequency metrology system with ultra-narrow linewidth and $1{\cdot}10^{-13}$-level frequency instability," *Opt. Lett.*, vol. 40, p. 2289, 2015.

[36] M. S. de Cumis, S. Borri, G. Insero, I. Galli, A. Savchenkov, D. Eliyahu, V. Ilchenko, N. Akikusa, A. Matsko, L. Maleki, and P. D. Natale, "Microcavity-stabilized quantum cascade laser," *Laser Photonics Rev.*, vol. 10, no. 1, p. 153, 2016.

[37] P. L. T. Sow, S. Mejri, S. K. Tokunaga, O. Lopez, A. Goncharov, B. Argence, C. Chardonnet, A. Amy-Klein, C. Daussy, and B. Darquié, "A widely tunable 10-μm quantum cascade laser phase-locked to a state-of-the-art mid-infrared reference for precision molecular spectroscopy," *Appl. Phys. Lett.*, vol. 104, p. 264101, 2014.

[38] D. Mazzotti, P. Cancio, G. Giusfredi, P. D. Natale, and M. Prevedelli, "Frequency-comb-based absolute frequency measurements in the mid-infrared with a difference-frequency spectrometer," *Opt. Lett.*, vol. 30, p. 997, 2005.

[39] U. Bressel, I. Ernsting, and S. Schiller, "5 μm laser source for frequency metrology based on difference frequency generation," *Opt. Lett.*, vol. 37, p. 918, 2012.

[40] M. Niering, R. Holzwarth, J. Reichert, P. Pokasov, T. Udem, M. Weitz, T. Hänsch, P. Lemonde, G. Santarelli, M. Abgrall, P. Laurent, C. Salomon, and A. Clairon, "Measurement of the hydrogen $1s$-$2s$ transition frequency by phase coherent comparison with a microwave cesium fountain clock," *Phys. Rev. Lett.*, vol. 84, p. 5496, 2000.

[41] S. Borri, M. S. de Cumis, G. Insero, S. Bartalini, P. C. Pastor, D. Mazzotti, I. Galli, G. Giusfredi, G. Santambrogio, A. Savchenkov, D. Eliyahu, V. Ilchenko, N. Akikusa, A. Matsko, L. Maleki, and P. D. Natale, "Tunable microcavity-stabilized quantum cascade laser for Mid-IR high-resolution spectroscopy and sensing," *Sensors*, vol. 16, no. 2, p. 238, 2016.

[42] G. Shekhar and P. G. Leonel, *Laser Beam Propagation in Nonlinear Optical Media*. CRC Press, 2016/11/26 2013.

[43] G. D. Boyd, A. Ashkin, J. M. Dziedzic, and D. A. Kleinman, "Second-harmonic generation of light with double refraction," *Phys. Rev.*, vol. 137, no. 4A, p. A1305, 1965.

[44] D. A. Kleinman, "Theory of second harmonic generation of light," *Phys. Rev.*, vol. 128, no. 4, p. 1761, 1962.

[45] D. A. Kleinman, "Second-harmonic generation of light by focused laser beams," *Physical Review*, vol. 145, no. 1, p. 338, 1966.

[46] P. Canarelli, Z. Benko, R. Curl, and F. K. Tittel, "Continuous-wave infrared laser spectrometer based on difference frequency generation in $AgGaS_2$ for high-resolution spectroscopy," *J. Opt. Soc. Am. B*, vol. 9, no. 2, p. 197, 1992.

[47] T.-B. Chu, R. Fischer, and A. J. Bouvier, "c.w.-intracavity difference frequency generation (I.D.F.G.) by non-collinear mixing of three waves in two laser resonators," *J. Phys. France*, vol. 46, p. 2083, 1985.

[48] J.-J. Zondy, "The effects of focusing in type-I and type-II difference-frequency generations," *Optics Comm.*, vol. 149, p. 181, 1998.

[49] V. G. Dmitriev, G. G. Gurzadyan, and D. N. Nikogosyan, *Handbook of nonlinear optical crystals*. Springer-Verlag Berlin Heidelberg, 1999.

[50] I. Galli, S. Bartalini, P. Cancio, G. Giusfredi, D. Mazzotti, and P. D. Natale, "Ultra-stable, widely tunable and absolutely linked mid-IR coherent source," *Opt. Express*, vol. 17, no. 12, p. 9582, 2009.

[51] I. Ricciardi, E. D. Tommasi, P. Maddaloni, S. Mosca, A. Rocco, J.-J. Zondy, M. D. Rosa, and P. D. Natale, "Frequency-comb-referenced singly-resonant OPO for sub-Doppler spectroscopy," *Opt. Express*, vol. 20, no. 8, p. 9178, 2012.

[52] L. Wang, Z. Cao, H. Wang, H. Zhao, W. Gao, Y. Yuan, W. Chen, W. Zhang, Y. Wang, and X. Gao, "A widely tunable (5-12.5 μm) continuous-wave mid-infrared laser spectrometer based on difference frequency generation in $AgGaS_2$," *Optics Comm.*, vol. 284, no. 1, p. 358, 2011.

[53] V. Tassev, M. Snure, R. Peterson, K. L. Schepler, R. Bedford, M. Mann, S. Vangala, W. Goodhue, A. Lin, J. Harris, M. Fejer, and P. Schunemann, "Progress in orientation-patterned GaP for next-generation nonlinear optical devices," *Proc. SPIE*, vol. 8604, p. 86040V, 2013.

[54] P. G. Schunemann, L. A. Pomeranz, and D. J. Magarrell, "Optical parametric oscillation in quasi-phase-matched GaP," *Proc. SPIE*, vol. 9347, 2015.

[55] M. G. Hansen, I. Ernsting, S. V. Vasilyev, A. Grisard, E. Lallier, B. Gérard, and S. Schiller, "Robust, frequency-stable and accurate mid-IR laser spectrometer based on frequency comb metrology of quantum cascade lasers upconverted in orientation-patterned GaAs," *Opt. Express*, vol. 21, no. 22, p. 27043, 2013.

[56] K. Devi, P. G. Schunemann, and M. Ebrahim-Zadeh, "Continuous-wave, multimilliwatt, mid-infrared source tunable across 6.4-7.5 μm based on orientation-patterned GaAs," *Opt. Lett.*, vol. 39, no. 23, p. 6751, 2014.

[57] O. Levi, T. J. Pinguet, T. Skauli, L. A. Eyres, K. R. Parameswaran, J. S. Harris, M. M. Fejer, T. J. Kulp, S. E. Bisson, B. Gerard, E. Lallier, and L. Becouarn, "Difference frequency generation of 8-μm radiation in orientation-patterned GaAs," *Opt. Lett.*, vol. 27, p. 2091, 2002.

[58] S. Vasilyev, S. Schiller, A. Nevsky, A. Grisard, D. Faye, E. Lallier, Z. Zhang, A. J. Boyland, J. K. Sahu, M. Ibsen, and W. A. Clarkson, "Broadly tunable single-frequency cw mid-infrared source with milliwatt-level output based on difference-frequency generation in orientation-patterned GaAs," *Opt. Lett.*, vol. 33, no. 13, p. 1413, 2008.

[59] L. A. Pomeranz, P. G. Schunemann, D. J. Magarrell, J. C. McCarthy, K. T. Zawilski, and D. E. Zelmon, "1–μm–pumped OPO based on orientation–patterned GaP," *Proc. SPIE*, vol. 9347, p. 93470K, 2015.

[60] S. Guha, J. O. Barnes, and P. G. Schunemann, "Mid-wave infrared generation by difference frequency mixing of continuous wave lasers in orientation-patterned Gallium Phosphide," *Opt. Mater. Express*, vol. 5, no. 12, p. 2911, 2015.

[61] P. Deus, U. Voland, and H. A. Schneider, "Thermal expansion of GaP within 20 to 300 K," *Physica Status Solidi (a)*, vol. 80, no. 1, p. K29, 1983.

[62] G. Insero, C. Clivati, D. D'Ambrosio, P. D. Natale, G. Santambrogio, P. G. Schunemann, J.-J. Zondy, and S. Borri, "Difference frequency generation in the mid-infrared with orientation-patterned gallium phosphide crystals," *Opt. Lett.*, vol. 41, no. 21, p. 5114, 2016.

[63] T. Matsushita, T. Yamamoto, and T. Kondo, "Epitaxial growth of spatially inverted gap for quasi phase matched nonlinear optical devices," *Jap. J. App. Phys.*, vol. 46, p. 17, 2007.

[64] J. Lee, J. Salzman, D. Emerson, J. R. Shealy, and J. M. Ballantyne, "Selective area growth of GaP on Si by MOCVD," *J. Cryst. Gr.*, vol. 172, p. 53, 1997.

[65] J.-J. Zondy, D. Touahri, and O. Acef, "Absolute value of the d36 nonlinear coefficient of $AgGaS_2$: prospect for a low-threshold doubly resonant oscillator-based 3:1 frequency divider," *J. Opt. Soc. Am. B*, vol. 14, no. 10, p. 2481, 1997.

[66] P. S. Kuo, *Thick film, orientation–patterned Gallium Arsenide for nonlinear optical frequency conversion*. PhD thesis, Standford University, 2008.

[67] Z. H. Levine, "Optical second-harmonic susceptibilities: Frequency-dependent formulation with results for GaP and GaAs," *Phys. Rev. B*, vol. 49, no. 7, p. 4532, 1994.

[68] I. Shoji, T. Kondo, A. Kitamoto, M. Shirane, and R. Ito, "Absolute scale of second-order nonlinear-optical coefficients," *J. Opt. Soc. Am. B*, vol. 14, no. 9, p. 2268, 1997.

[69] G. Boyd, H. Kasper, and J. McFee, "Linear and nonlinear optical properties of $AgGaS_2$, $CuGaS_2$, and $CuInS_2$, and theory of the wedge technique for the measurement of nonlinear coefficients," *IEEE J. Quantum Electron.*, vol. 7, no. 12, p. 563, 1971.

[70] J. J. WYNNE and N. BLOEMBERGEN, "Measurement of the lowest-order nonlinear susceptibility in III-V semiconductors by Second-Harmonic Generation with a CO_2 laser," *Phys. Rev.*, vol. 188, p. 1211, 1969.

[71] R. C. Miller, "Optical second harmonic generation in piezoelectric crystals," *Appl. Phys. Lett.*, vol. 5, p. 17, 1964.

[72] I. Galli, M. S. de Cumis, F. Cappelli, S. Bartalini, D. Mazzotti, S. Borri, A. Montori, N. Akikusa, M. Yamanishi, G. Giusfredi, P. Cancio, and P. D. Natale, "Comb-assisted subkilohertz linewidth quantum cascade laser for high-precision mid-infrared spectroscopy," *Appl. Phys. Lett.*, vol. 102, no. 12, 2013.

[73] A. Schliesser, N. Picque, and T. W. Hänsch, "Mid-infrared frequency combs," *Nat. Phot.*, vol. 6, no. 7, p. 440, 2012.

[74] F. Keilmann, C. Gohle, and R. Holzwarth, "Time-domain mid-infrared frequency-comb spectrometer," *Opt. Lett.*, vol. 29, no. 13, pp. 1542–1544, 2004.

[75] A. A. Savchenkov, A. B. Matsko, D. Strekalov, M. Mohageg, V. S. Ilchenko, and L. Maleki, "Low threshold optical oscillations in a whispering gallery mode CaF_2 resonator," *Phys. Rev. Lett.*, vol. 93, p. 243905, 2004.

[76] P. Del'Haye, A. Schliesser, O. Arcizet, T. Wilken, R. Holzwarth, and T. J. Kippenberg, "Optical frequency comb generation from a monolithic microresonator," *Nature*, vol. 450, no. 7173, p. 1214, 2007.

[77] C. Clivati, G. Cappellini, L. F. Livi, F. Poggiali, M. S. de Cumis, M. Mancini, G. Pagano, M. Frittelli, A. M., G. A. Costanzo, F. Levi, D. Calonico, L. Fallani, J. Catani, and M. Inguscio, "Measuring absolute frequencies beyond the GPS limit via long-haul optical frequency dissemination," *Opt. Express*, vol. 24, no. 11, pp. 11865–11875, 2016.

[78] D. Calonico, E. K. Bertacco, C. E. Calosso, C. Clivati, G. A. Costanzo, M. Frittelli, A. Godone, A. Mura, N. Poli, D. V. Sutyrin, G. Tino, M. E. Zucco, and F. Levi, "High-accuracy coherent optical frequency transfer over a doubled 642-km fiber link," *Appl. Phys. B*, vol. 117, no. 3, p. 979, 2014.

[79] L.-S. Ma, P. Jungner, J. Ye, and J. L. Hall, "Delivering the same optical frequency at two places: accuratecancellation of phase noise introduced by an optical fiber or other time-varyingpath," *Opt. Lett.*, vol. 19, no. 21, pp. 1777–1779, 1994.

[80] P. A. Williams, W. C. Swann, and N. R. Newbury, "High-stability transfer of an optical frequency over long fiber-optic links," *J. Opt. Soc. Am. B*, vol. 25, no. 8, pp. 1284–1293, 2008.

[81] C. Clivati, "Private communications." INRIM data, 2016.

[82] H. Telle, B. Lipphardt, and J. Stenger, "Kerr-lens, mode-locked lasers as transfer oscillators for optical frequency measurements," *Appl. Phys. B*, vol. 74, no. 1, p. 1, 2002.

[83] E. Rubiola, *Phase Noise and Frequency Stability in Oscillators.* The Cambridge RF and Microwave Engineering Series, Cambridge University Press, 2010.

[84] H. L. Bethlem and W. Ubachs, "Testing the time-invariance of fundamental constants using microwave spectroscopy on cold diatomic radicals," *Faraday Discuss.*, vol. 142, p. 25, 2009.

[85] E. J. Salumbides, M. L. Niu, J. Bagdonaite, N. de Oliveira, D. Joyeux, L. Nahon, and W. Ubachs, "CO $A - X$ system for constraining cosmological drift of the proton-electron mass ratio," *Phys. Rev. A*, vol. 86, p. 022510, 2012.

[86] A. J. de Nijs, E. J. Salumbides, K. S. E. Eikema, W. Ubachs, and H. L. Bethlem, "UV-frequency metrology on CO ($a^3\Pi$): Isotope effects and sensitivity to a variation of the proton-to-electron mass ratio," *Phys. Rev. A*, vol. 84, p. 052509, 2011.

[87] S. Y. T. van der Meerakker, H. L. Bethlem, N. Vanhaecke, and G. Meijer, "Manipulation and control of molecular beams," *Chem. Rev.*, vol. 112, p. 4828, 2012.

[88] C. A. Burrus, "Stark effect from 1.1 to 2.6 millimeters wavelength : PH_3, PD_3, DI, and CO," *J. Chem. Phys.*, vol. 28, p. 427, 1958.

[89] W. L. Lorgensen and L. Salem, *The Organic Chemist's Book of Orbitals*. Academic Press, 1973.

[90] B. G. Wicke, R. W. Field, and W. Klemperer, "Fine structure, dipole moment, and perturbation analysis of $a^3\Pi$ CO," *J. Chem. Phys.*, vol. 56, p. 5758, 1972.

[91] J. J. Gilijamse, S. Hoekstra, S. A. Meek, M. Metsälä, S. Y. T. van de Meerakker, G. Meijer, and G. C. Groenenboom, "The radiative lifetime of metastable CO ($a^3\Pi$, $v = 0$)," *J. Chem. Phys.*, vol. 127, p. 221102, 2007.

[92] H. Lefebvre-Brion and R. W. Field, *The Spectra and Dynamics of Diatomic Molecules*. Elsevier Academic Press, 2004.

[93] J. M. Brown and A. Carrington, *Rotational Spectroscopy of Diatomic Molecules*. Cambridge University Press, 2003.

[94] S. A. Meek, *A Stark Decelerator on a Chip*. PhD thesis, Freie Universität Berlin, 2010.

[95] G. Herzberg, *Molecular Spectra and Molecular Structure: Spectra of Diatomic Molecules*, vol. 1. Krieger Publishing Company, 1989.

[96] J. M. Brown, E. A. Colbourn, K. Watson, and F. Wayne, "An effective hamiltonian for diatomic molecules: Ab initio calculations of parameters of HCl+," *J. Mol. Spectr.*, p. 294, 1979.

[97] F. Hund, "Zur Deutung einiger Erscheinungen in den Molekelspektren," *Zeitschrift für Physik*, vol. 36, pp. 657–674, 1926.

[98] C. L. Pekeris, "The rotation-vibration coupling in diatomic molecules," *Phys. Rev.*, vol. 45, p. 98, 1934.

[99] J. L. Dunham, "The energy levels of a rotating vibrator," *Phys. Rev.*, vol. 41, pp. 721–731, 1932.

[100] S. Yamamoto and S. Saito, "The microwave spectra of CO in the electronically excited states ($a^3\Pi_r$ and $a'^3\Sigma^+$)," *J. Chem. Phys.*, vol. 89, p. 1936, 1988.

[101] N. Carballo, H. E. Warner, C. S. Gudeman, and R. C. Woods, "The microwave spectrum of CO in the $a^3\Pi$ state. II. the submillimeter wave transitions in the normal isotope," *J. Chem. Phys.*, vol. 88, p. 7273, 1988.

[102] A. Wada and H. Kanamori, "Submillimeter-wave spectroscopy of CO in the $a^3\Pi$ state," *J. Mol. Spectr.*, vol. 200, p. 196, 2000.

[103] R. J. Saykally, K. M. Evenson, E. R. Comben, and J. M. Brown, "Measurement of the rotational spectrum of carbon monoxide in its metastable $a^3\Pi$ state by laser magnetic resonance," *Mol. Phys.*, vol. 58, p. 735, 1986.

[104] M. Havenith, W. Bohle, J. Werner, and W. Urban, "Vibration rotation spectroscopy of excited electronic states Faraday-L.M.R. spectroscopy of CO $a^3\Pi$," *Mol. Phys.*, vol. 64, p. 1073, 1988.

[105] P. B. Davies and P. A. Martin, "Diode-laser spectroscopy of $a^3\Pi$ CO," *Mol. Phys.*, vol. 70, p. 89, 1990.

[106] R. Field, S. Tilford, R. Howard, and J. Simmons, "Fine structure and perturbation analysis of the $a^3\Pi$ state of CO," *J. Mol. Spectr.*, vol. 44, p. 347, 1972.

[107] C. Effantin, F. Michaud, F. Roux, J. D. Incan, and J. Verges, "High-resolution fourier spectrometry of the CO infrared emission spectrum: Perturbation analysis of the $a'^3\Sigma - a^3\Pi$ system," *J. Mol. Phys.*, vol. 92, p. 349, 1982.

[108] M. D. Morse, "Supersonic beam sources," in *Atomic, Molecular, and Optical Physics: Atoms and Molecules* (F. Dunning and R. G. Hulet, eds.), vol. 29, Part B of *Experimental Methods in the Physical Sciences*, p. 21, Academic Press, 1996.

[109] D. R. Miller, "Free jet sources," in *Atomic and Molecular Beam Methods* (G. Scoles, ed.), vol. 1, Oxford University Press, 1988.

[110] J. Marbach, F. X. Bronold, and H. Fehske, "Auger de-excitation of metastable molecules at metallic surfaces," *Phys. Rev. B*, vol. 84, p. 085443, 2011.

[111] M. Zubek and G. C. King, "A hot ribbon detector for metastable atoms," *J. Phys. E: Sci. Instrum.*, vol. 15, no. 5, p. 511, 1982.

[112] J. Tennyson, P. F. Bernath, A. Campargue, A. G. Császár, L. Daumont, R. R. Gamache, J. T. Hodges, D. Lisak, O. V. Naumenko, L. S. Rothman, H. T. N. F. Zobov, J. Buldyreva, C. D. Boone, M. D. D. Vizia, L. Gianfrani, J.-M. Hartmann, R. McPheat, D. Weidmann, J. Murray, N. H. Ngo, and O. L. Polyansky, "Recommended isolated-line profile for representing high-resolution spectroscopic transitions," *Pure and Applied Chemistry*, vol. 86, p. 1931, 2014.

[113] G. Insero, S. Borri, D. Calonico, P. C. Pastor, C. Clivati, D. D'Ambrosio, P. D. Natale, M. Inguscio, F. Levi, and G. Santambrogio, "Synchronizing mid infrared radiation with the primary frequency standard for molecular spectroscopy at sixteen digits of accuracy," *In preparation*, 2017.

[114] C. Clivati, G. Insero, S. Borri, D. Calonico, P. C. Pastor, D. D'Ambrosio, P. D. Natale, M. D. Pas, F. Levi, and G. Santambrogio, "Laser source at 5.8 μm traceable to a primary frequency standard using a 642 km optical link," *In preparation*, 2017.

[115] G. Insero, C. Clivati, D. D'Ambrosio, P. D. Natale, G. Santambrogio, P. G. Schunemann, J.-J. Zondy, and S. Borri, "Continuous-wave difference frequency generation in the mid-infrared with orientation-patterned gallium phosphide (OP-GaP) crystals," *Proc. SPIE*, vol. 10088-30, 2017.

[116] S. Borri, M. S. de Cumis, G. Insero, G. Santambrogio, A. Savchenkov, D. Eliyahu, V. Ilchenko, A. Matsko, L. Maleki, and P. D. Natale, "Whispering gallery mode stabilization of quantum cascade lasers for infrared sensing and spectroscopy," *Proc. SPIE*, vol. 10090-7, 2017.

[117] S. Marx, D. A. Smith, G. Insero, S. A. Meek, B. G. Sartakov, G. Meijer, and G. Santambrogio, "Measuring and manipulating the temperature of cold molecules trapped on a chip," *Phys. Rev. A*, vol. 92, p. 063408, 2015.

Publications List

- G. Insero, S. Borri, D. Calonico, P. C. Pastor, C. Clivati, D. D'Ambrosio, P. D. Natale, M. Inguscio, F. Levi, and G. Santambrogio, "Synchronizing mid infrared radiation with the primary frequency standard for molecular spectroscopy at sixteen digits of accuracy," *In preparation*, 2017

- C. Clivati, G. Insero, S. Borri, D. Calonico, P. C. Pastor, D. D'Ambrosio, P. D. Natale, M. D. Pas, F. Levi, and G. Santambrogio, "Laser source at 5.8 μm traceable to a primary frequency standard using a 642 km optical link," *In preparation*, 2017

- G. Insero, C. Clivati, D. D'Ambrosio, P. D. Natale, G. Santambrogio, P. G. Schunemann, J.-J. Zondy, and S. Borri, "Continuous-wave difference frequency generation in the mid-infrared with orientation-patterned gallium phosphide (OP-GaP) crystals," *Proc. SPIE*, vol. 10088-30, 2017

- S. Borri, M. S. de Cumis, G. Insero, G. Santambrogio, A. Savchenkov, D. Eliyahu, V. Ilchenko, A. Matsko, L. Maleki, and P. D. Natale, "Whispering gallery mode stabilization of quantum cascade lasers for infrared sensing and spectroscopy," *Proc. SPIE*, vol. 10090-7, 2017

- G. Insero, C. Clivati, D. D'Ambrosio, P. D. Natale, G. Santambrogio, P. G. Schunemann, J.-J. Zondy, and S. Borri, "Difference frequency generation in the mid-infrared with orientation-patterned gallium phosphide crystals," *Opt. Lett.*, vol. 41, no. 21, p. 5114, 2016

- S. Borri, M. S. de Cumis, G. Insero, S. Bartalini, P. C. Pastor, D. Mazzotti, I. Galli, G. Giusfredi, G. Santambrogio, A. Savchenkov, D. Eliyahu, V. Ilchenko, N. Akikusa, A. Matsko, L. Maleki, and P. D. Natale, "Tunable microcavity-stabilized quantum cascade laser for Mid-IR high-resolution spectroscopy and sensing," *Sensors*, vol. 16, no. 2, p. 238, 2016

- M. S. de Cumis, S. Borri, G. Insero, I. Galli, A. Savchenkov, D. Eliyahu, V. Ilchenko, N. Akikusa, A. Matsko, L. Maleki, and P. D. Natale, "Microcavity-

stabilized quantum cascade laser," *Laser Photonics Rev.*, vol. 10, no. 1, p. 153, 2016

- S. Marx, D. A. Smith, G. Insero, S. A. Meek, B. G. Sartakov, G. Meijer, and G. Santambrogio, "Measuring and manipulating the temperature of cold molecules trapped on a chip," *Phys. Rev. A*, vol. 92, p. 063408, 2015